DEVELOPMENT OF WIND TURBINE TOWERS USING FIBER REINFORCED POLYMERS

BY

Nibong Ungkurapinan

A Thesis

Submitted to the Faculty of Graduate Studies

In Partial Fulfillment of the Requirement for the Degree of

DOCTOR OF PHILOSOPHY

Department of Civil Engineering

University of Manitoba

Winnipeg, Manitoba

THE UNIVERSITY OF MANITOBA

FACULTY OF GRADUATE STUDIES

*****

COPYRIGHT PERMISSION

DEVELOPMENT OF WIND TURBINE TOWERS USING FIBER REINFORCED POLYMERS

BY

Nibong Ungkurapinan

A Thesis/Practicum submitted to the Faculty of Graduate Studies of The University of Manitoba in partial fulfillment of the requirement of the degree

Of

Doctor of Philosophy

DEDICATION

This thesis is dedicated to my parents, Mr. Nepon and Dr. Nongnuj (M.D.) Ungkurapinan. Without their encouragement, supports, and generosity of spirit, I would never have come this far.

ABSTRACT

With an ongoing trend in the wind turbine market, the size of wind turbines has been increasing continuously. Larger wind turbines imply an increase in size, weight, and loads acting on the wind turbine tower. This requires towers to be stronger and stiffer, and consequently leads to bigger tower diameters. Because of their size and weight, transportation and erection require heavy equipment that makes the use of such towers prohibitive in remote communities. To tackle this problem, a research program was initiated at the University of Manitoba to develop the technology required for the fabrication of wind turbine towers constructed of fiber reinforced polymers (FRP) for use in remote communities in Canada.

The research program was carried out in stages. During the first stage, a feasibility study and an analytical investigation on various shapes of FRP towers were conducted. The concept of a multi-cellular composite tower was examined in great detail and the finite element results showed that such a tower could result in almost 45 percent reduction in weight.

In the second stage of this research program, a robotic filament winding machine was designed and constructed in the Composites Laboratory of the University of Manitoba. It was used to fabricate the multi-cell tower specimens for testing.

The third stage of the research program involved the experimental investigation, which was carried out in three phases. In the first phase, two single cell specimens were tested to failure under lateral loading. The specimens were 8 ft (2.44 m) long. The second phase involved the testing of two single cells loaded in compression. The third phase of the experimental investigation involved the testing of two eight-cell jointed tower specimens. The specimens were octagonal and tapered, with a diameter of 21.4 in (543 mm) at the base and 17.4 in (441 mm) at the top. They were 16 ft (4.88 m) in height and tested as cantilever under static loading. Local buckling was the dominant failure mode of the specimens tested. One of these towers was subsequently repaired and retested to determine whether repairing would restore the original strength of the tower.

The last stage of the research program, various finite element models were developed to analyze the structural behavior of tested specimens. The results from finite element models were validated through comparison with experimental results. The finite element models gave a very good prediction of the structural performance of the FRP towers tested.

TABLE OF CONTENTS

CHAPTER 6

NUMERICAL ANALYSIS

CHAPTER 7

DESIGN OF WIND TURBINE TOWERS

LIST OF TABLES

LIST OF FIGURES

CHAPTER 1

INTRODUCTION

1.1 GENERAL

Wind is a clean, renewable resource with enormous environmental benefits. Wind is already a major source of energy across Europe. In 2003 alone, 8344 MW of wind power were installed. This installation brought the cumulative worldwide installed wind energy beyond 40,000 MW. In fact, wind power accounted for nearly 0.5 percent of the world's electricity supply by the end of 2003 (Jones, 2004). Even though Canada has one of the world's best wind resources, it is behind other countries in utilizing wind power. Only 81 MW of wind power were installed across Canada in 2003. Hence, there is a significant potential for growth in wind energy in Canada.

In recent years both the size of wind turbines and tower heights have been steadily increasing. The new turbines in the market are in the range of more than 2 MW with the hub height above 90 m. Larger wind turbines imply an increase in size, weight, and loads acting on the wind turbine towers. Therefore, this

requires towers to be stronger and stiffer, and consequently leads to bigger tower dimensions. As tubular steel towers become more massive, costs associated with transportation and erection have increased. In addition, a special crane for erecting tower sections, nacelle, and blades is required.

There are efforts to reduce the cost of wind turbines. Most of the cost reductions have concentrated mainly on blades and power production systems in the nacelle. However, no effort has been make to reduce the cost of the towers. This is an interesting situation as the tower is now one of the most expensive components comprising around 20 to 30 percent of total wind turbine system costs (Danish Wind Turbine Manufactures Association (DWTMA), 2005; and WindTower Composites, 2003).

The most common type of wind turbine towers today is the tubular steel tower. These are usually manufactured in two to three sections of 20 m to 30 m with flanges at either end and bolted together on site. Because of their size and weight, transportation and erection require heavy equipment that make the use of such towers prohibitive in remote areas. To develop towers that are easy to transport and construct in remote areas becomes an important strategy.

In recent years, fiber reinforced polymers (FRP) have received much attention as alternative materials to steel in the construction industry. The FRP materials have the potential to decrease the weight of the wind turbine towers, leading to

substantial savings in transportation and construction as well as allowing the erection of such towers in remote communities.

An extensive research has been carried out at the University of Manitoba to develop lightweight multi-cell composite wind turbine towers. This new concept tower provides the same benefit as of the tubular steel tower. It also overcomes the transportation restriction, because of its segmental construction. In addition, for offshore applications, where tubular steel towers face the risk of corrosion, composite towers are corrosion resistant and, therefore, have lower maintenance costs.

1.2 OBJECTIVES

The primary objective of this research project was to develop the technology required for the fabrication of wind turbine towers constructed of fiber reinforced polymers (FRP) for use in remote communities. More specifically, the objectives of this research program were:

a) To conduct a review of the load requirements for towers taking into account weights of nacelle, rotors, etc;

b) To conduct a finite element analysis and design of various types of towers, such as single-cell, multiple-cell towers using internationally recognized design standards;

c) To carry out an experimental program to determine the material properties of various FRP layouts, to examine the effect of the type of resin, type of fiber, and fiber angle;

d) To fabricate and test scaled prototype wind turbine towers under lateral loading; and

e) To develop a numerical model to be used in analyzing the structural behavior of composite wind turbine towers.

The research program was carried out in stages. During the first stage, a feasibility study and an analytical investigation on various shapes of FRP towers were carried out using the ANSYS finite element program. The concept of a multi-cell composite tower, as shown in **Figure 1-1**, was examined in great detail and the finite element results showed that such a tower could result in almost 45 percent reduction in weight.

In the second stage of this research program, a robotic filament winding machine was designed and constructed in the Composites Laboratory of the University of Manitoba. It was used to fabricate the prototype multi-cell composite tower specimens for testing. The winder has two independent motions: one is to rotate the mandrel and the other is to control the linear movement of fibers. Users can program the winder to control fiber orientation by changing the movement speed of those axes. The details related to the design and the fabrication of the winder, are given in subsequent sections.

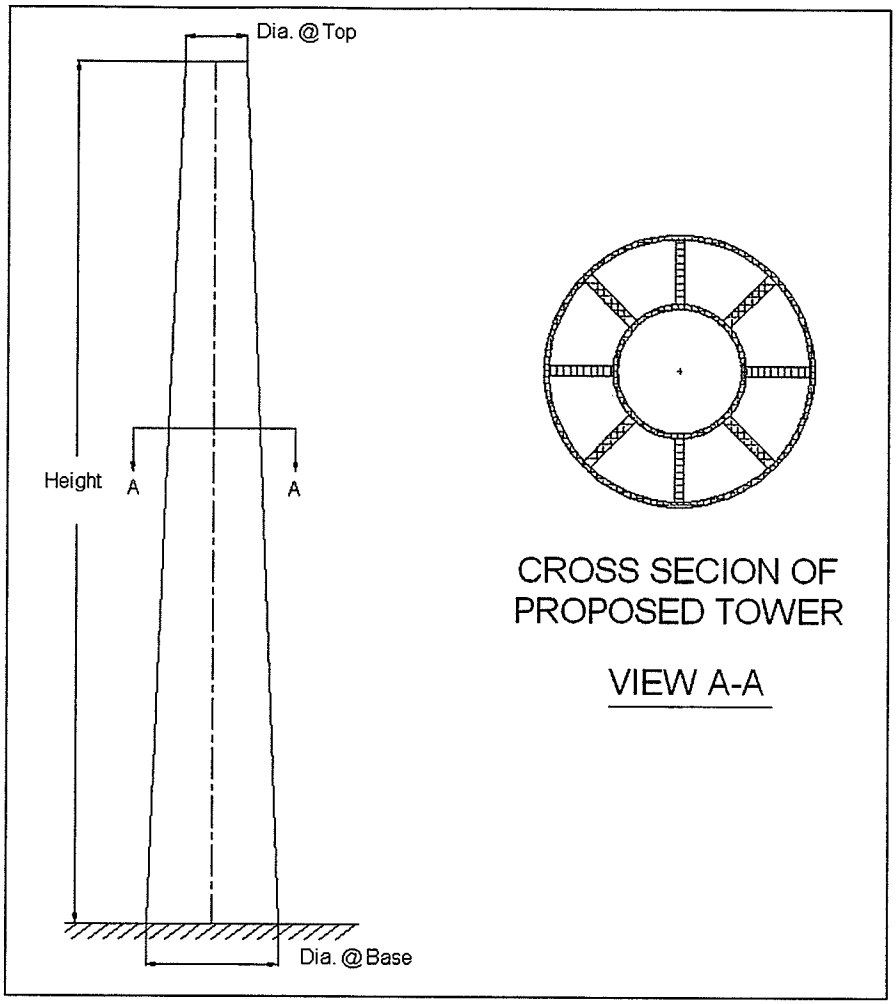

Figure 1-1 Proposed FRP tower

The third stage of the research program involved the experimental investigation, which was carried out in three phases. In the first phase, two single cell specimens were tested to failure under lateral loading. These specimens were 8 ft (2.44 m) long. The second phase involved the testing to failure of two single cell specimens in compression. The two specimens had a height of 1280 mm and 1780 mm, respectively. The third phase of the experimental investigation involved the testing of two 8-cell jointed scaled towers. These specimens were tested as cantilevers under static loading. The jointed scaled towers had a total

height of 16 ft (4.88 m). The testing was conducted at the W.R. McQuade Structural Engineering Laboratory of the University of Manitoba.

In the last stage of the research program, finite element models were developed to analyze the structural behavior of single and multi-cell composite cells and towers. The results from finite element models were validated through comparison with the experimental results.

1.3 SCOPE

This thesis consists of eight chapters. The introduction to the project and the objectives and scope of this study are given in Chapter 1.

The survey of the related literature is presented in Chapter 2. This survey reviews the history of wind turbine, types of wind turbine, the current design standards and specifications for wind turbine generator systems.

Details of the design and manufacturing of the robotic filament winding machine required for the fabrication of the specimens used in this research project are described in Chapter 3. The detail descriptions of each component used in the winder are also given. An example of the input command used to control the winding pattern is also presented here.

A description of the test specimens, the fabrication of the test specimens, and the testing procedures are presented in Chapter 4. This chapter concludes with a description of the material characterization tests performed.

The results of the experimental program are given in Chapter 5. A detailed of structural performance and observed failure modes of the tested specimens are also discussed in this chapter.

The development of the finite element models used to analyze single and multi-cell composite segments and towers is described in Chapter 6. Emphasis is placed on comparing the theoretical results obtained from these finite element models with the experimental results.

The design of a 750 kW 50 m wind turbine tower is presented in Chapter 7. The description of the load requirements for the wind turbine tower is given here. A comparison between the structural performance of a multiple-cell composite tower and an equivalent steel tower is given in this chapter.

A summary of the research finding is given in Chapter 8 along with a number of conclusions and recommendations for future research.

1.4 ACKNOWLEDGEMENTS

The author wishes to acknowledge the contribution of the following individuals and groups without whom this project would not have been a success.

- Dr. D. Polyzois, his advisor, for his guidance, advice, and encouragement, as well as the opportunity to work on an exciting and challenging research topic;
- Members of his committee, Dr. A. Mufti, Dr. G. Wang, and Dr. J.J. Roger Cheng for their comment and useful suggestions;
- Dr. N. Xu, research associate, for his dedicated help and patience over the course of this project;
- Mr. V. Burachynsky, Ph.D. candidate, for his helpful suggestions and assistant during the design and manufacturing of the equipment and tools used in this project;
- Mr. A. Ochonski, Ph.D. candidate and Mr. D. Philopulos, E.I.T., for their tireless help during fabrication and testing of the specimens;
- Mr. I. Polyzois, undergraduate research assistant, for his assistant during manufacturing of the specimens;
- Mr. M. Mcvey, Mr. G. Whiteside, Ms. E. Rivera and fellow graduate students for their support, cooperation and assistance over course of this investigation;

- ISIS Canada, NSERC, and Faculty of Gradate Studies for their financial contribution to the project;
- The Thai community in Winnipeg for providing a homely atmosphere during his study; and
- Kyung-Min Park, for her tremendous support, encouragement, and understanding.

CHAPTER 2

LITERATURE REVIEW

2.1 BRIEF HISTORY OF WIND ENERGY

The wind has played a long and important role in the history of human civilization. The first known use of wind dates back 5,000 years to Egypt, where boats used sails to travel from shore to shore (EERE, 2005). The first true windmill, a machine with vanes attached to an axis to produce circular motion, may have been built as early as 2000 B.C. in ancient Babylon. By the 10th century A.D., windmills with wind-catching surfaces as long as 16 feet and as high as 30 feet were grinding grain in the area now known as eastern Iran and Afghanistan.

The western world discovered the windmill much later. The earliest written references to working wind machines dated from the 12th century. These too were used for milling grain. It was not until a few hundred years later that windmills were modified to pump water and reclaim much of Holland from the sea. In the 19th Century, when settlers moved into the western United States,

they built windmills to pump water so that they could farm and raise livestock.

During the 1980s, sparked by increased concerns for the environment and diminishing fossil fuel supplies, windmills designed for the generation of electricity (referred to as wind turbines) were first installed in large numbers in California, and later in Denmark. This was the start of the modern wind turbines. Since those early days, wind turbine technology has advanced enormously.

The new megawatt-class wind turbines are producing high quality utility-grade power that can compete directly with conventional forms of power production. The megawatt-class wind turbine of today, which supplies enough power for 300 to 600 houses, produces as much as 30 times the power of the wind turbines of the 1980's. This means that many fewer turbines are needed today than 20 years ago for the same power output. The megawatt-class wind turbine has also evolved aesthetically. The turbine comprises a light colored tubular tower, which integrates with the landscape in a more natural way, and three large rotor blades that spin slowly and quietly.

2.2 TYPES OF WIND TURBINE TOWER

Wind turbine towers are used to support the nacelle and the rotors. Towers need to be strong to resist the load transferred from the wind turbine. Three types of

tower constructions that are commonly used for supporting a large wind turbine are:

- Tubular towers (steel or concrete);
- Lattice towers; and
- Guyed towers.

Tubular steel towers, as shown in **Figure 2-1 (a)**, are the most commonly used for supporting large wind turbines. They are usually manufactured in sections of 20 m to 30 m with flanges at either end, and bolted together on the site. The towers are conical shape, with their diameter increasing towards the base, in order to increase their strength and to save materials at the same time. They are clearly preferred over other types of towers because of aesthetic reasons. In addition, in sub-zero weather, the tubular towers can provide the protection from wind during maintenance work.

Lattice towers, as illustrated in **Figure 2-1 (b)**, are manufactured using welded steel profiles. The basic advantage of lattice towers is cost, since a lattice tower requires only half as much material as a freely standing tubular tower with a similar stiffness. The basic disadvantage of lattice towers is their visual appearance. It is also difficult to do any service works on lattice towers in cold climates. Be that as it may, for aesthetic reasons lattice towers have almost disappeared from use for large, modern wind turbines.

Many small wind turbines are built with narrow pole towers supported by guy wires, as shown in **Figure 2-1 (c)**. However, there were some guyed towers that have been used for large wind turbines in the 1980's. The advantage is weight savings, and thus cost. The disadvantage is the difficulty to access around the towers, which makes them less suitable in farm areas. Finally, this type of tower is more prone to vandalism, thus compromising its overall safety.

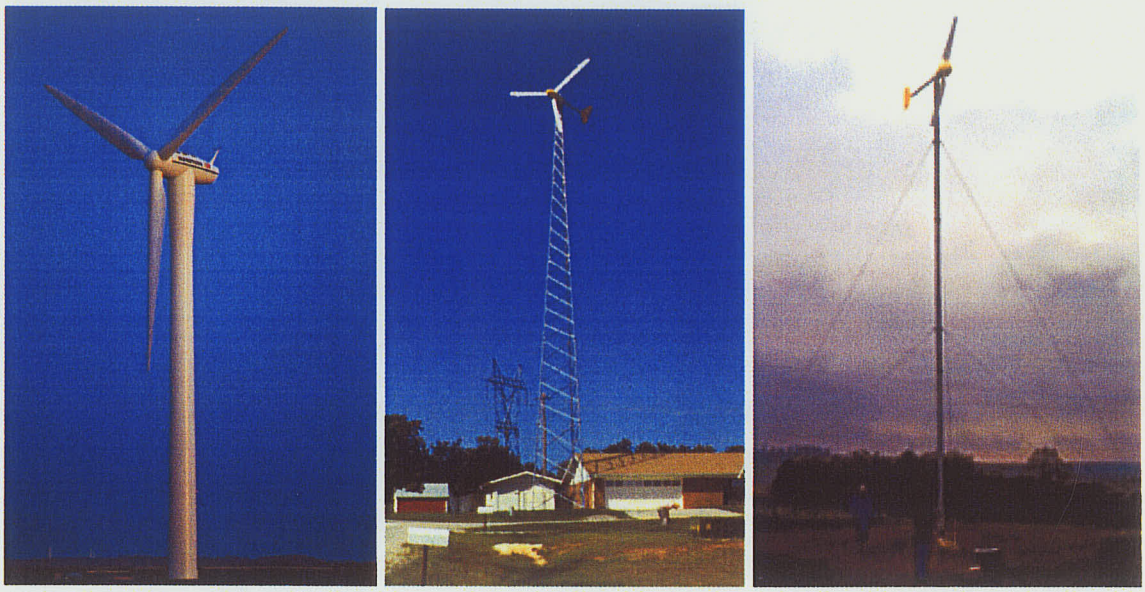

(a) **(b)** **(c)**

Figure 2-1 Types of wind turbine tower (DWTMA, 2005)

2.3 INFRASTRUCTURE CHALLENGES

Although considerable technology input has gone into the design and manufacturing of the blades, the technology for towers has been at a virtual

standstill. But, there have been some few researches that have focused on improving the design of towers. Bormann and Reuter (1996) had proposed alternative structural concepts to increase the stiffness of towers. They have considered an alternative tower design using segments with stringers. However, no reports on their structural performance of such towers have been published.

Brughuis (2003) developed the alternative hybrid wind turbine tower. The hybrid tower uses prefabricated concrete element to replace the conventional steel tower section. The research showed that this new hybrid concept could overcome the restriction of transportation of the tower. The weight of the tower and the erection cost however have not been solved.

Because of their lightweight, high strength-to-weight ratio, and corrosion resistant, the use of fiber composite materials has been increasing as the construction material in the past two decades. WindTower Composites (2003) has developed a commercially available composite space frame tower, which yields cost saving in three areas: a) reduced manufacturing cost of the tower; b) reduction or elimination of the crane used; and, c) substantial savings in transportation cost. Even though the space frame constructed has certain benefit, it still faces maintenance difficulty in sub-zero weather, and for aesthetic reason it has not been very popular (Gipe, 1995). Hence, there is a need to develop an innovative alternative wind turbine tower.

2.4 WIND TURBINE TOWERS DESIGN STANDARDS

There is no North America design specification or standard for wind turbine towers. Therefore, the Germanischer Lloyd: Rules and Regulations, Part 1 – Wind Energy (1993) and the IEC 61400-1 International Standard (1999) were used in this research study. Both standards are essentially the same. These two standards cover material, manufacturing, and loads requirements for towers, taking into account the climate conditions. Serviceability limits for design are also described. For instance, the deformation limit state is defined by maintenance of a safety gap, the distance between rotor blade and tower or rotor blade and guyed wire. The standards require the use of a structural dynamics model to predict design loads. This model uses to determine the loads over a range of wind speed, using the turbulence conditions and other extreme wind conditions. All relevant combinations of external load conditions must be taken in account. A minimum set of such combinations defined as load cases is described in the standards.

In the present research project, simplified design loads described in the Germanischer Lloyd: Rules and Regulations, Part 1 – Wind Energy (1993) were used. More details of the loads required in the design of a wind turbine tower are given in Chapter 7.

2.5 STRUCTURAL BEHAVIOR OF TUBULAR STRUCTURES

Tubular structures, which have found a wide application in tower construction, consist of cylindrical or conical shells. For the practical analysis and design of tubular structures, the theory of thin-walled shells can be used with certain limitations. This is because the formulae were developed under the assumption that the thickness-to-radius ratio (t/R) is very small. However, in tubular tower structures, the t/R ratio may be large and the results will have an approximate character. Thus, it is important to find the maximum t/R ratio when the deviation obtained by the thin-walled shell theory is practically permissible. In other word, it is important to find the limiting value of the t/R ratio at which the tubular structures may be considered as a thin-walled.

Troitsky (1986) suggested that in the design of tubular structures, thin-walled shells can be applied at least for the values of $t = 0.1R$, where R is the minimum radius of curvature of the middle surface. Furthermore, for an approximate design, this limits may be increased even to a value of $t = 0.2R$.

Buckling may be defined as a localized failure in the form of wrinkle or indentation caused by overstress or instability of the wall of tubular structures on the compression side. Such a local buckling is the result of localized structural instability of the wall of the structure when subjected to a compressive stress. This type of buckling could occur when the compressive stresses exceed critical

values. Collapse, on the other hand, is defined as a general failure usually in the form of flattering of the shell cross section over a considerable length as the result of the action of external pressure in the shell.

Both resistance to collapse and resistance to local buckling are functions of the diameter-to-thickness ratio (D/t) of the shell. The lower this ratio is, the greater the resistance of failure in both cases.

2.6 OVERALL AND LOCAL BUCKLING OF CYLINDRICAL SHELLS

In the design of tubular steel structures, after determining the wall shell thickness in order to satisfy tensile stress requirements, the stability of the wall shell should be checked for local buckling.

A thin-walled cylindrical shell subjected to compression in the direction of its longitudinal axis may fail either by the instability of the shell as a whole, involving bending of the axis, or by local instability of the wall of the shell, which may not at all involve lateral distortion of the axis. The former type of failure is when the strength depends on the length-to-radius ratio of the shell (L/R). The latter type of failure is known by various names such as secondary flexure, wrinkling, or local buckling. The latter type of failure is often governing in the design of thin-walled cylinders.

The stability against local buckling depends on the thickness-to-radius ratio of the shell (t/R). Wrinkling is local in nature and depends on the combined compressive stresses at the point. This type of failure is due to the deformation of characteristic wrinkles or bulges, circular or lobed in shape.

In thin-walled tubular structures, there are mainly two important considerations. Firstly, local buckling should be prevented at stresses below yield strength. Secondly, a more severe restriction is that tendency to buckle locally should not reduce the general buckling load of a whole structure (Chilver, 1967; Troitsky, 1986; and Allen et al., 1990).

The critical buckling stress of cylindrical shell under axial compression (Chilver, 1967; Baker et al., 1972; Troitsky, 1986; Allen et al., 1990; DIN18800, 1990; and Beedle, 1991) can be expressed as:

$$\sigma_{cr} = \frac{Et}{R\sqrt{3(1-\mu^2)}} = 0.605E\frac{t}{R} \qquad \textbf{Equation 2.1}$$

where

R = the radius of the shell

t = the thickness of the shell

E = modulus of elasticity of material (200,000 MPa for steel)

μ = Poisson's ratio (0.3 for steel).

In most of codes the critical buckling stress of cylindrical shells under axial compression is multiplied by the factor C (Baker et al., 1972; Troitsky, 1986; DIN18800, 1990; and Beedle, 1991). This factor C either takes into account the asymptotic transition of the ideal axial buckling stress curve because of imperfections or is based on an experiment data. Therefore, each code has a different value of factor C. Many codes address this problem and give rules for the design of simple shells under uniform loading conditions. However, the problem of how to interpret buckling stresses or load predictions can be simplified through the use of finite element analyses.

It should be noted that the most important parameter affecting the buckling strength of thin-walled shells is the amplitude of imperfection. It is important that the structural engineer or the fabricator is aware of the physical dimensions of the imperfections on which the design has to be based.

For a lobed form of buckling, the critical buckling stress of a cylindrical shell under axial compression can be expressed as (Southwell, 1913; Prescott, 1924; and Dean, 1925):

$$\sigma_{cr} = \frac{E}{\sqrt{3(1-\mu^2)}}\left(\frac{t}{R}\right)\frac{n^2-1}{n^2+1} \qquad \textbf{\textit{Equation 2.2}}$$

in which

n = the number of lobes in the wrinkle.

In these derivations, it is assumed that the elastic limit of the material is not exceeded. In general, although different approaches are used, the same results are obtained for a uniform circular bulge or wrinkle. In any case, when the number of lobes is greater than 3, ***Equation 2.2*** gives substantially the same critical stress as ***Equation 2.1***.

It may be noted that ***Equation 2.1*** for local buckling does not involved the length of the shell. That is the critical buckling stress is independent of the length of the shell. However, in the case of long slender shells, the total load carrying capacity is affected by the ratio of the length-to-radius. If there is a tendency to buckle, the stress will no longer be uniform over a section, and failure will occur when the maximum stress on the section becomes equal to the critical buckling stress. When the local loss of stability passes to the overall stability, the ratio of the length-to-radius lies within the following limits:

$$1.72\sqrt{t/R} \le L/R \le 2.38\sqrt{R/t} \qquad \textbf{Equation 2.3}$$

For a long slender cylindrical shell, wrinkle failure does not occur, rather, lateral buckling taken place. The elastic critical stress defined as the Euler buckling stress, is given by the following formula:

$$\sigma_{cr} = k\frac{\pi^2 E}{(L/r)^2} \qquad \textbf{Equation 2.4}$$

where

r = radius of gyration of the cross section of the cylinder

L = total length of the shell

k = a constant depending on the end conditions

For a very thin shell $r^2 = R^2/2$, and ***Equation 2.4*** becomes:

$$\sigma_{cr} = k\frac{\pi^2}{2}E\left(\frac{R}{L}\right)^2 \qquad \textbf{Equation 2.5}$$

Experimental results were used to verify ***Equation 2.1*** (Troitsky, 1986; and Beedle, 1991). However, serious disagreement exists between the results from classical theory and the experimental stress for the buckling capacity of cylindrical thin shells under axial compression. This can be attributed to the imperfections in the shells, as previous stated.

Baker et al. (1972) suggested the following formula for the determination of the local buckling stress of cylindrical shells of moderate length:

$$\sigma_{cr} = 0.605\gamma E\left(\frac{t}{R}\right) \qquad \textbf{Equation 2.6}$$

where, the values of the correlation factor γ, same as factor C used in DIN18800 (1990), in the function of the R/t ratio. The correlation γ is used to account for the difference between theoretical and experimental results.

For a large D/t ratio, the magnitude of the critical buckling stress recommended in the elastic range (Wilson and Newmark, 1933) is given as follows:

$$\sigma_{cr} = \frac{8{,}000}{D/t} \qquad \textbf{Equation 2.7}$$

Assuming a factor of safety equal to 1.5, the allowable local critical buckling stress is:

$$\sigma_{cr} = \frac{5{,}333}{D/t} \qquad \textit{Equation 2.8}$$

Long cylindrical shells must be checked for overall buckling given by the Euler stress in ***Equation 2.5***.

2.7 EXPERIMENTAL INVESTIGATION OF TUBULAR FRP STRUCTURES

During the past decade, there were several researchers investigated the behavior of tubular FRP structures. McClure et al. (1992) conducted an investigation on FRP poles. The tested specimens were tapered with a hollow cross section. The experimental results indicated that FRP poles could safely resist loads comparable to those of wooden poles under the same conditions. The behavior of the FRP poles was found to be elastic even for large defections.

Lin (1995) investigated the behavior of FRP tubes under cantilever loading condition. Most of his work was theoretical. Four scaled specimens were tested up to failure. The specimens had a circular hollow cross section with the shell thickness of 6-mm. The experimental results showed a linear relationship between load and tip deflection.

Ibrahim (2000) studied the performance of glass fiber reinforced plastic poles for transmission lines. A total of twelve 2.5 m and twelve 6 m GFRP poles were tested under lateral loading. The experimental results showed that GFRP poles

can sustain a load capacity similar to that of the wooden, steel, or concrete poles. Failure due to local buckling was the most dominant failure mode of the specimens tested. He also developed a finite element model using the ANSYS software program to predict the behavior of FRP poles. The numerical results compared well with the experimental results. In addition, he also investigated the effect of different fiber orientation on FRP poles.

Philopulos (2002) investigated the structural performance of filament wound GFRP jointed poles. The objective in his investigation was to determine the minimum joint lengths required to develop the full capacity of jointed poles. Four GFRP jointed poles were tested under bending. Most of the specimens failed by local buckling near the base. The experimental results showed a very short joint length may lead to joint failure. A minimum joint length of 1/10 of the length of a segment being jointed was recommended. The ANSYS finite element program was used to model the GFRP jointed poles. The finite element model predicted well the ultimate load for all poles tested as well as their deflection characteristics.

CHAPTER 3

DEVELOPMENT OF ROBOTIC FILAMENT WINDING MACHINE

3.1 GENERAL

A number of advanced processes are available for producing high performance fiber reinforced polymers structures. These processes are generally automated such as pultrusion, braiding, and filament winding. Filament winding is an attractive process for a number of reasons such as low production cost, design flexibility, control fiber orientation, and high fiber volume.

Filament winding is the process of placing or winding continuous fibers on a mandrel surface in a precise geometric pattern. By winding continuous strands of glass fiber, or other material, in very precise patterns, structures can be built with superior structural properties and low weight.

Filament winding is a highly automated process, where structural components are fabricated by rotating a mandrel while a delivery-head precisely positions fibers on the mandrel surface.

The ability to provide high strength-to-weight ratios makes filament winding one of the most effective manufacturing processes. Directional strength and stiffness through the wound part can be optimized by aligning the fibers in the direction of the loads. This makes fiber orientation critical to the performance of the part.

During the winding process the fibers are either run through a low viscosity resin, or the resin matrix is pre-impregnated into the fiber. Then the resin impregnated bands of fibers under controlled tension are fed through a payout eye and placed on a rotation mandrel in a prescribed geometric pattern. After the composite layers are wound, the component is cured and removed from the mandrel.

Typically, a filament winding machine consists of a mandrel, a carriage system, and a motion control system, as shown in **Figure 3-1.** The motion control system should be able to precisely control mandrel and carriage movements as well as to allow users to program the winding pattern.

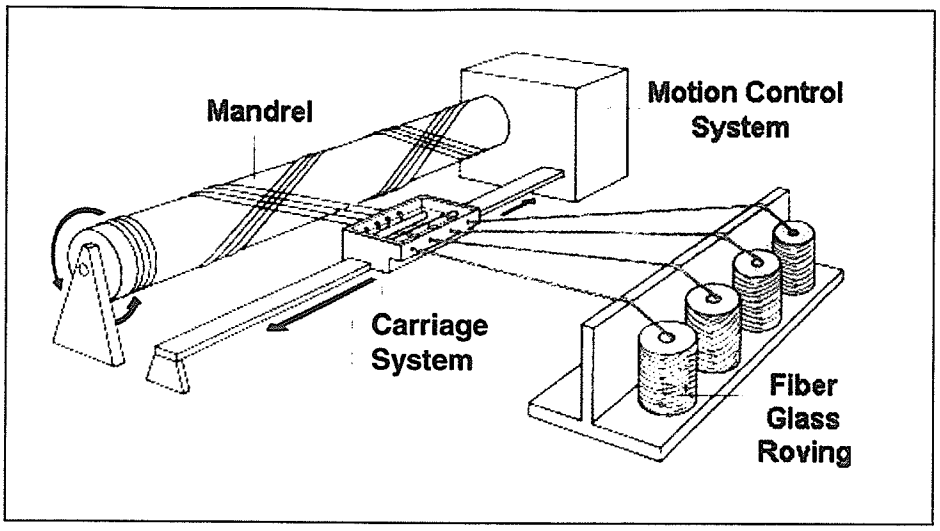

Figure 3-1 Typical filament winding machine (Agarwala and Broutman, 1990)

In this chapter, the design and fabrication of a custom made Robotic Filament Winding Machine (RFWM) is presented. The details of a motion control system used, the design and fabrication of the winder, and the winding program are described.

3.2 MOTION CONTROL SYSTEM

The DMC-1425 motion controller from Galil Motion Control was selected and used for the filament winding machine. The DMC-1425 is configured for two-axis applications. The controller accepts feedback from a quadrature linear or rotation encoder with input frequencies up to 12 million quadrature counts per second. Several motion parameters can be specified including speed,

acceleration, and deceleration rates. The DMC-1425 circuitry can be divided into the functional groups shown in **Figure 3-2**.

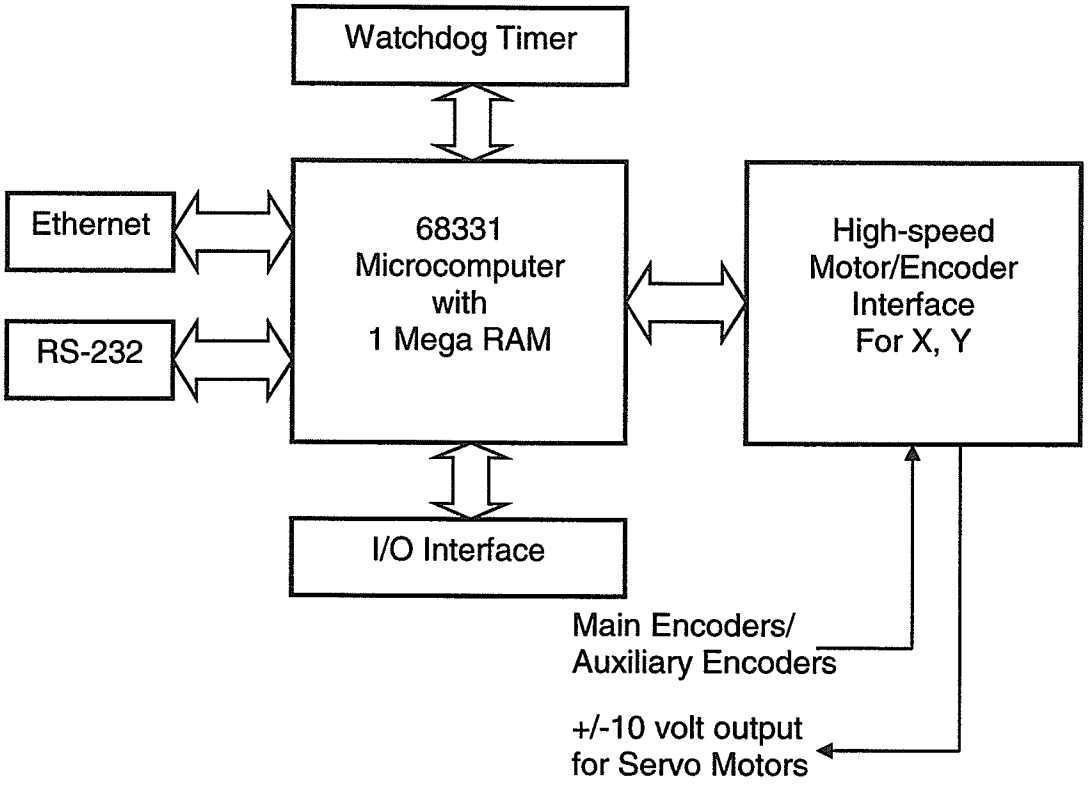

Figure 3-2 DMC-1425 functional elements

As shown in **Figure 3-3**, the DMC-1425 is part of a motion control system, which includes amplifiers, servo motors, and encoders. These elements are described below.

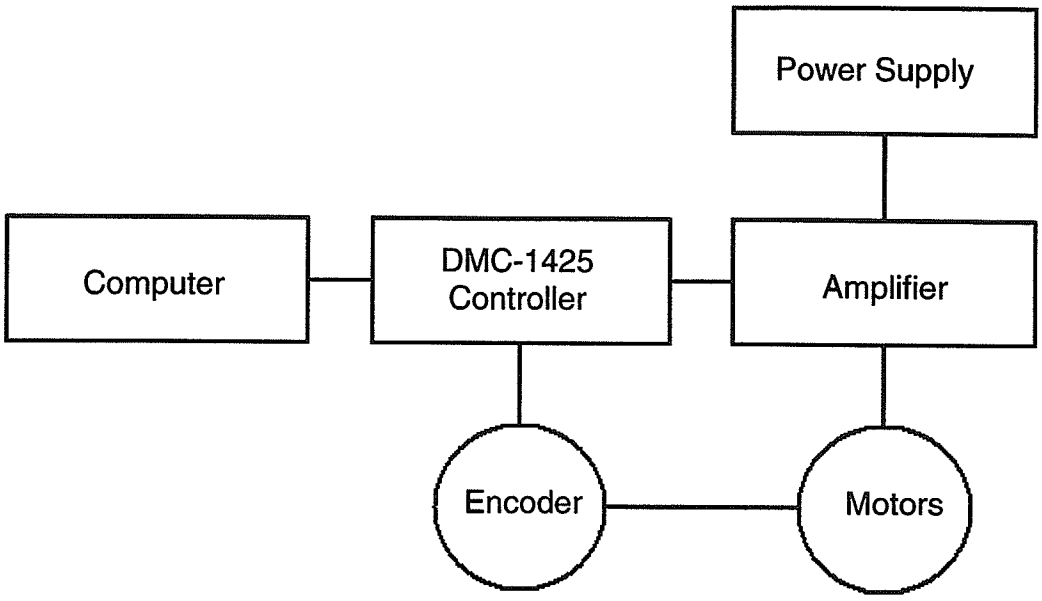

Figure 3-3 System elements

3.2.1 Servo Motors

A motor converts current into torque, which produces motion. Each axis of motion requires a motor sized properly to move the load at required speed and acceleration. Two NEMA 34 servo motors with encoders were used. The encoder connectors for the NEMA 34 are shown in **Table 3-1**. It is very crucial to connect the right encoders to the right interconnect module. This allows the user to be able to control the movement position of the servo motor.

Table 3-1 NEMA 34 encoder connectors

Function	Wire Color
+VCC	RED
GND	BLACK
CHA-	YELLOW
CHA+	WHITE
CHB-	BLUE
CHB+	GREEN
INDEX-	BROWN
INDEX+	ORANGE

The motor has a maximum rotational speed of 4600 rpm, which is much higher than the speed required during the winding process. Therefore, a reduction gear ratio of 100:1 was added to the system. The reduction gear helps to increase the torque and run the motor at more efficient speed. The dimension details and specifications of the NEMA 34 servo motor are given in **APPENDIX A.**

3.2.2 Power Supply and Amplifier

The CPS-15-80 power supply manufactured by Galil Motion Control was used. The power supply was rated at 80 VDC and constant current of 12 A. The CPS-15-80 is an unregulated DC power supply that compliments the amplifiers.

For each axis, the power amplifier converts a ±10 volt signal from the controller into current to drive the motor. An MSA-12-80 amplifier manufactured by Galil Motion Control was used for each motor. The amplifier provides DC voltage from 20 to 80 volts and continuous current of 12 amperes. **Figure 3-4** shows the connection diagram, which illustrates the connection between a DMC-1425 controller, a shared power supply, two amplifiers, and two servo motors.

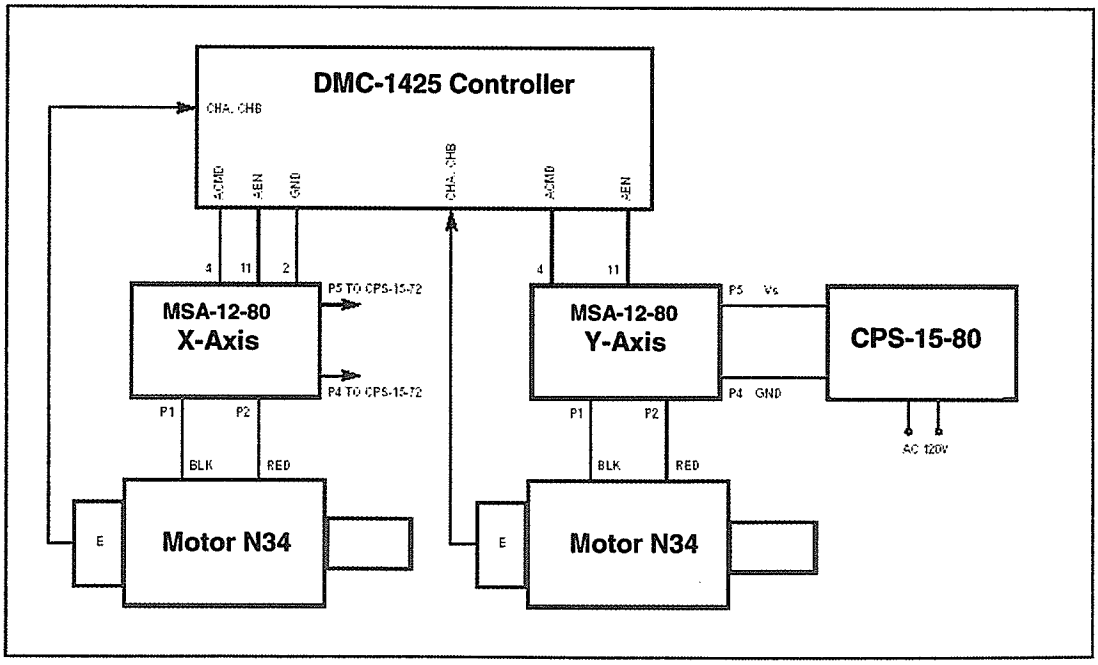

Figure 3-4 Connection diagram (DMC-1425 user manual, 2002)

3.2.3 Encoder

An encoder translates motion into electrical pulses, which are fed back into the controller. Typical encoders provide two channels in quadrature, known as CHA and CHB. Quadrature encoders used in this system are differential channels (CHA+, CHA-, CHB+, CHB-) and have a third channel (INDEX) for synchronization.

The ICM-1460 Interconnect Module was used. It provides screws terminals for 37 pin D-type cable from the DMC-1425 controller into screw-type terminals to connect system elements. The terminal specifications of ICM-1460 are given in **APPENDIX B**.

3.3 DESIGN AND FABRICATION OF THE ROBOTIC FILAMENT WINDING MACHINE

The two axes robotic filament winding machine is shown in **Figure 3-5**. The basic design requirements of this winder are: a) to be able to control the rotation of the mandrel, and b) to be able to control the movement of the carriage. The winder consists of two supported frames, carriage, chain box, chain transmission, and mandrel transmission.

Frames were fabricated to support both the mandrel and the chain box at each end. HSS 38x38x25 steel sections were cut into designed length and welded together to fabricate the frames. Then bolt holes were drilled in order to support the mandrel transmission system, which consists of: two chucks, which are used to grab the mandrel, two shafts for each end, two pillow blocks, a timing pulley, and a timing belt, as shown in **Figure 3-6**.

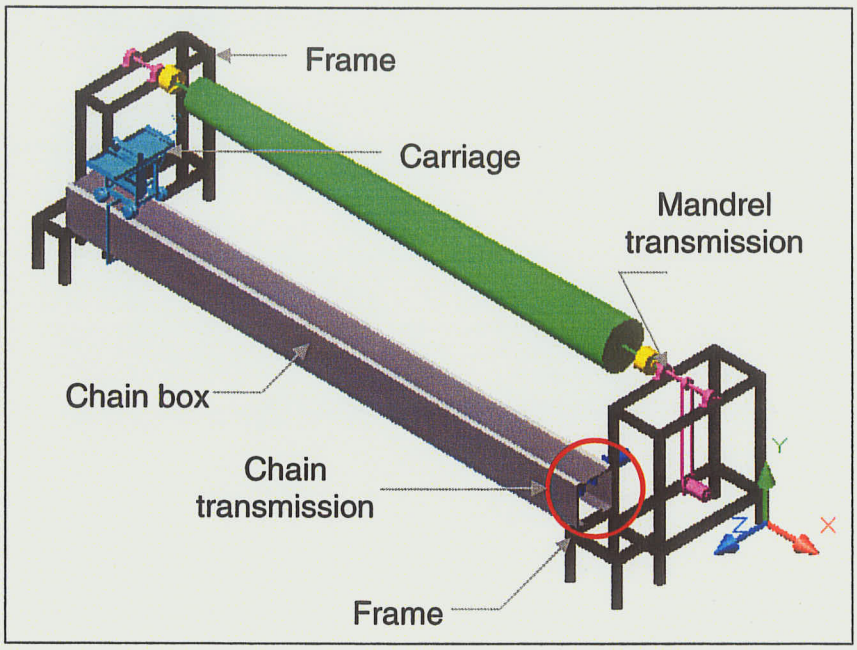

Figure 3-5 Schematic of robotic filament winding machine

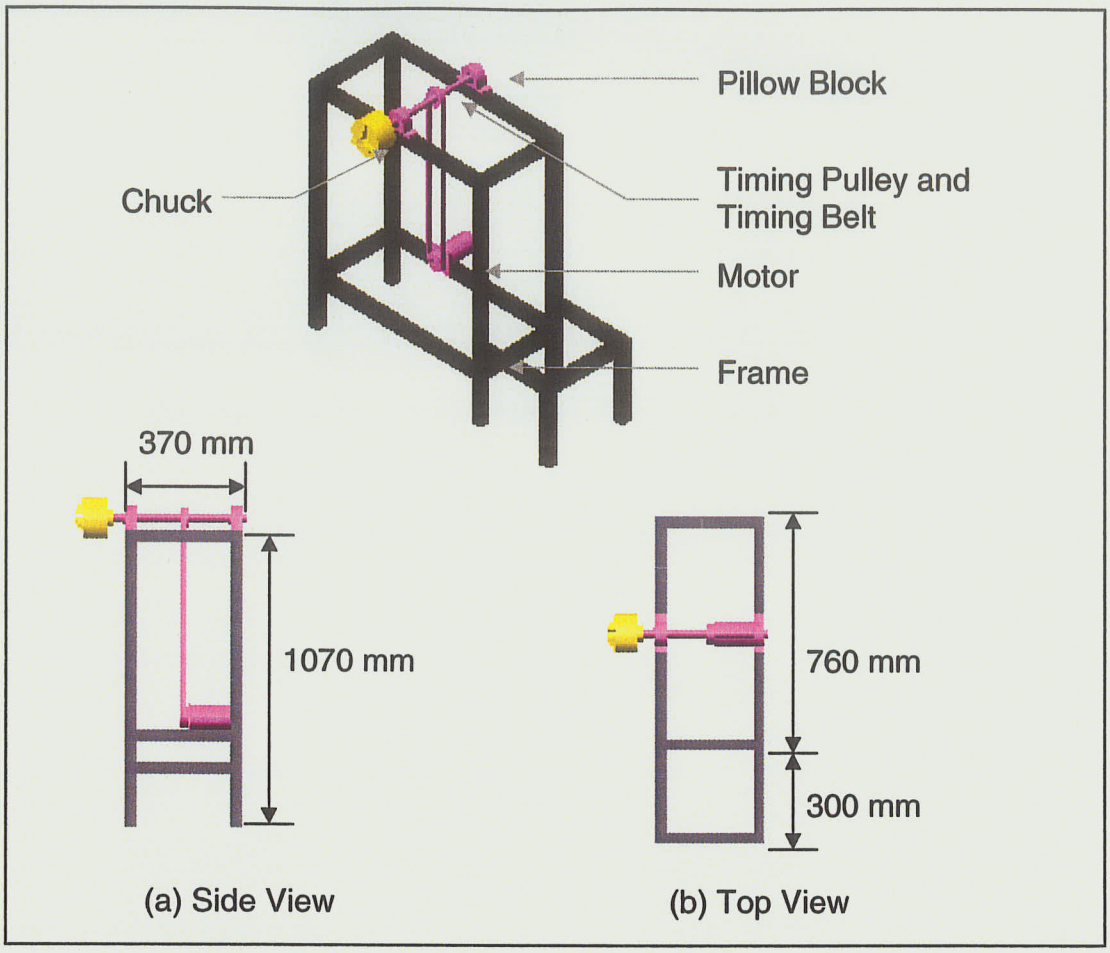

Figure 3-6 Schematic of mandrel transmission system

The carriage was driven by the chain transmission system shown in **Figure 3-7**. Two C250x23 steel channels were used to form the chain box, which is used to protect the chain transmission from resin during winding. They were bolted to the frames at both ends. On the top of the C250x23 steel channels, a 1/4 inch (6.35 mm) steel plate was bolted to the top of the channels and then two L25x25x3.2 angles were welded to the steel plate to form a V-rail for the carriage. This set up provides stability to the carriage. There were two shafts at both ends of the chain box, which were supported by pillow blocks. One side of

the chain box was used as a driven end, where the servo motor was connected to the shaft by coupling connector. The chain ran through the sprocket, which was placed at the middle of the shaft on both sides of the chain box. The carriage frame, which was run on four 76 mm double rubber wheels, was connected with the chain by using the steel figure shown in **Figure 3-7**. Double rubber wheels were used because it provided the stability for the carriage while it moved alone the V-rail. The servo motor, which was connected to the controller and computer, controls the movement of the carriage through the chain.

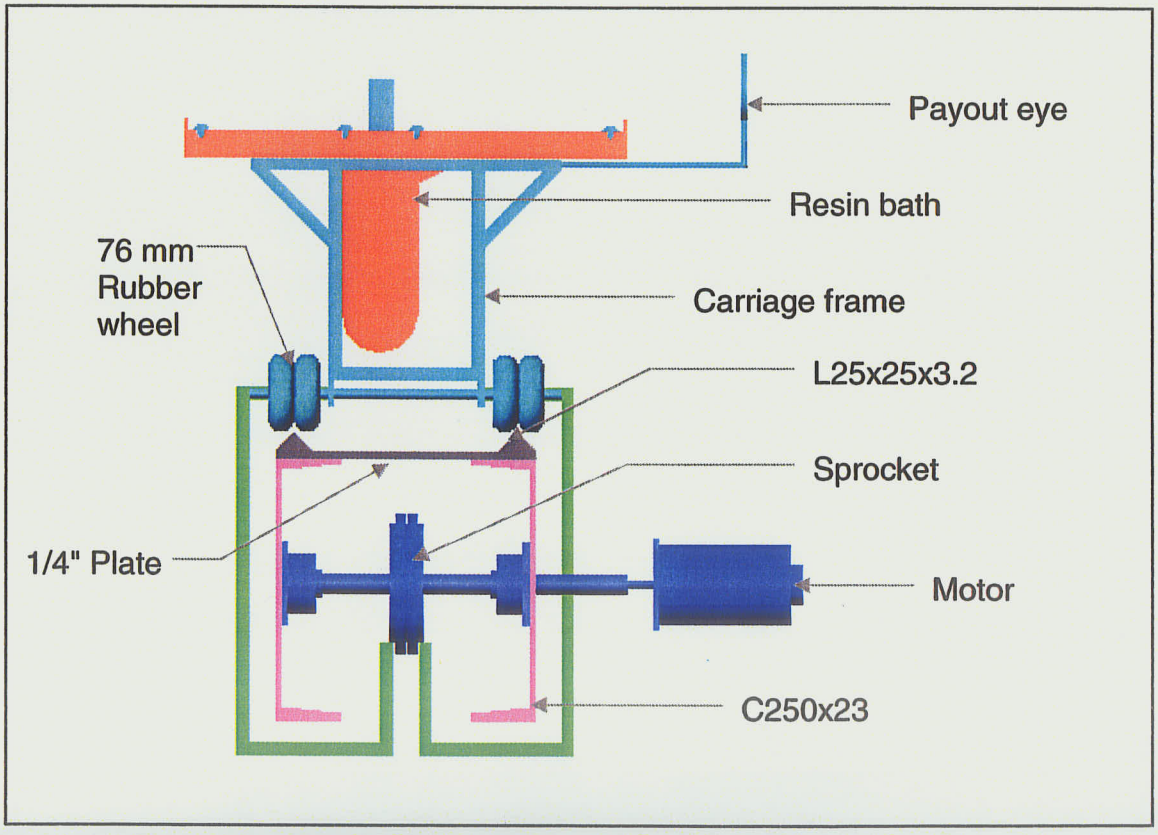

Figure 3-7 Chain transmission system

3.4 PROGRAMING MOTION

The DMC-1425 is a two-axis controller and uses both X and Y axes. The DMC-1425 provides several modes of motions, including independent positioning and jogging, coordinated motion, electronic cam motion, and electronic gearing. The independent axis positioning motion was chosen since each axis used was independent and the motion followed the prescribed velocity profile. This mode of motion and the example of winding application are discussed below.

3.4.1 Independent Axis Positioning

In this mode, motion between the specified axes is independent, and each axis follows its own profile. The user specifies the desired absolute position (PA) or relative position (PR), stew speed (SP), acceleration ramp (AC), and deceleration ramp (DC), for each axis. At the beginning, the DMC-1425 profiler generates the corresponding trapezoidal or triangular velocity profile and position trajectory. The controller determines a new command position along the trajectory every sample period until the specified profile is complete. Motion is complete when the last position command is sent by the DMC-1425 profiler. It should be noted that the actual motor motion may not be complete when the profiler has been completed; however, the next motion command may be specified.

The begin command (BG) can be issued for all axes either simultaneously or independently. X and Y axis specifiers are required to select the axes for motion. When no axes are specified, this causes motion to begin on all axes.

The speed (SP) and the acceleration (AC) can be changed at any time during motion; however, the deceleration (DC) and position (PR or PA) cannot be changed until motion is complete. The motion is complete when the profiler is finished, not when the actual motors is in position. The stop command (ST) can be issued at any time to decelerate the motor to a stop before it reaches its final position.

An incremental position movement (IP) may be specified during motion as long as the additional move is in the same direction. If the user specifies the desired position increment, n, the new target is equal to the old target plus the increment, n. Upon receiving the IP command, a revised profile will be generated for motion towards the new end position. The IP command does not require a begin (BG). It should be noted that if the motor is not moving, the IP command is equivalent to the PR and BG command combination. The basic command summary is given in **Table 3-2.**

Table 3-2 Basic command for the winder

Command	Description
PR X,Y	Specifies relative distance
PA X,Y	Specifies absolute position
SP X,Y	Specifies slew speed
AC X,Y	Specifies acceleration rate
DC X,Y	Specifies deceleration rate
BG XY	Starts motion
AM XY	Trippoint for profiler complete
ST XY	Stops motion

3.4.2 Example of Winding Application

In this section, an example using independent axis positioning for winding application is presented. For the winding application, there are two main motions that need to be considered. The first motion is the rotation of the mandrel, defined as X, while the second motion is the linear motion of the carriage, defined as Y. Therefore, for a later motion the user needs to determine the relationship between a rotation of the motor and a linear movement of the carriage. It should be noted that one revolution of the motor shaft is equal to 4,000 counts. For a circumferential winding application, the user needs to

determine the bandwidth of the fiber feeding in order to calculate how much the carriage needs to move when the mandrel rotates for one revolution. The example of the input command for circumferential winding for the controller is given below, assuming the bandwidth of the fiber is equal to 20 mm, the relationship between a rotation of the motor and a linear movement of the carriage is equal to 12.5 counts per mm, and a mandrel has 2500 mm in length. This example specifies a relative position movement on X and Y axes. **Figure 3-8** shows the velocity profiles for the X, and Y axes.

Instruction	**Description**
# CIRCUMFERENTIAL	Label
DP 0,0	Define the current position as zero
SP 4000,250	Specify speed of 4000 and 250 counts per second
AC 400000,25000	Specify acceleration rate of 400000 and 25000 counts per sec^2 for the X and Y axes
DC 400000,25000	Specify deceleration rate of 400000 and 25000 counts per sec^2 for the X and Y axes
PR 500000,31250	Specify relative position of 500000 and 31250 counts for the X and Y axes
BG XY	Begin motion on X and Y axes
AM XY	Wait for motion on X and Y axes to be done
WT 500,500	Wait 500 milliseconds for all axes
EN	End program

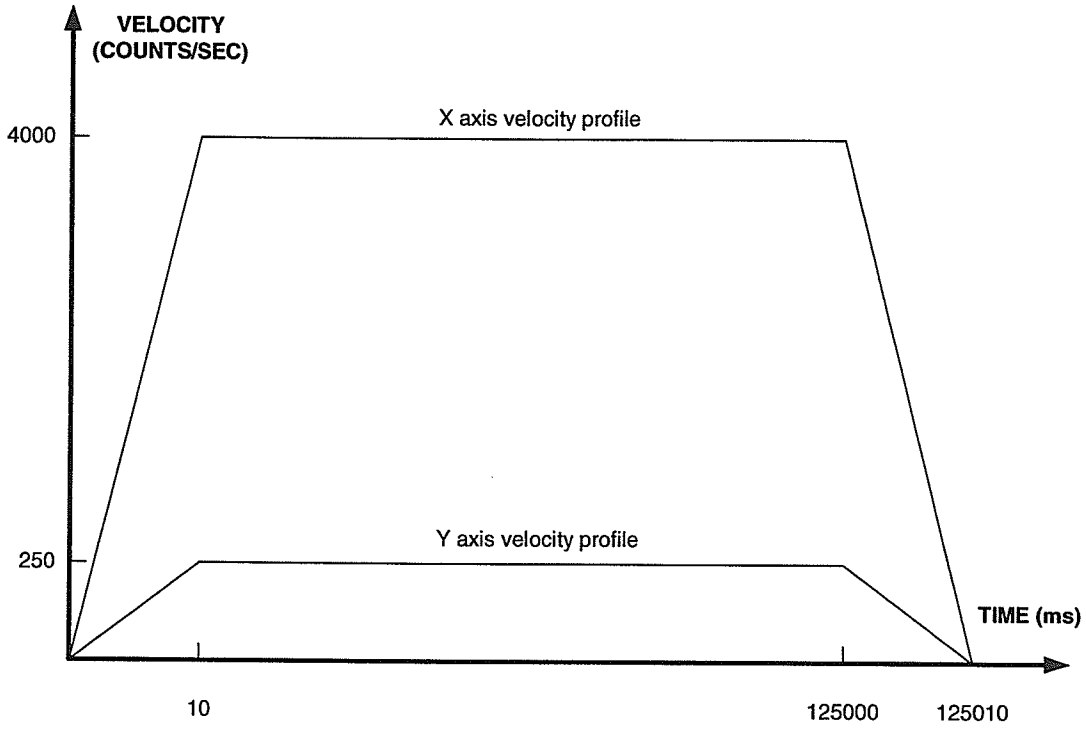

Figure 3-8 Velocity profiles of XY

As shown in **Figure 3-8**, the X and Y axis velocity have a trapezoidal profile and both axes accelerate to the specified speed at the same time. The speed ratio between X axis (the mandrel) and the Y axis (the carriage) was constant. This provides the circumferential winding position for the fiber.

CHAPTER 4

EXPERIMENTAL PROGRAM

4.1 GENERAL

The main objective of the research program was to evaluate the structural performance of segmented FRP wind turbine towers. This objective was accomplished through a comprehensive experimental program at the W.R. McQuade Structural Engineering Laboratory of the University of Manitoba. The design of wind turbine towers is typically controlled by the bending capacity, thus bending tests were performed to evaluate the structural performance of the proposed FRP segmented towers. The specimens were tested to failure. The specimens were manufactured using the filament winding process at the FRP Laboratory of the University of Manitoba. A description of the tested specimens, the test setup, and the instrumentation used are presented in detail in this chapter. A description of the manufacturing process is also presented.

The experimental program was carried out in three phases. Phase I involved the testing of two single FRP cells under lateral loading to obtain the ultimate

strength and to observe the mode of failure. In Phase II, single FRP cells with various lengths were tested under compression. Phase III involved the testing of two FRP multi-cell towers. The specimens were tested as cantilever under static loading. One of these was subsequently repaired and retested. Standard coupons were also fabricated and tested according to current standards in order to determine the material properties of the FRP for use in the numerical analysis.

The specimens were given an alphanumeric designation. All designations begin with the letter P followed by a number indicating the experimental phase. For instance, P1 refers to specimens in Phase I, while P3 refers to specimens in Phase III. In Phase I, the specimens were designated as P1-x, where x indicates the specimen number in Phase I. In Phase II, the single FRP cells were designated as P2-y-x, where y indicates the length of the cell in millimeters. For example, P2-1780-2 is the second specimen tested in Phase II with a 1780 mm length. For the specimens tested in Phase III, the numbering system is the same as that of the Phase I.

4.2 MANDREL FABRICATION

Before the FRP towers components can be manufactured, mandrels need to be fabricated to the designed dimensions. Fabrication of the mandrels is described below.

Two mandrels were fabricated from composite materials: one is to be used for the fabrication of the cells for the upper section of the tower and another one is to fabricate the cells for the lower section. The composite construction provided an economical, lightweight, and reusable mandrel.

The dimensions of the mandrel for the upper section cells are shown in **Figure 4-1**. Four 2x6 in (50.8x152.4 mm) cedar wood planks were used to form the mandrel shape. Each plank was trimmed to a thickness of 1.5 in (38.1 mm) and the edges were then cut at 22.5 degrees, as shown in **Figure 4-2**. After the planks were trimmed and cut to the required dimensions, the upper end of the planks were cut to the required taper ratio and then the pieces were connected together to construct the mandrel. Two 1 in (25.4 mm) diameter threaded steel shafts were used at both ends of the mandrel to serve as a self-extraction drive mechanism. In addition, a 1 in diameter fiber glass tube was used in the middle of the mandrel to provide stiffness, as shown in **Figure 4-2**. The self-extracting drive mechanism, which was installed at both ends of the mandrel, is composed of a nut which was mounted at the end of the threaded shaft and a ball bearing which was placed in front of the fiber glass tube, as shown in **Figure 4-3**. This mechanism allows the threaded shaft to rotate freely during the specimen removal process.

Each corner of the wood box comprising the inner part of the mandrel was trimmed to the designed radius. This helps to prevent the fibers from breaking

during the winding process. Two layers of bi-directional glass fiber woven sheet were wrapped around the wooden box at ±45 degrees. In addition, epoxy resin mixed with carbon power and thickened with silica powder was applied on the surface of the mandrel. After the resin was completely cured, the surface of the mandrel was manually sanded and polished to a perfectly smooth surface finish. A steel plate was attached at each end of the mandrel, as shown in **Figure 4-2**.

The dome end of the mandrel was fabricated from plywood with the required geometry. A drive-nut was welded to a thrust steel plate and then installed at the middle of the dome end. This drive-nut was used to move the dome end and thus remove the specimens from the mandrel after curing. **Figure 4-4** shows the schematic of self-extracting drive incorporated with the dome end to remove the specimens.

The dimensions of the lower section mandrel are illustrated in **Figure 4-5**. The construction of this mandrel was similar to the upper section mandrel. The difference between the two is that the lower section mandrel was fabricated with a sleeve of 9.6 in (24.84 cm) at the top of the mandrel. This sleeve would allow the upper section of the bottom cell to be fabricated in such a way as to fit perfectly inside the lower end of the upper cell. The self-extracting mechanism was similar to the previous mandrel and was installed, as shown in **Figure 4-6**. The sleeve had to be accurately fabricated. This was the most critical task of fabricating this mandrel.

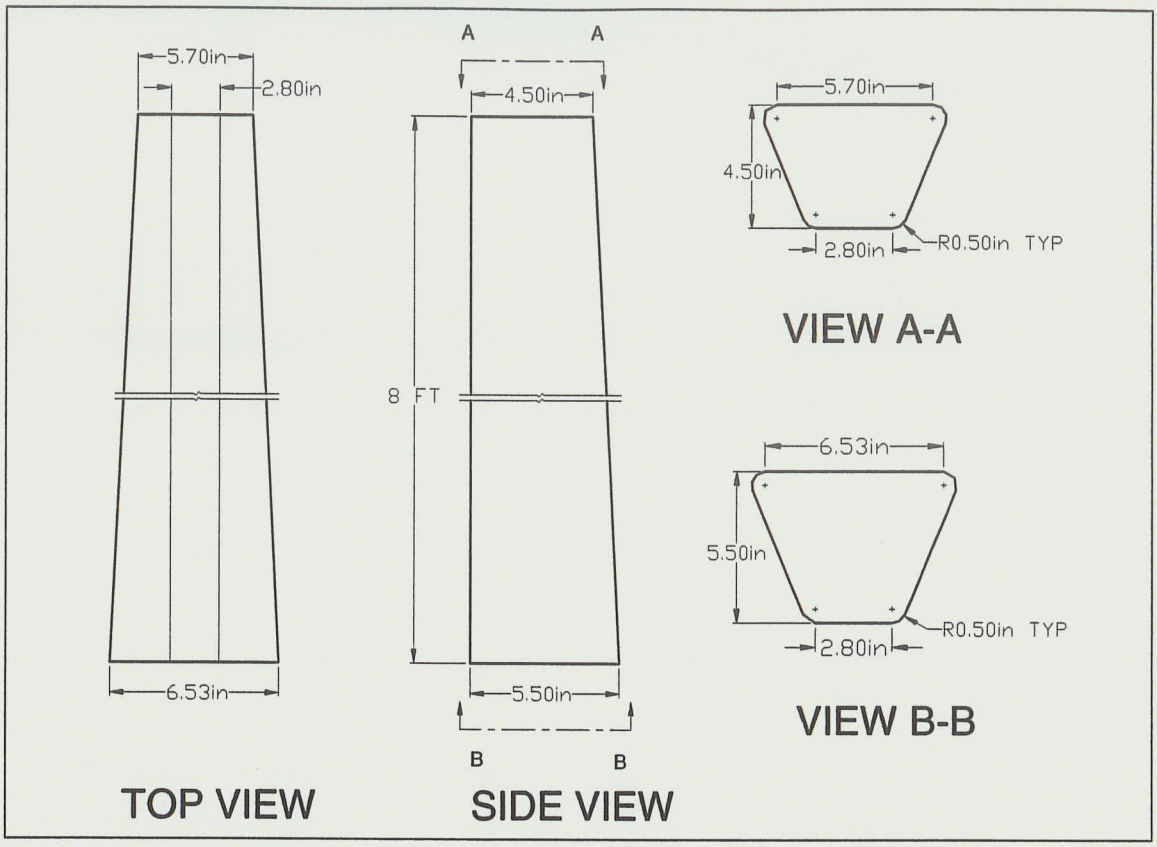

Figure 4-1 Dimensions of upper section of 8-cell scaled tower mandrel

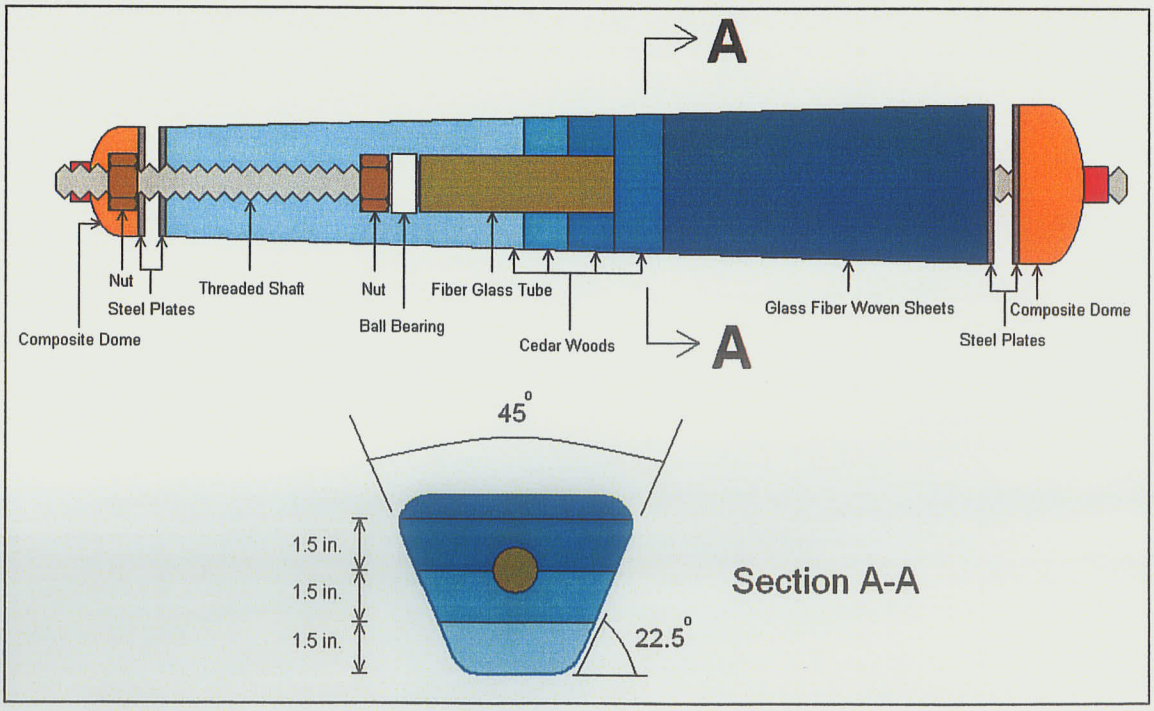

Figure 4-2 Schematic of upper section 8-cell scaled tower mandrel

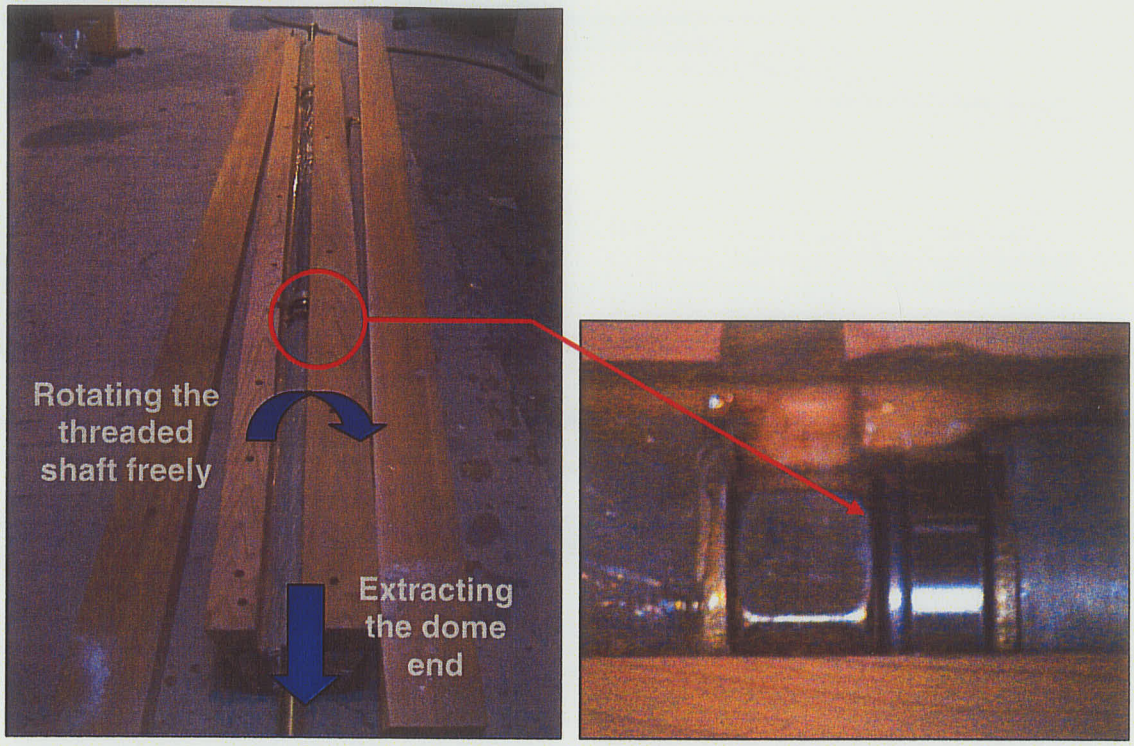

Figure 4-3 Extracting drive mechanism

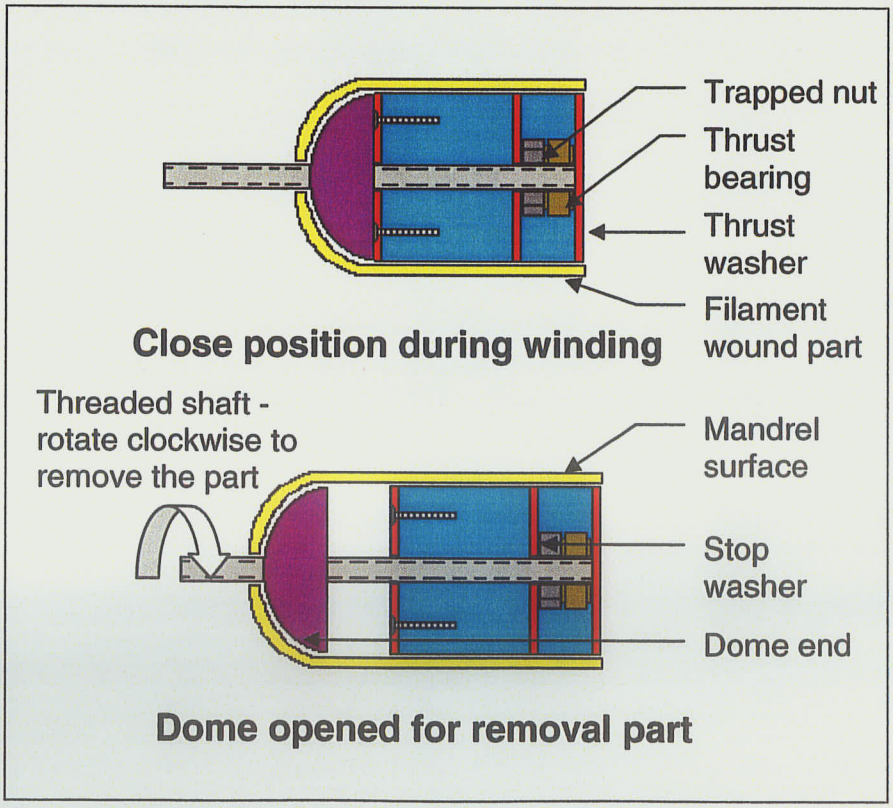

Figure 4-4 Schematic of self-extracting drive

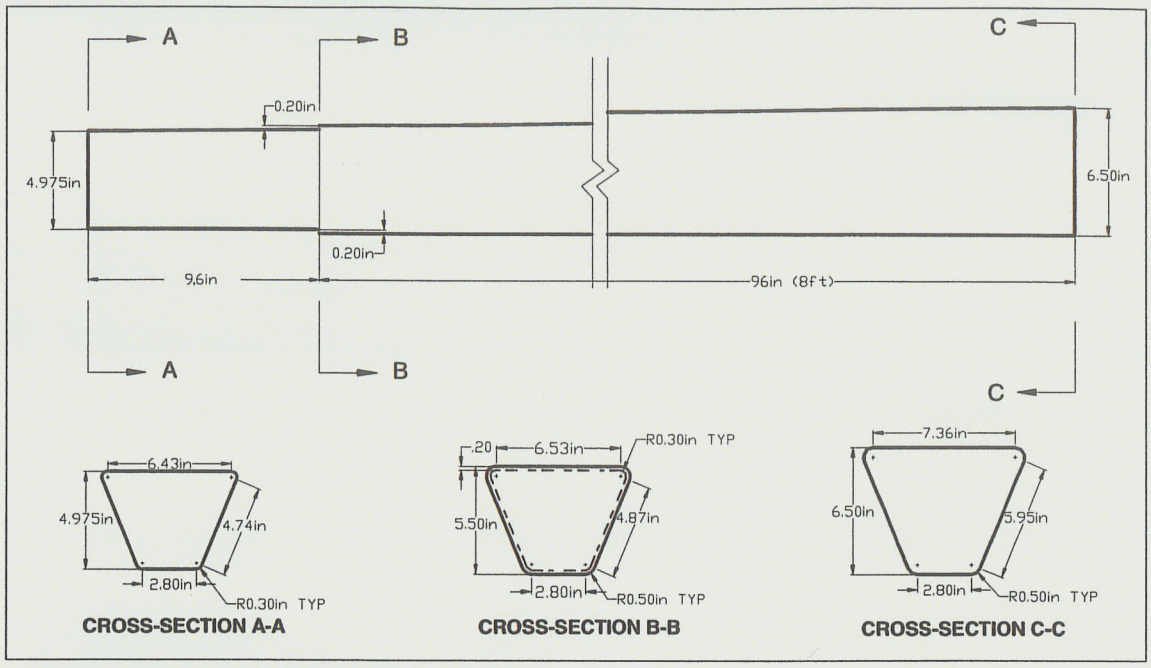

Figure 4-5 Dimensions of lower section of 8-cell scale tower mandrel

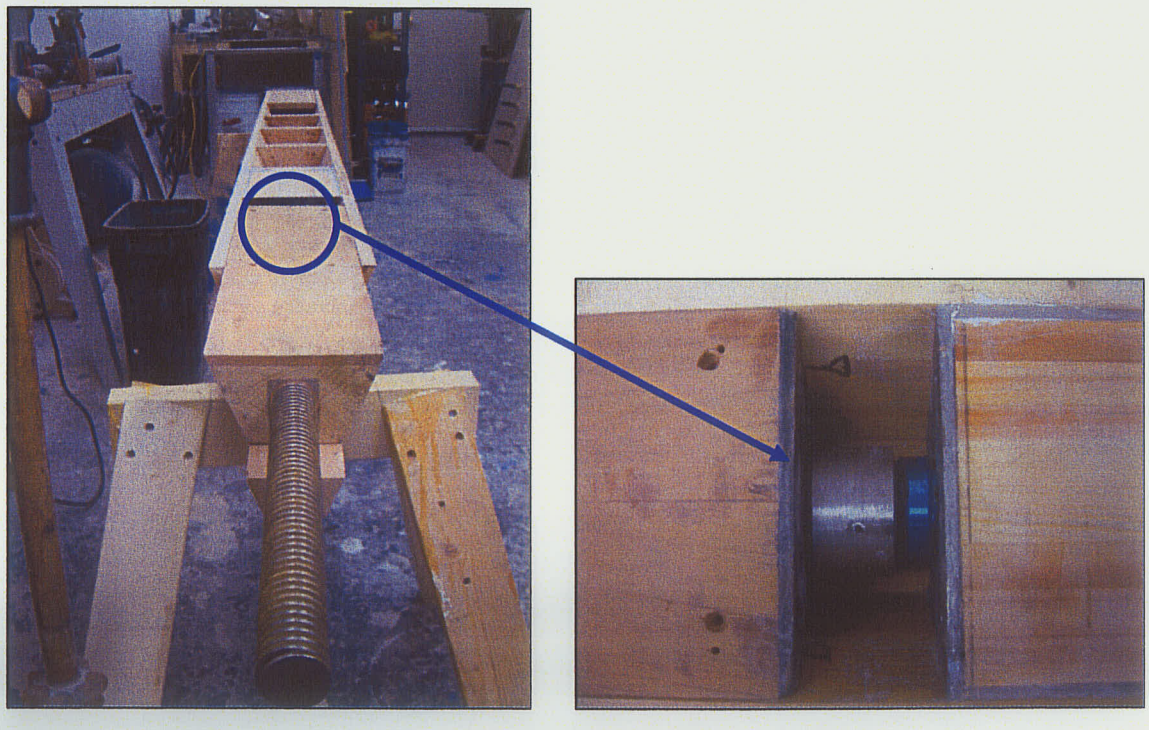

Figure 4-6 The extracting drive mechanism

4.3 MANUFACTURING OF SINGLE CELL SPECIMENS

Prior to fabricating the individual cells, several coats of a mold cleaner, a mold sealer, and a releasing agent were applied to the surface of the mandrel and then polished to a perfect smooth surface, as shown in **Figure 4-7**. After that the Mylar, a plastic sheet, was wrapped around the mandrel, as shown in **Figure 4-8**. This sheet prevents the FRP having a direct contact with the surface of the mandrel and helps the removal of the specimen from the mandrel. The fiber layer sequence of the filament wound cell was -86, 86, 0, -86, and 86 degrees. As shown in **Figure 4-9**, first, a layer of ±86 degrees of glass fiber (1100 TEX) saturated with West System 105/ 205 epoxy resin was wound using the robotic filament winder. The 1258 g/m^2 unidirectional glass fiber mats (0 degree fibers) were then cut to required length and saturated with epoxy resin as shown in **Figure 4-10**. Once the fabric was saturated, it was rolled in the longitudinal direction, unrolled and wrapped around the mandrel as shown in **Figure 4-11**. There was approximately one inch overlap of the mat at the small face of the mandrel. This technique was chosen in order to provide 0 degree fiber orientation (longitudinal direction) and to also ensure a consistent thickness throughout the specimens. Then, a saturated glass fiber string was used to hold the fabric in place during the winding. Finally, a layer of ±86 degrees of saturated glass fiber was wound, as shown in **Figure 4-12**. The cell specimen was left on the mandrel for approximately 8 hours to cure. Once the specimen

cured, it was removed from the mandrel, as shown in **Figure 4-13**. The finished cell is shown in **Figure 4-14**.

Figure 4-7 Applying releasing agent on the surface of the mandrel

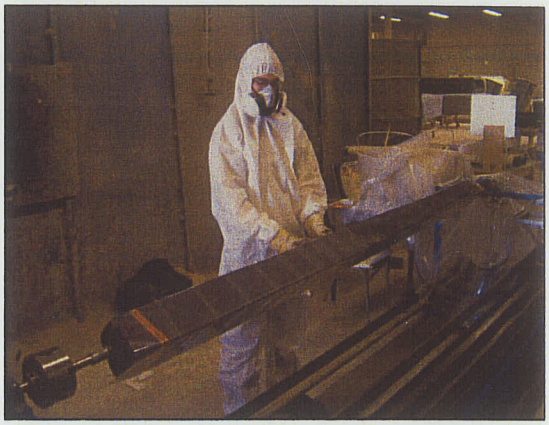

Figure 4-8 Wrapping Mylar on the surface of the mandrel

Figure 4-9 Winding -86 degree layers

Figure 4-10 Preparing unidirectional glass fiber woven sheet

Figure 4-11 Wrapping the unidirectional sheet

Figure 4-12 Winding 86 degree layers

Figure 4-13 Removing finished cell specimen

Figure 4-14 Finished cell specimens

4.4 FABRICATION OF JOINTED TOWER SPECIMENS

The tower investigated in this experimental study was fabricated in two sections each consisting of eight cells, as shown in **Figure 4-15**. The upper section of the tower, shown in **Figure 4-16**, had a height of 8 ft (2.44 m), a diameter at the base of 19.38 in (49.22 cm), a diameter at the top of 17.38 in (44.15 cm), and a constant inner diameter of 8.38 inches (21.29 cm). The lower section of the

tower, shown in **Figure 4-17**, had a height of 8 ft (2.44 m), a diameter at the base of 21.38 in (54.31 cm), a diameter at the top of 19.38 inches (49.22 cm), and a constant inner diameter of 8.38 in (21.29 cm). A sleeve of 9.6 in (24.38 cm) was fabricated at the top of the cells in the lower section. This allows the cells in the upper section to joint with the cells in the lower section. The length of the sleeve was 1/10 of the length of the lower section as recommended by previous research (Philopulos, 2002).

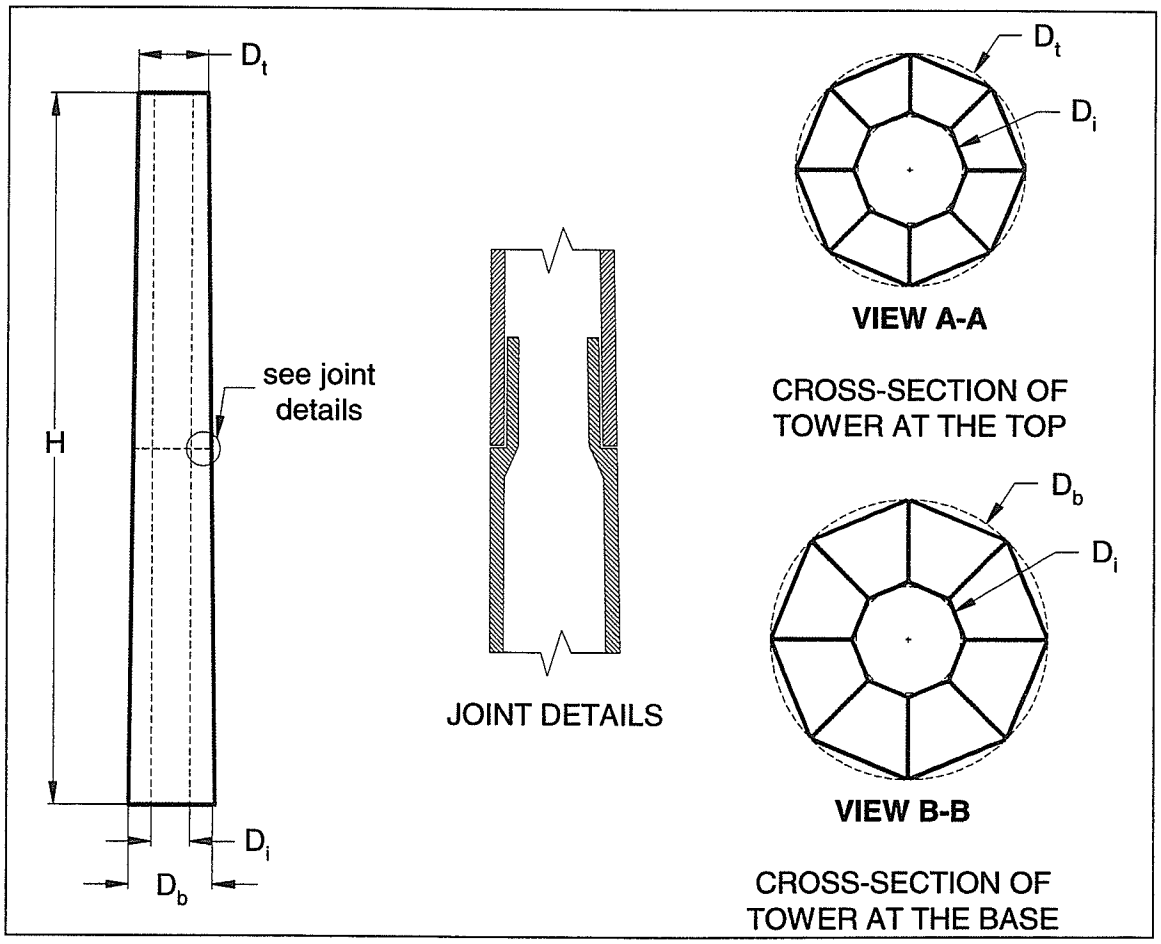

Figure 4-15 Eight-cell jointed tower specimen

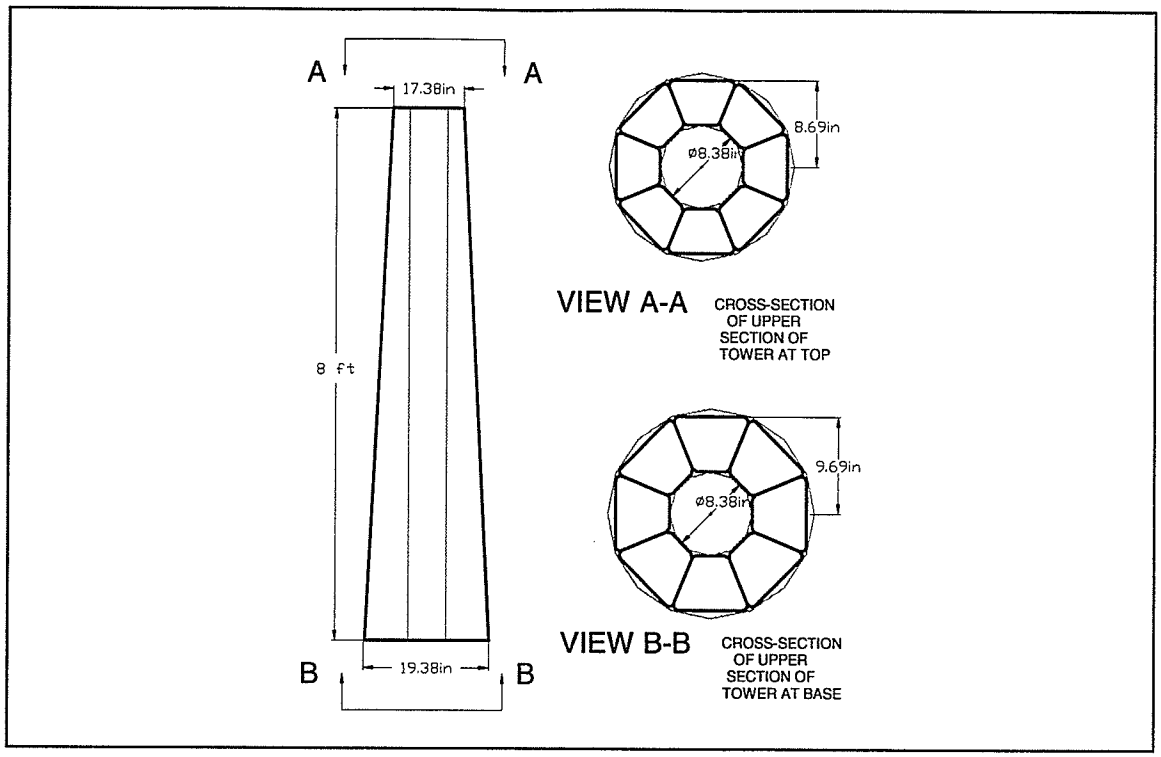

Figure 4-16 The upper section of 8-cell scaled tower

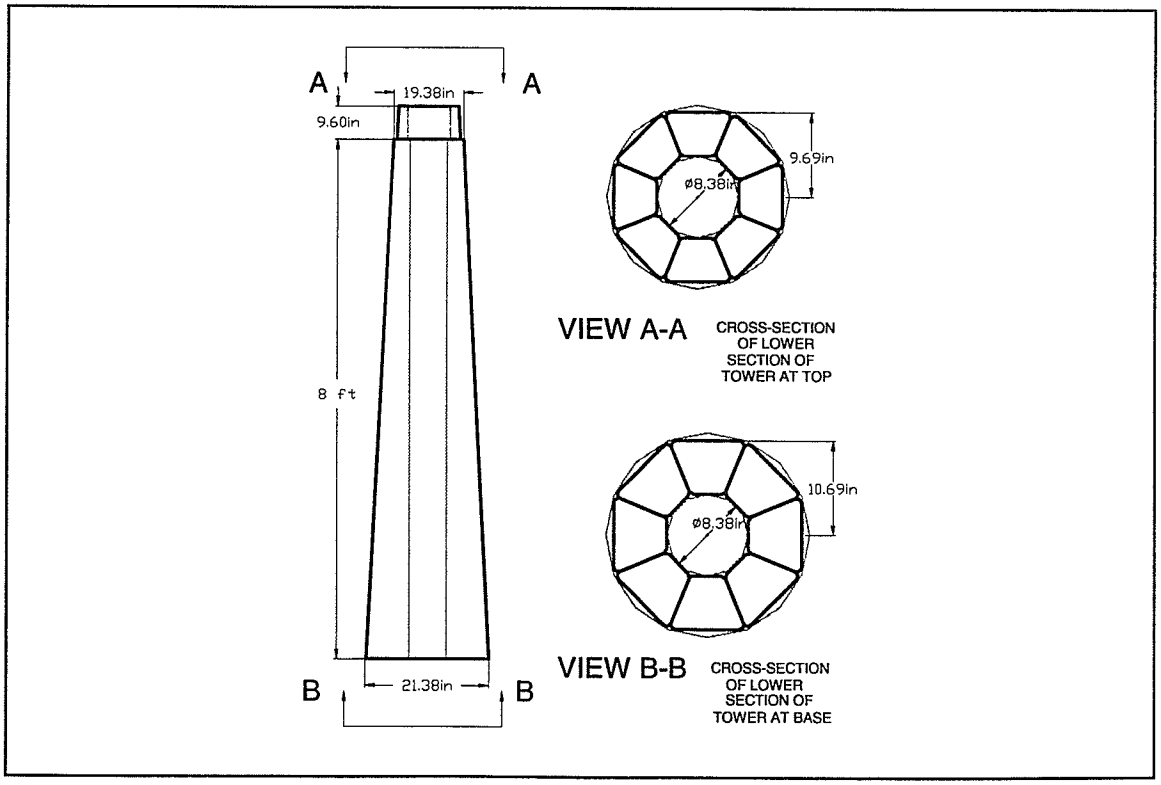

Figure 4-17 The lower section of 8-cell scaled tower

The foundation of the tower was designed specifically for multi-cell jointed towers. It comprises of a concrete base with inserts/sleeves at the top which allow the tower cells to be inserted in a tight fit fashion, as shown in **Figure 4-18**. After fabricating all cell specimens, the cells of the lower section were placed into the reinforced concrete foundation, as shown in **Figure 4-19**. Epoxy resin thickened with silica powder was applied on the contact surface of each cell installed before the next cell was inserted into the foundation. The same process was used until all eight cells of the lower section were installed. A steel strap was then placed at the middle of the lower section to hold the cells in place before the upper section cell was erected, as shown in **Figure 4-20**. The same procedure used in the lower section was repeated for the upper section. Epoxy resin was applied in the sleeves of the cells in the lower section before the cells of the upper section were installed. After all cells in the upper section were installed, several steel straps were placed at different locations along the height of the tower to hold the cells in position, as illustrated in **Figure 4-21**. The steel straps were removed after the epoxy was cured. Then two layers of 340 g/m^2 bi-directional glass fiber tape saturated with West System epoxy resin (205/105) were wrapped around the tower at different locations along the height of the tower to provide the confinement.

Figure 4-18 Foundation of the eight-cell jointed tower

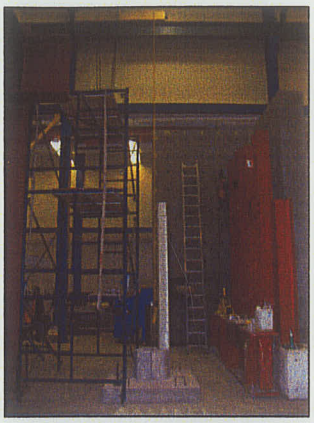

Figure 4-19 Placing the first cell in the lower section

Figure 4-20 Placing the first cell in the upper section

Figure 4-21 Completed jointed tower

4.5 TESTING PROGRAM

The testing program consisted of three phases, as described in Section 4.1. A detailed description of the testing in each of those phases is given in subsequent sections. Additionally, a description of the tests conducted in order to determine the material properties of the FRP used in the experimental program is also given.

4.5.1 Phase I

Phase I involved the testing of two single FRP cells as cantilevers under lateral loading. These tests were conducted in order to evaluate the structural performance of the single cells and to, also, evaluate the finite element model that was developed for determining the capacity of composite cells. The specimens had a measured average length of 8 ft (2.44 m). The dimensions are shown in **Figure 4-22**. The fiber orientations of each cell were -86, +86, 0, -86, and +86. The measured average shell thickness of the cells was 4.50 mm.

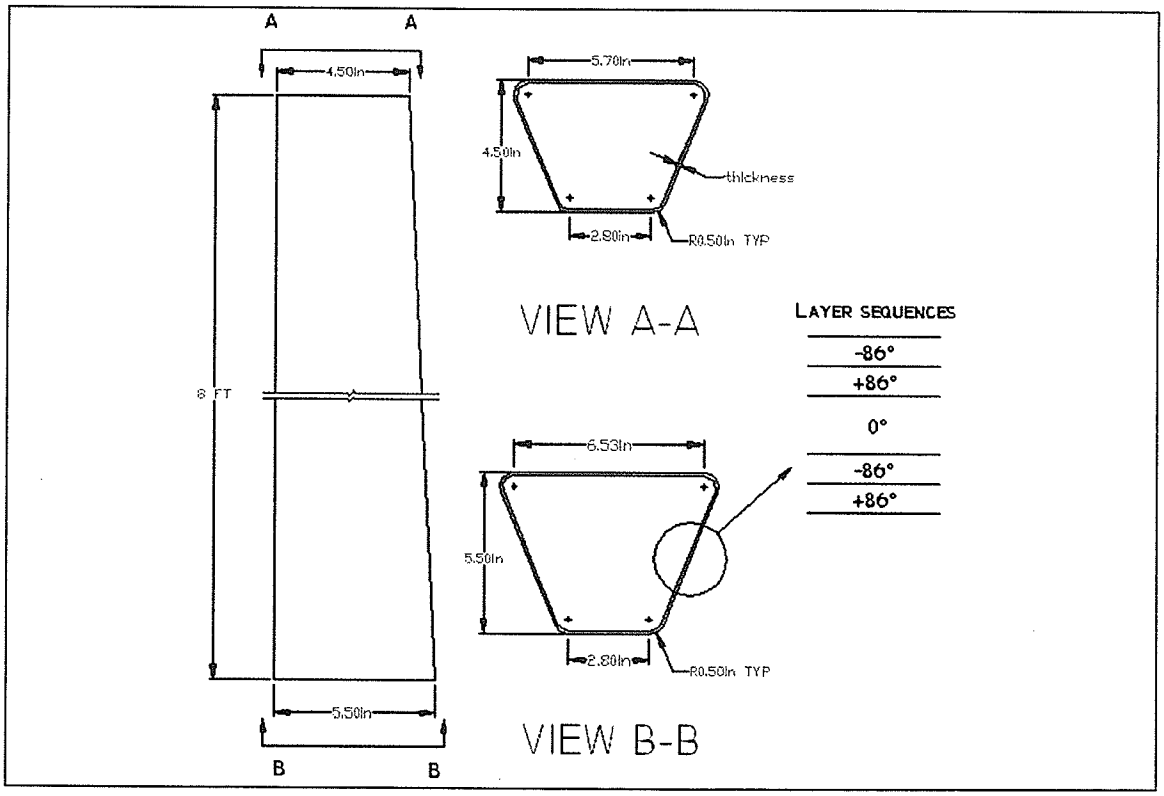

Figure 4-22 Dimensions of Phase I specimens

The specimens were tested using the test set-up shown in **Figure 4-23**. The specimens were inserted horizontally into a composite sleeve, which was attached to a testing fixture and which in turn was rigidly mounted to the structural reinforced concrete wall of the structural laboratory. The load was applied vertically through a cable attached to the specimens approximately 78 mm from the tip. The load was monitored through an electronic load cell.

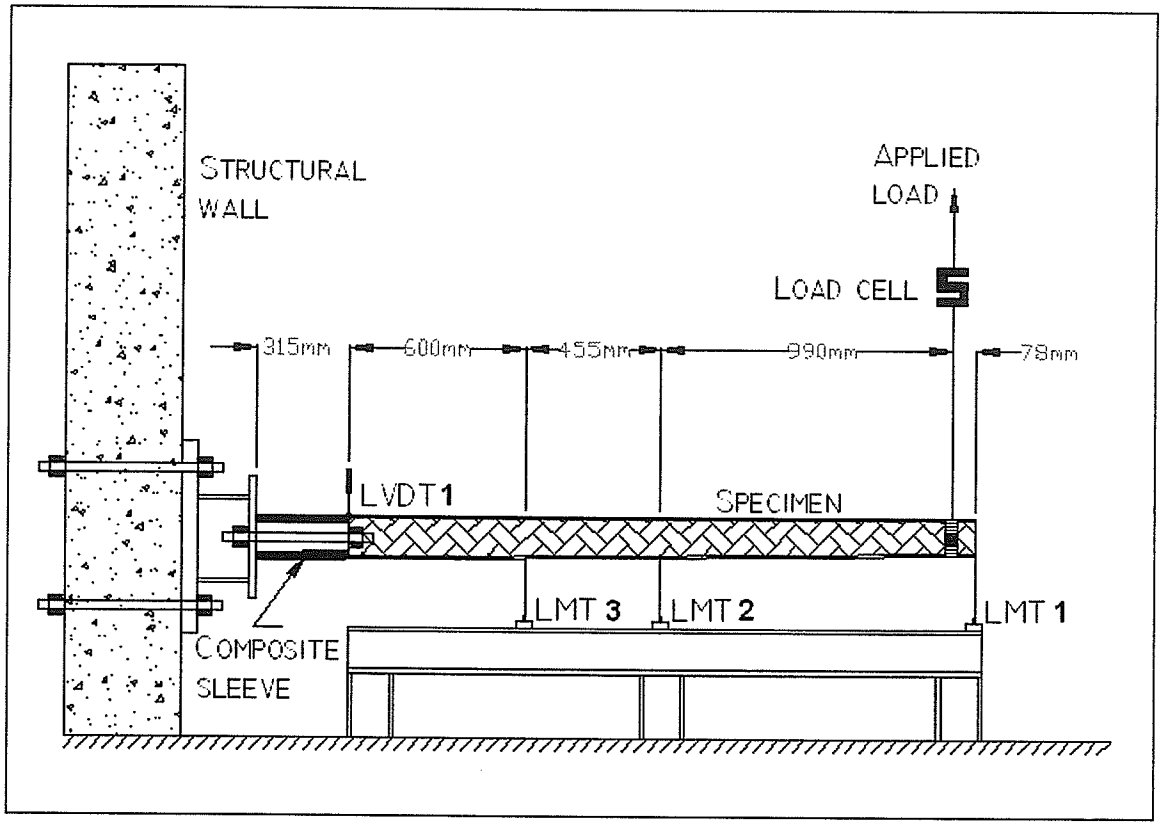

Figure 4-23 Schematic drawing of Phase I test set-up

The instrumentation consisted of:

a) a load cell to measure the applied load at the top of the specimen;

b) transducers to measure the vertical displacement at various positions of the specimen; and,

c) strain gages to measure the horizontal strains along the specimen at various positions.

The load was measured with a pre-calibrated electronic load cell having a load capability of 44 kN. The vertical deflections were monitored through an electronic linear measurement transducers (LMT) mounted on the fixed steel beam approximately 40 mm away from the specimens. The stroke range of the LMTs was 2500 mm. Three LMTs were used to measure the vertical displacement at distances 915, 1370, and 2438 mm away from the sleeve base, as shown in **Figure 4-24**.

To monitor the deformation of the sleeve, an electronic linear variable displacement transducers (LVDT) was mounted approximately 315 mm away from the base support. This deformation was used to obtain the actual displacement of the specimens tested.

Twelve electrical resistance strain gages were mounted on each specimen. The strain gages had a 5 mm gage length and 120 ohm electrical resistance. Six of the stain gages were placed on the compression side and the other six on the tension side of the specimens at distances 315, 467, and 619 mm away from the base. Three of the strain gages on the compression side were placed on the

middle of the top surface (T) and the other three on the top corner (CT) of the specimen. Similarly, three of the strain gages on the tension side were placed on the middle of the bottom surface (B) and the other three on the bottom corner (CB) of the specimen, as shown in **Figure 4-24**.

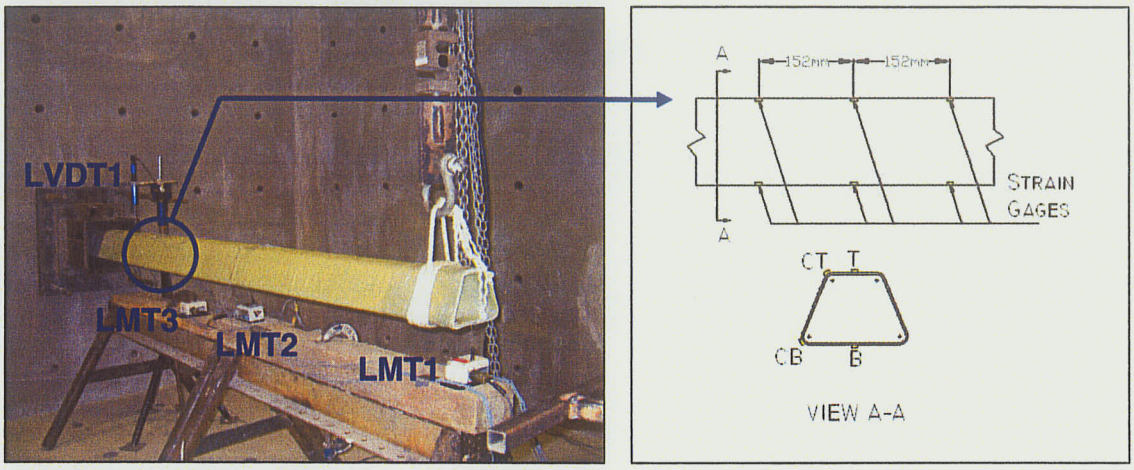

Figure 4-24 Phase I instrumentation

The load cell, the LMTs, the LVDT, and the strain gages were connected to a 64 channel Data Acquisition System to monitor and record all data onto a hard drive of a Pentium II PC using Labview software. Initial readings of all instruments were set to zero. The data were sampled every one second and plots of load versus deformations were on display during testing. Visual observations were also made during the test and the load was applied till a complete failure of the specimen occurred.

4.5.2 Phase II

In Phase II, single FRP cells were tested in compression. These tests were conducted in order to evaluate the buckling behavior of the single cells. Two specimens, 1280 mm and 1780 mm long, were tested. The dimensions of the specimens were similar to those of the specimens in Phase I. The fiber orientations of each cell were -86, +86, 0, -86, and +86. The measured average shell thickness of the cells was 4.50 mm.

The two specimens were tested using the test set-up shown in **Figure 4-25**. The compressive load was applied via the MTS 445 Servo Hydraulic Testing Machine. Pinned supports were used at both ends of the specimen.

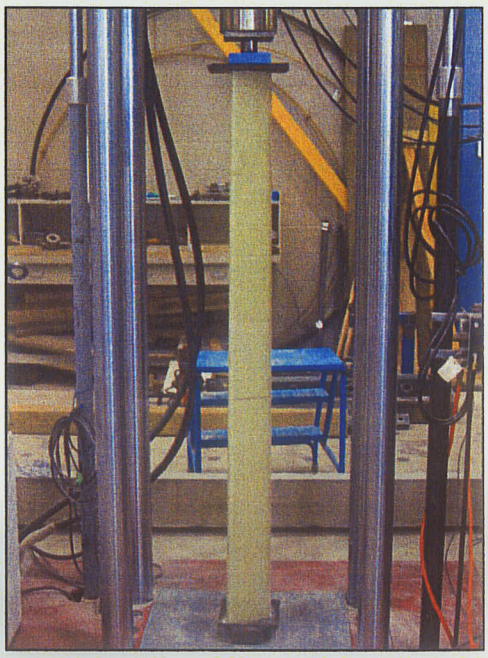

Figure 4-25 Composite single cells under compression

Initial readings of the load and the vertical displacement were set to zero. The load and vertical displacement were monitored and recorded onto a hard drive of a Pentium II PC using Labview software through a Data Acquisition System. The data were sampled every one second and plots of load versus deformations were on display during testing. Visual observations were also made during the tests and the load was applied until a complete failure of the specimen occurred.

4.5.3 Phase III

Phase III involved the testing of two jointed FRP towers under lateral loading. The purpose of these tests was to study the structural performance of the eight-cell jointed towers and to verify the finite element model developed for evaluating the structural performance of multi-cell, multi-segment composite towers. One of the specimens tested was subsequently repaired and retested in order to evaluate the effectiveness of a repair technique to restore the original structural performance of the tower.

The manufacturing process of the towers tested is described in details in Section 4.4. The towers tested in Phase III had an average height of 16 ft (4.88 m) from the base. Other dimensions are shown in **Figure 4-26**. As described in Section 4.4, the fiber orientations of each cell were -86, +86, 0, -86, and +86. Because of the way the tower segments were constructed, the stiffeners of the tower segments had double the thickness. Thus the fiber orientation in these stiffeners

was (-86, +86, 0, -86, +86)$_2$. The measured average outer and inner shell thickness of the tower segments was 4.76 mm while measured average stiffener shell thickness was 9.53 mm.

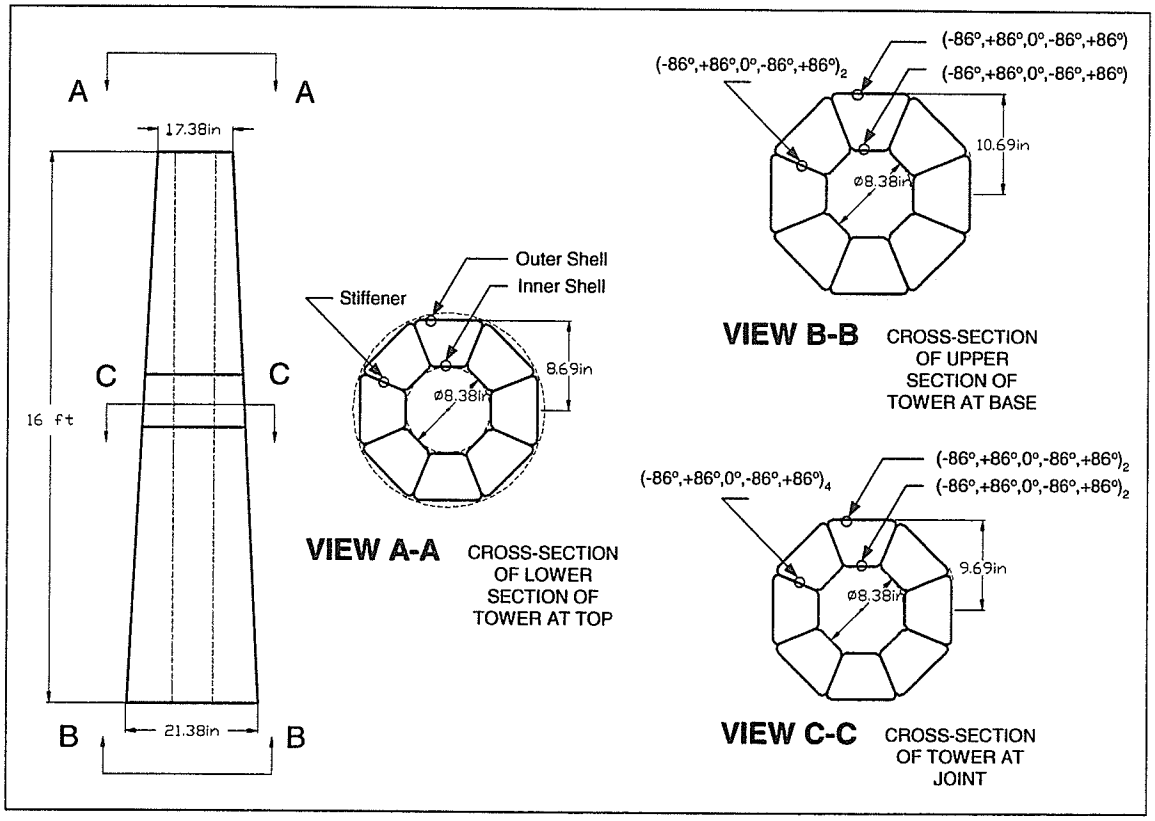

Figure 4-26 Dimensions of Phase III specimens

The towers were tested using the test set-up shown in **Figure 4-27**. The reinforced concrete foundation was rigidly mounted to the reinforced concrete structural floor using four high tensile strength dwydag bars. The horizontal displacements at the tip and the middle of the specimen were monitored through LMTs. Steel wires were used to connect the LMTs and the specimen, as shown in the **Figure 4-27**.

The load was applied horizontally through a sling located 305 mm below the top of the specimen and attached to a steel cable. In order to prevent local deformations at the point where the load was applied, wood stiffeners were placed inside of each cell at the point of application of the concentrated load. The load was monitored through a load cell, as shown in **Figures 4-27** and **4-28**. The end of the steel cable was attached to an electrically operated overhead crane with a capacity of 10 tons through a pulley. The load was applied incrementally by the operator of the overhead crane at a rate of, approximately, 0.50 mm/second.

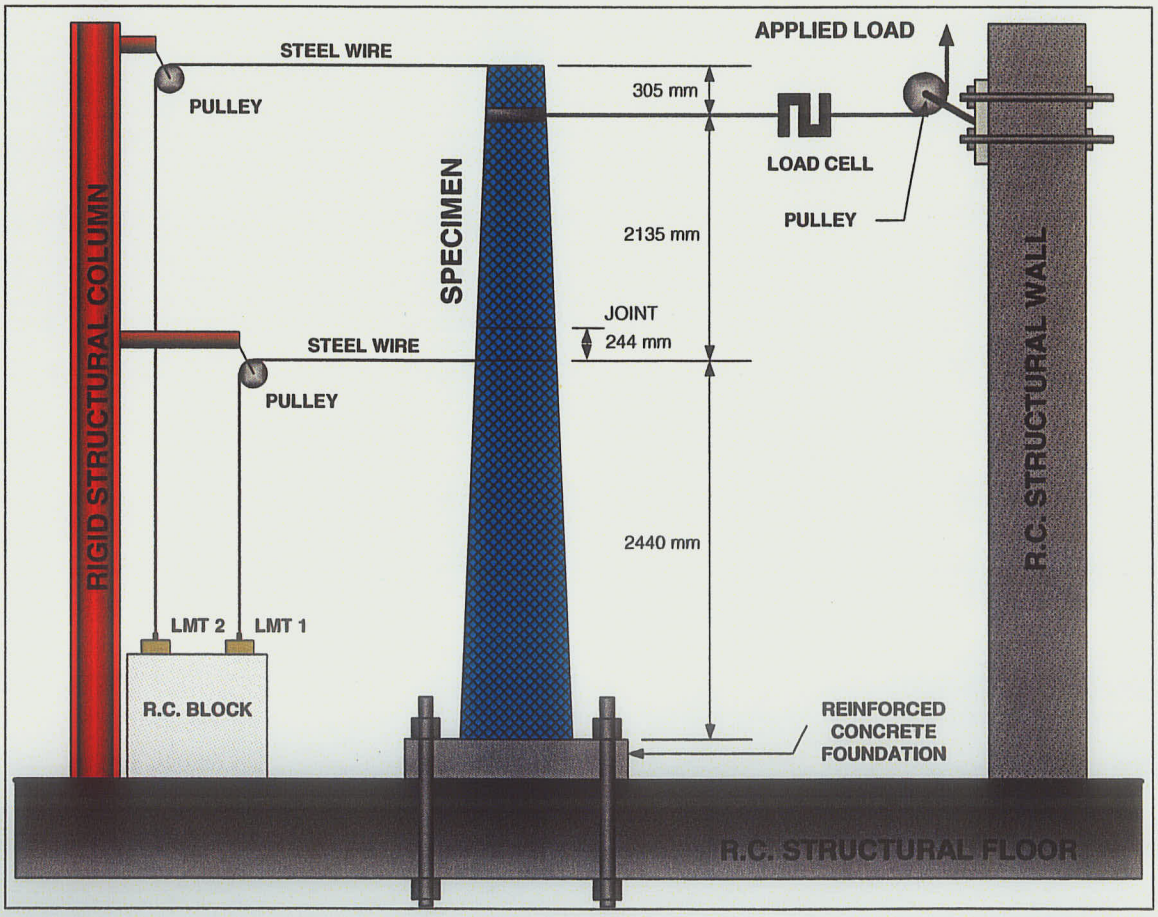

Figure 4-27 Schematic drawing of tower set-up

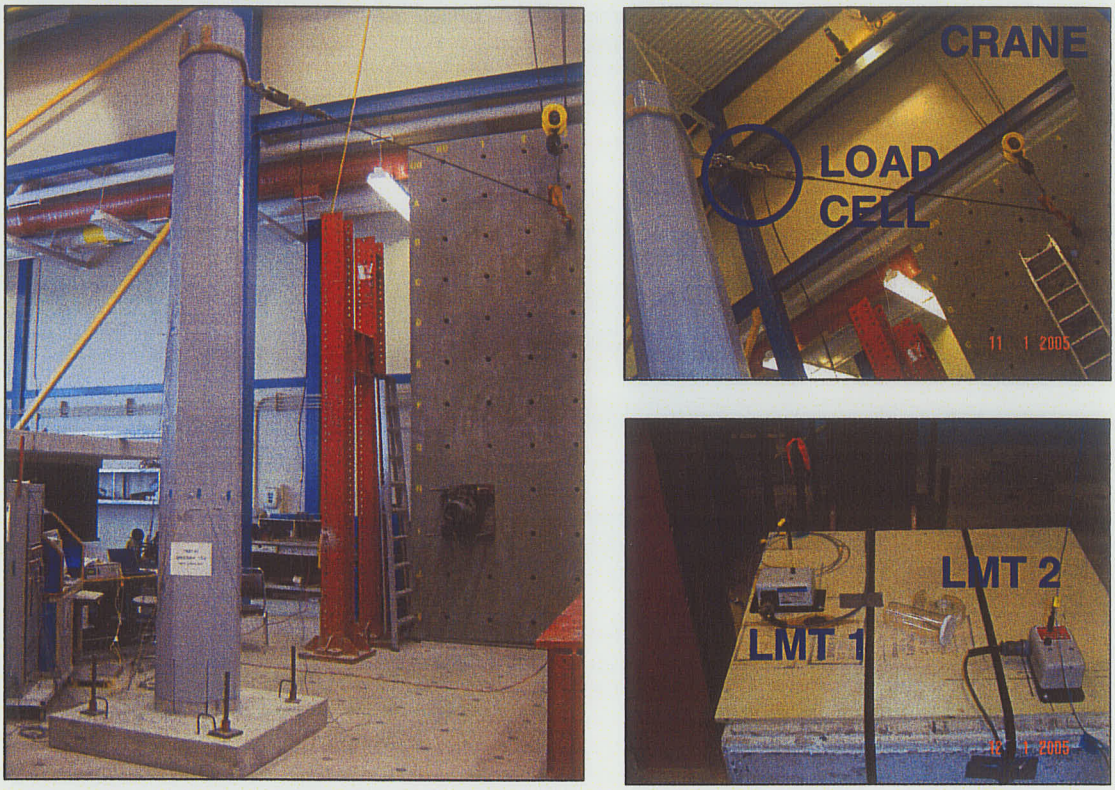

Figure 4-28 Instrumentation of tower

The instrumentation used in this Phase was designed to measure:

a) the applied load at the top of the specimen;

b) the horizontal displacement at the top of the tower and at the joint of the segments; and,

c) the strains along the specimen at various locations on both the compression and the tension sides.

The applied load was measured with a pre-calibrated electronic load cell having a load capability of 44 kN. The horizontal deflections were monitored through electronic linear measurement transducers (LMTs) mounted on the fixed

concrete block. A steel wire was used to measure the deflections. One end of the steel wire was connected to an LMT, while the other end was attached to the specimen through a pulley, as illustrated in **Figure 4-27**. The stroke range of the LMTs was 2500 mm. The two LMTs were attached to the tower specimen at distances 2449 and 4880 mm away from the concrete foundation.

The slip of the tower from its foundation was monitored through electronic linear variable displacement transducers (LVDTs) mounted on a steel plate, as shown in **Figure 4-29**. The LVDTs were located on both the compression and the tension side at the base of the tower. These transducers were used to monitor a vertical movement during the test. The values were used to adjust the horizontal displacement obtained from LMTs and thus determine the actual horizontal displacement of the specimen, as shown in **Figure 4-30**.

Twenty four electrical resistance strain gages were also mounted on each tower specimen. The strain gages had a 5 mm gage length and 120 ohm electrical resistance. The strain gages which were mounted at strategic locations were used to measure the strain in the longitudinal direction. Twelve of the strain gages were placed on the tension side and the other twelve on the compression side of the specimen at heights of 585, 685, 785, 885, 985, 1085, 1185, 2400, 2450, 2565, 2680, and 2730 mm from the base, as shown in **Figure 4-31 (a)**. Two long gauge fiber optic sensors were also used to monitor the longitudinal strain in each specimen. The fiber optic sensors had a 100 mm gauge length

with standard 3 mm jacketing on the lead cable and FC/APC connector. One fiber optic sensor was placed on the tension side and the other on the compression side of the specimen at a height of 785 mm from the base. **Figure 4-31 (b)** shows the installation of the fiber optic sensor on the specimen. The load was applied 305 mm from the tip of the specimen.

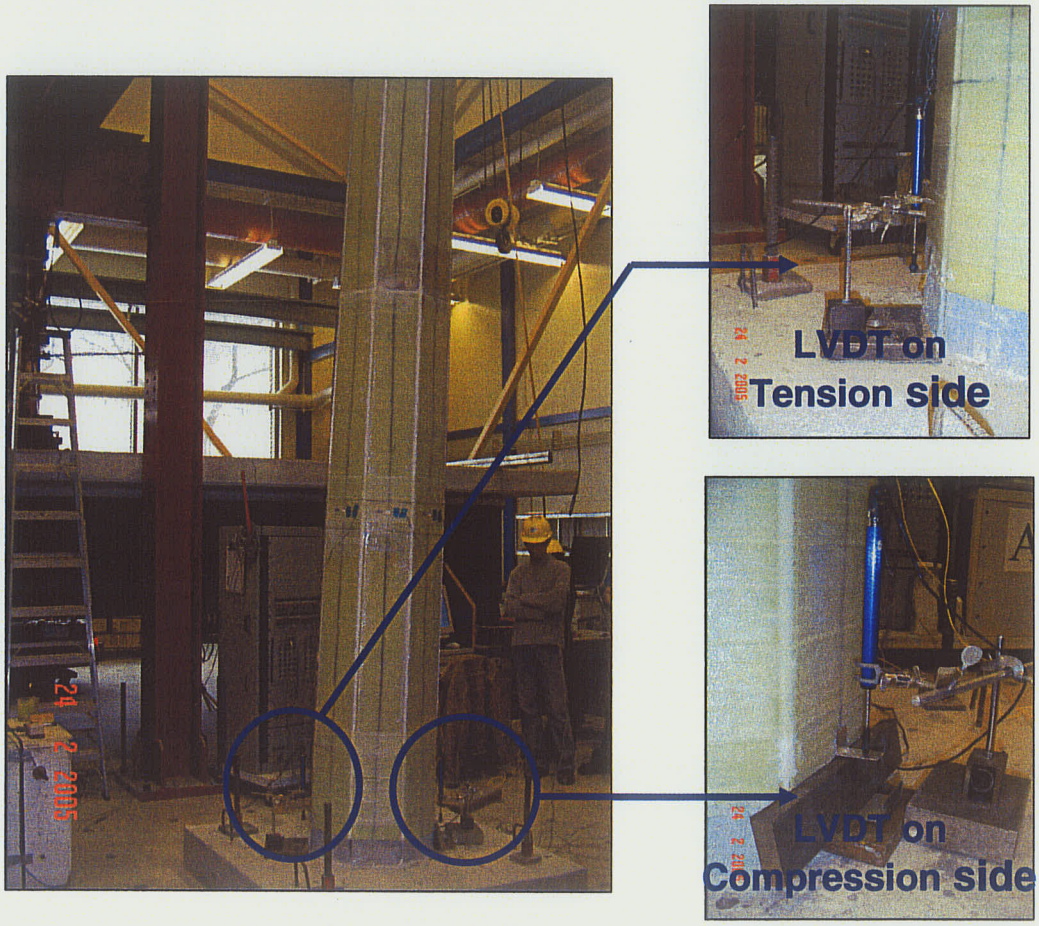

Figure 4-29 Measurement of vertical displacement of Phase III specimen

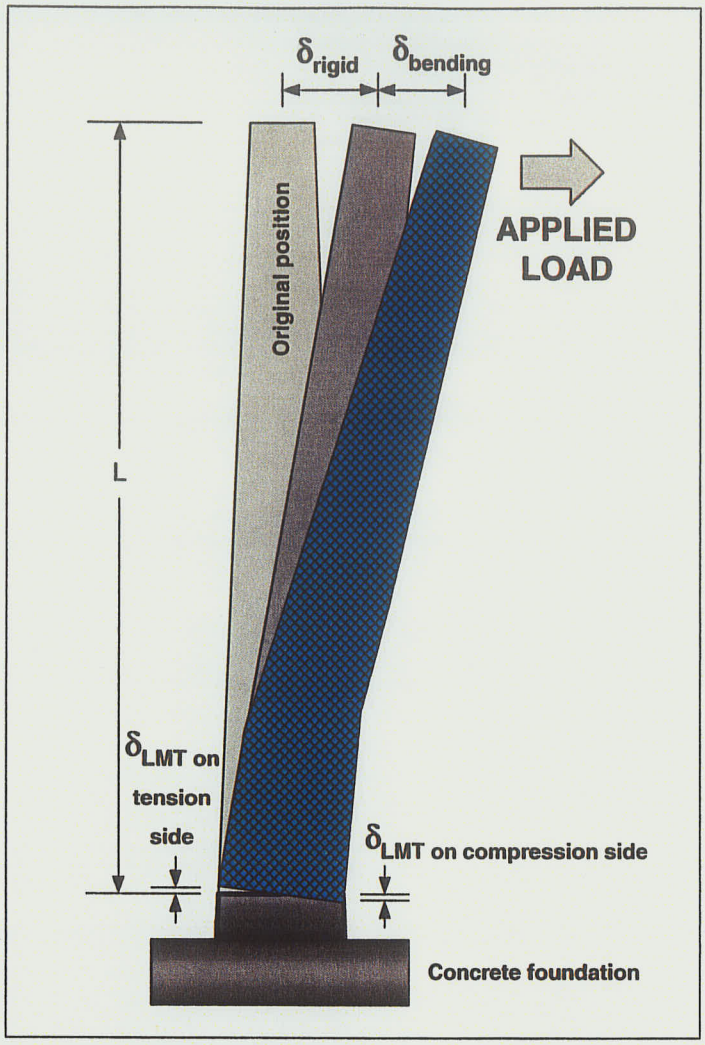

Figure 4-30 Schematic drawing of the actual horizontal displacement

(a) (b)

Figure 4-31 Phase III instrumentation

The load cell, the LMTs, LVDT, and strain gages were connected to a 64-channel Data Acquisition System to monitor and record all data onto a hard drive of a Pentium II PC using Labview software. The fiber optic sensors were connected to a FOXTEX 8-channel FT sensor scanner. The data from the FT scanner were then transferred and recorded onto a hard drive of a Pentium IV PC. Initial readings of all instruments were set to zero. The data were sampled every one second and plots of load versus deformations were on display during testing. Visual observations were also made during the test and the load was applied till a complete failure of the specimen occurred.

After specimen P3-1 was tested up to failure, a decision was made to repair and retest that specimen in order to study the effectiveness of the repair to restore the original structural performance of the tower. The surface of the section of the specimen P3-1 that experienced failure was sanded and prepared for the repair. The specimen was reinforced with a layer of 1258 g/m^2 unidirectional glass fiber matt providing a 0 degree fiber orientation and two layers of 340 g/m^2 bi-directional glass fiber tape to confine the reinforced region, as shown in **Figures 4-32 (a)** and **(b)**. Both matt and tape were saturated with West System epoxy resin (205/105) and then applied on the tower by hand. This specimen is referred to as P3-1R. The specimen P3-2 was not repaired after failure because of the extensive damage it suffered during testing.

(a) (b)

Figure 4-32 Repairing the tested specimen P3-1

4.5.4 Material Characterization

To determine the material properties of the FRP used in the theoretical model, 50 standard coupons (25 filament wound coupons and 25 unidirectional coupons) were fabricated and tested. The physical properties obtained from the coupons were the tensile modulus, the ultimate tensile strength, the compressive modulus, the ultimate compressive strength, the shear modulus, the ultimate shear strength, the density of the FRP, and the volume fraction of fiber and resin matrix. Five coupons were used for each test. In order to simulate the actual material properties of the FRP used to fabricate the towers, two types of coupons were fabricated namely filament wound coupons and unidirectional coupons.

4.5.4.1 Filament wound coupons

The coupons were fabricated using a filament winding machine specifically designed for the fabrication of such coupons. A square mandrel was used to produce flat coupons. Circumferential windings were employed to achieve unidirectional specimens. Glass fiber (TEX 1100) and West System 105/ 205 epoxy resin were used to manufacture the coupons. These materials were the same as those used in the manufacturing of the Phase I, II, and III specimens. The vacuum-bagging process was used after winding in order to drive out any air trapped in the material and to remove excess resin. After curing, square-shaped tubes were removed form the mandrel and cut into four panels, each panel measured 30 by 52 cm, as shown in **Figure 4-33**. Then, each panel was cut into four different configurations for various tests. Two configurations were used to create tensile coupons with longitudinal and transverse fiber orientations according to the ASTM standards D3039 (2000). One configuration was used to fabricate compressive coupons according to the ASTM standards D3410 (2000). The final configuration was used to fabricate shear coupons according to the ASTM standards D5379 (2000).

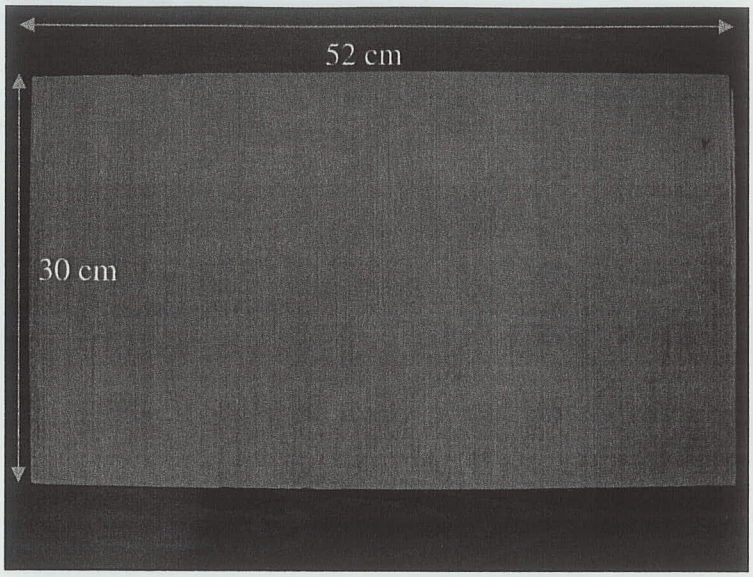

Figure 4-33 Filament wound coupon panel

The longitudinal fiber tensile coupons had an overall length of 250 mm, a width of 15 mm, and a thickness of 1 mm. The grip ends were reinforced with additional composite material to avoid local crashing of the coupons during testing. The longitudinal and transverse strains were measured using 5 mm strain gages located at mid section. The test set-up used to test the tensile coupons is shown in **Figure 4-34 (a)** and the longitudinal fiber tensile coupon configuration is shown in **Figure 4-34 (b)**. Unfortunately, due to large deformations the ultimate strain could not be recorded with the strain gauge, so only ultimate loads were recorded at the failure.

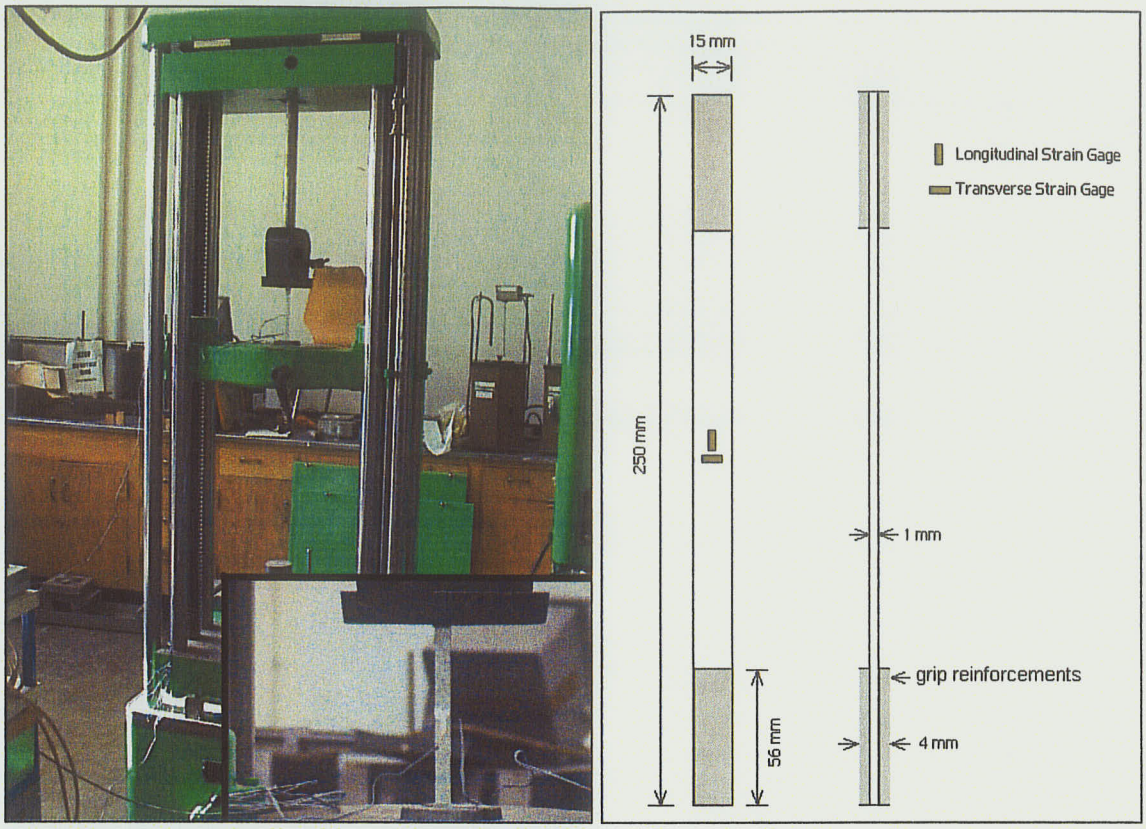

(a) (b)

Figure 4-34 Longitudinal tensile coupons

The transverse fiber tensile coupons had an overall length of 175 mm, a width of 25 mm, and a thickness of 1 mm. The ends of these specimens were also reinforced. The test set-up used is shown in **Figure 4-35 (a)** while the transverse fiber tensile coupon configuration is given in **Figure 4-35 (b)**. The longitudinal and transverse strains were measured and recorded in the same way as the longitudinal fiber tensile coupons.

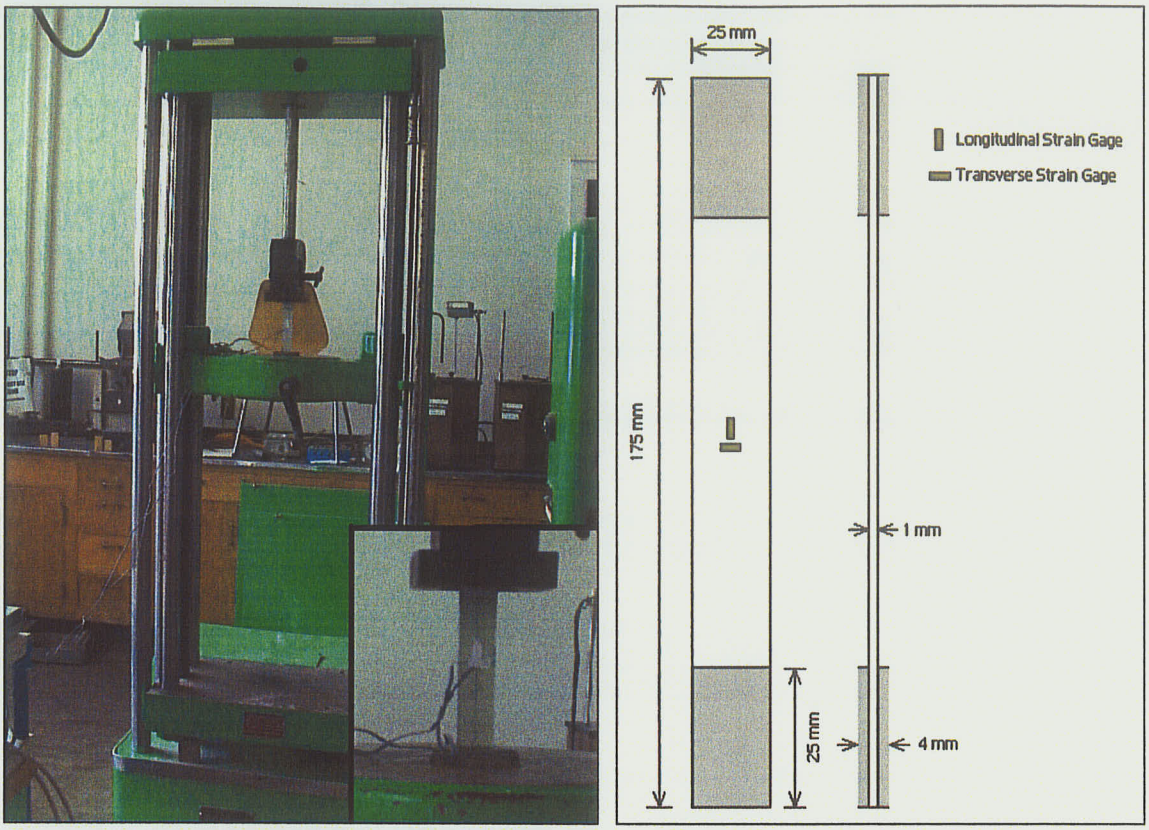

(a) (b)

Figure 4-35 Transverse tensile coupons

Compression coupons with longitudinal and transverse fiber reinforcements had a gage length of 10 mm, a width of 10 mm, and a thickness of 1 mm. The compression tests were conducted using a Modified Celenase Test Fixture, supplied by Wyoming Test Fixtures, as shown in **Figure 4-36 (a)**. The compression coupon configuration is shown in **Figure 4-36 (b)**. The longitudinal and transverse strains were measured with a 2 mm cross strain gage and recorded in the same way as the tensile coupons.

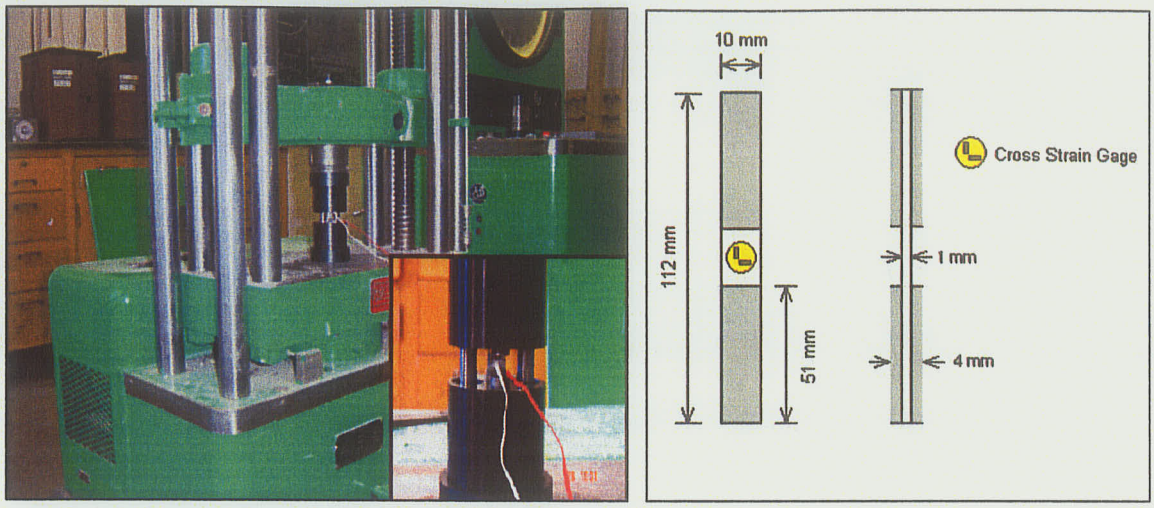

(a) (b)

Figure 4-36 Compression coupons

The shear coupons had a gage length of 12 mm, a width of 20 mm, and a thickness of 2 mm. The shear tests were performed in order to determine the in-plane shear properties of FRP, in accordance with ASTM Standard D5379 (2000). A cross strain gage was mounted at ±45° to the axial loading. The shear test set-up is shown in **Figure 4-37 (a)** and the shear coupons configuration is shown in **Figure 4-37 (b)**.

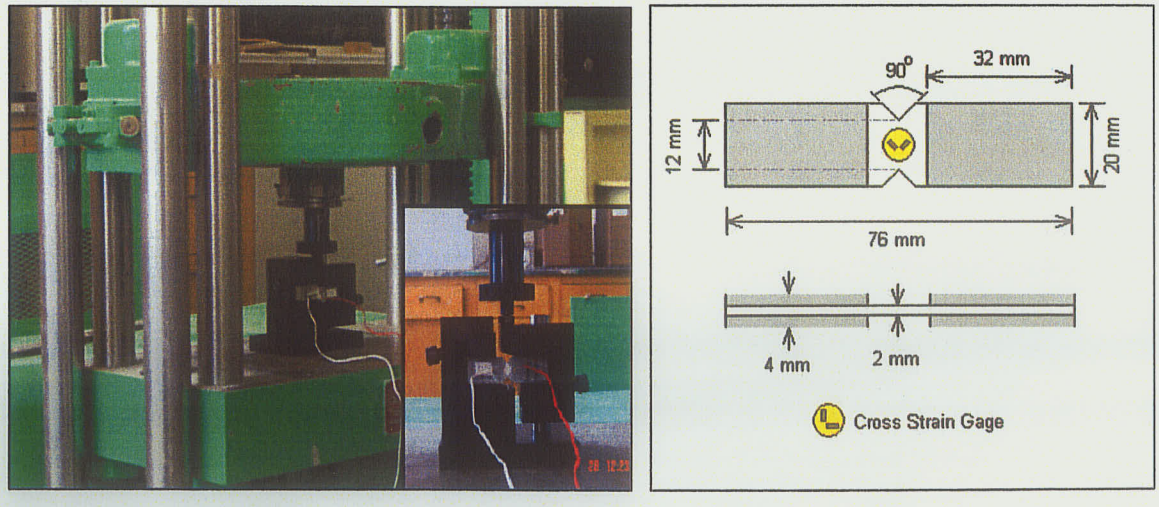

(a) (b)

Figure 4-37 Shear coupons

4.5.4.2 Unidirectional coupons

Unidirectional flat panels, as shown in **Figure 4-38 (a)**, were fabricated using 1258 g/m^2 unidirectional glass fiber matt and West System 105/ 205 epoxy resin. These materials were the same as those used in the manufacturing of the Phase I, II, and III specimens. A vacuum bagging process was employed in order to compact and remove excess resin, as shown in **Figure 4-38 (b)**. After curing, the panels were then cut into four different configurations, the same way as the filament wound coupons. The tensile, compression, and shear coupons were tested in accordance with the same ASTM Standard as those used in testing of the filament wound coupons. The coupon configurations used are the same as the filament wound coupons, except that the unidirectional coupons had a thickness of 1.75 mm. All coupons were tested to failure.

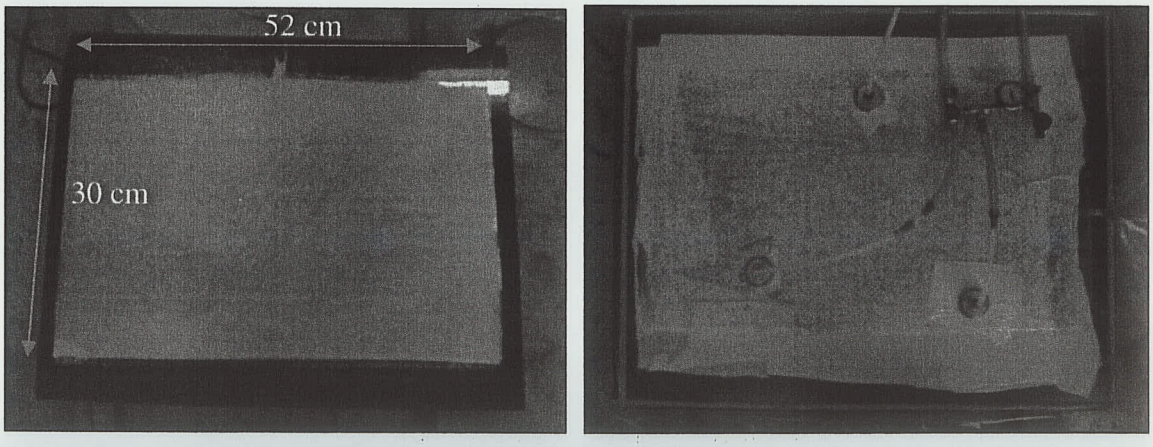

(a) FRP slab **(b)** Vacuum bagging process

Figure 4-38 Unidirectional coupon panel

4.5.5 Volume Fraction

The volume fraction of the matrix and fiber, as well as the density of the composite material used in this experimental program was determined. Samples were cut from the specimens tested. These had a fixed dimension of 25.4 by 101.6 mm, as shown in **Figure 4-39 (a)**. These samples were then put into the oven at the temperature of 500 degree Celsius to burn out all the resin. The samples after burning are shown in **Figure 4-39 (b)**. The samples were weighed before and after burning. The difference in weight before and after burning gives the mass of the resin in the FRP coupon. Using the manufacturer's specific gravity of the epoxy of 1.18 g/m^3, the volume of the resin was calculated. Using this value, the volume fraction of the matrix and glass fiber were then determined.

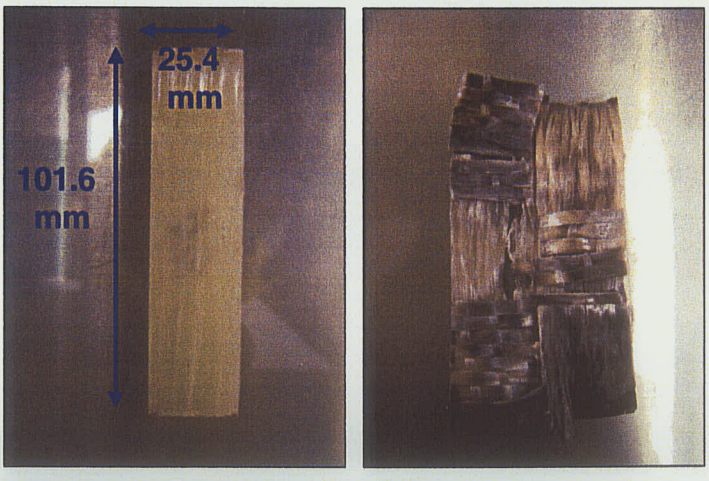

(a) Before burning **(b)** After burning

Figure 4-39 Coupon used to determine volume fraction

CHAPTER 5

EXPERIMENTAL RESULTS AND DISCUSSION

5.1 GENERAL

The experimental results from the three test phases are presented and discussed in this chapter. The data is presented in the form of load versus deflection, load versus strain, tables and figures. The experimental results from each phase are presented separately.

5.2 PHASE I

Two single GFRP cell specimens, namely P1-1 and P1-2, were tested as cantilevers. The load was applied monotonically at the free end until failure to obtain the following data:

a) the load-deflection characteristics;

b) the strain distribution; and,

c) the failure mechanism.

5.2.1 Load-Deflection Characteristics

The load-deflection curves for P1-1 and P1-2 specimens at different locations are shown in **Figures 5-1** and **5-2**, respectively. The load-displacement curve for the sleeve (LVDT1) indicates that a deformation of the sleeve occurred during testing. This resulted in an increase in the tip deflection of the tested specimens. Hence, the tip deflection of the tested specimens needs to be adjusted to take into account the deflection of the composite sleeve. Specimen P1-2 had to be unloaded and reloaded again due to a technical problem during testing. However, the structural behavior of specimen P1-2 was consistent with that of specimen P1-1. The load-deflection relationship was linear until a sudden drop in the load after local buckling occurred.

The load-deflection curves for both specimens at the free end are illustrated in **Figure 5-3**. The ultimate load carrying capacity and the corresponding deflection for both specimens are summarized in **Table 5-1**. The average ultimate load carrying capacity, tip deflection, and stiffness of both specimens were 3.72 kN 156.81 mm, and 24.25 kN/m, respectively. The test results showed a small variation in ultimate load, tip deflection, and stiffness as illustrated in **Table 5-1**. This is because both specimens had the same fiber orientations.

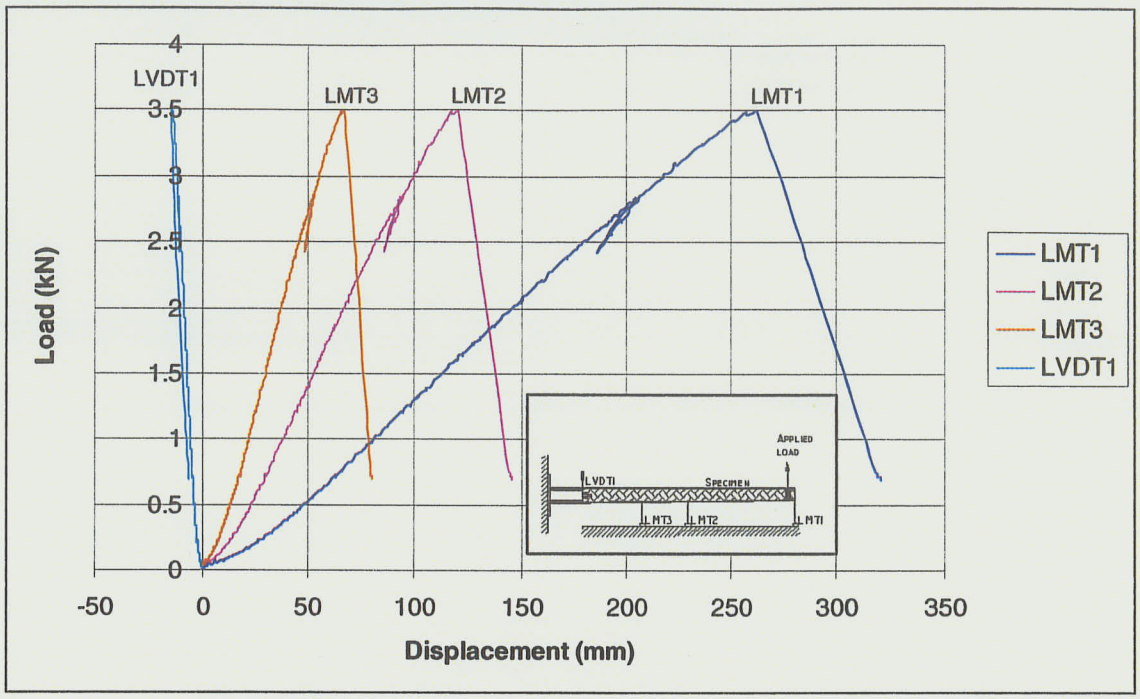

Figure 5-1 Load-deflection curve for P1-1 specimen

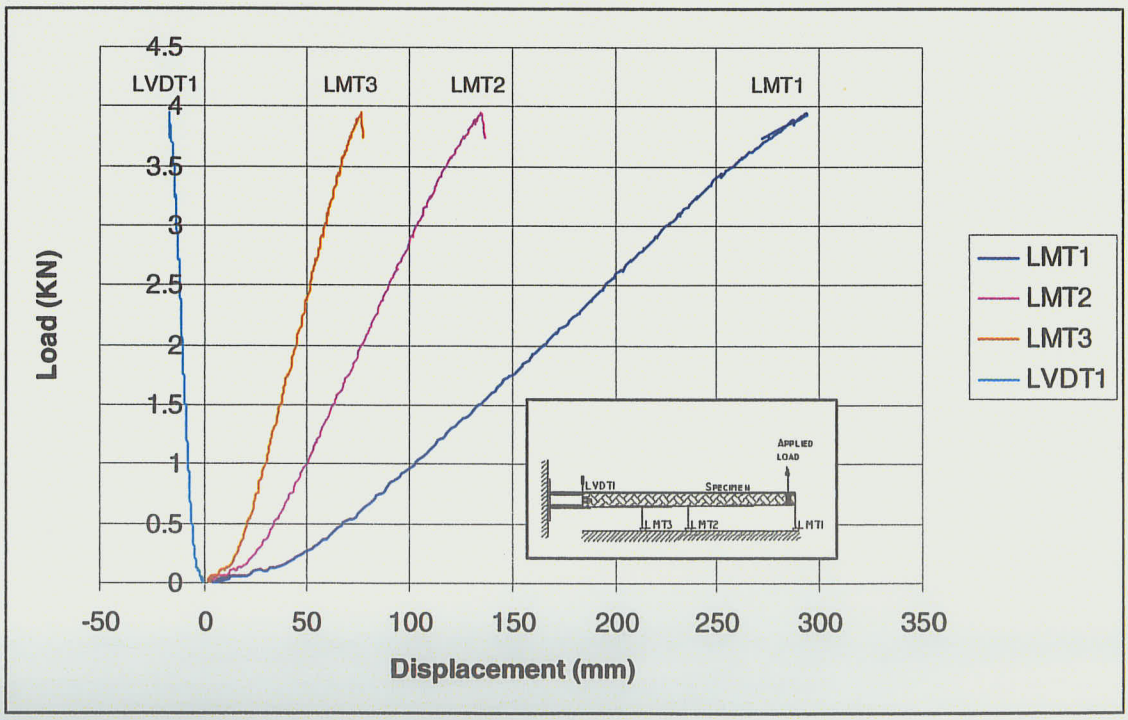

Figure 5-2 Load-deflection curve for P1-2 specimen

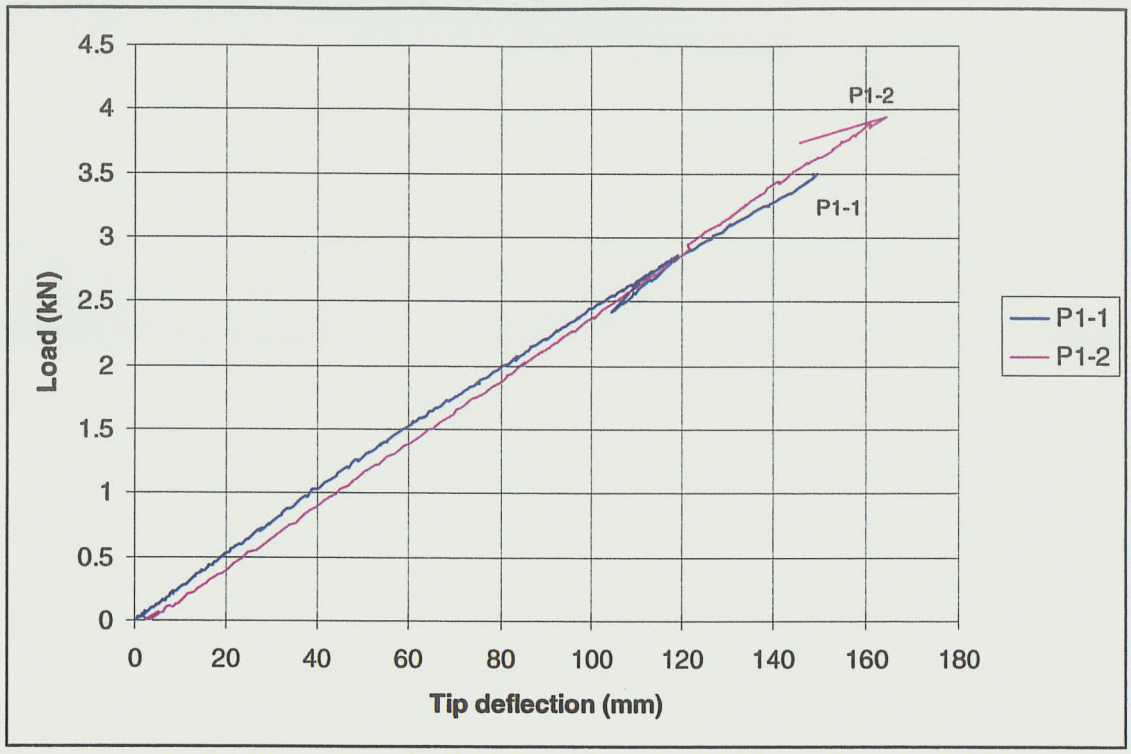

Figure 5-3 Load-deflection curves for both specimens in Phase I

Table 5-1 Phase I results summary

Specimen	Ultimate load (kN)	Tip deflection (mm)	Stiffness (kN/m)	Mass (kg)
P1-1	3.50	149.09	24.90	8.11
P1-2	3.94	164.52	23.60	8.86
Average	3.72	156.81	24.25	8.48

5.2.2 Strain Distribution

The load-strain relationships of Phase I specimens tested are discussed in this section. In both P1-1 and P1-2 specimens, which failed due to local buckling on the compression side, strains were monitored at twelve locations as described in the previous chapter.

Typical load-strain diagrams at the center of the flanges and at the corners for specimen P1-1 are shown in **Figures 5-4** and **5-5**, respectively. In specimen P1-1, which failed by local buckling, strain were monitored at 315, 467, and 619 mm away from the support on both the tension and the compression sides. As shown in **Figures 5-4** and **5-5**, the relationship between load and both tensile and compressive strains was linear. The strains measured at the corners (CT, and CB) were higher than those measured at the center of the flanges (T, and B). Also, the closer the strain gages to the support, the higher the strains measured. The maximum compressive strain at failure was approximately 6000 με (0.6%). A similar behavior was observed on the tension side of the specimen. The maximum tensile strain was approximately 5000 με (0.5%). Unfortunately, the ultimate strains were not recorded in these specimens since local buckling did not occur where the strain gages were attached. A similar behavior was observed on specimen P1-2.

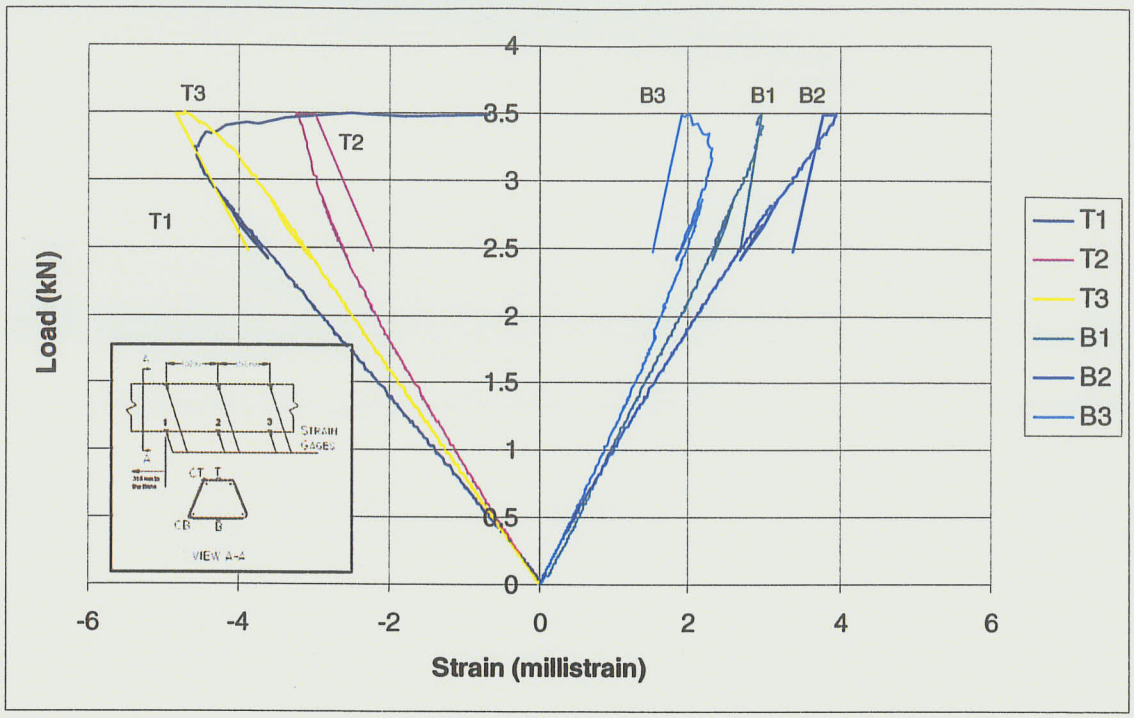

Figure 5-4 Load-strain curve at the center of the flanges for specimen P1-1

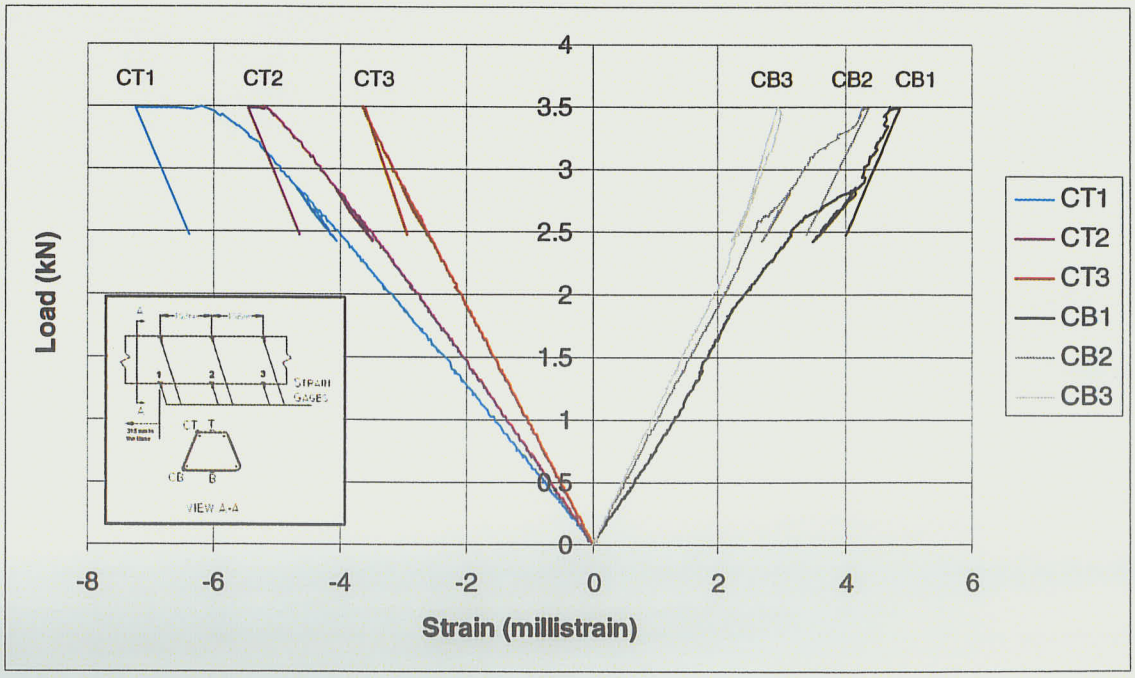

Figure 5-5 Load- strain curve at the corners for specimen P1-1

5.2.3 Failure Mode

The failure mode in both specimens in Phase I was local buckling on the compression side near the fixed support. There was no other sign of failure, such as cracking or crushing of the resin or fibers during testing. **Figure 5-6** shows the typical failure mode of Phase I specimens. The location of the buckling for specimen P1-1 and P1-2 was 385 mm and 504 mm from the support, respectively.

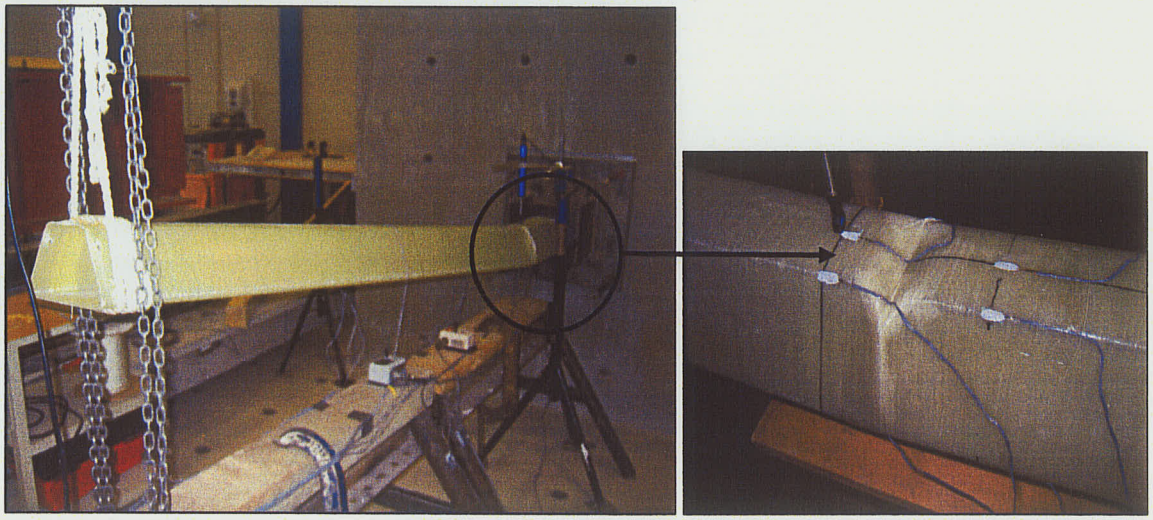

Figure 5-6 Local buckling failure mode for specimen P1-1

5.3 PHASE II

Two single GFRP cell specimens, P2-1280-1 and P2-1780-2, were tested under compression.

The load versus vertical deformation diagram for Phase II specimens is given in **Figure 5-7**. Since the specimens had different in heights, the ultimate compressive loads obtained were different. Specimen P2-1280-1, with a height of 1280 mm, had an ultimate compressive load of 82.89 kN, while specimen P2-1780-2, with a height of 1780 mm, had an ultimate compressive load of 64.38 kN. The P2-1280-1 had a higher load carrying capacity, which was expected, because of the width-to-cell wall thickness ratio in specimen P2-1280-1 was lower than those in P2-1780-2. **Figure 5-7** shows a sudden drop in load for both specimens after local buckling occurred.

"Ripples" were observed along the height on both specimens prior to failure by local buckling, as illustrated in **Figures 5.8** and **5-9**.

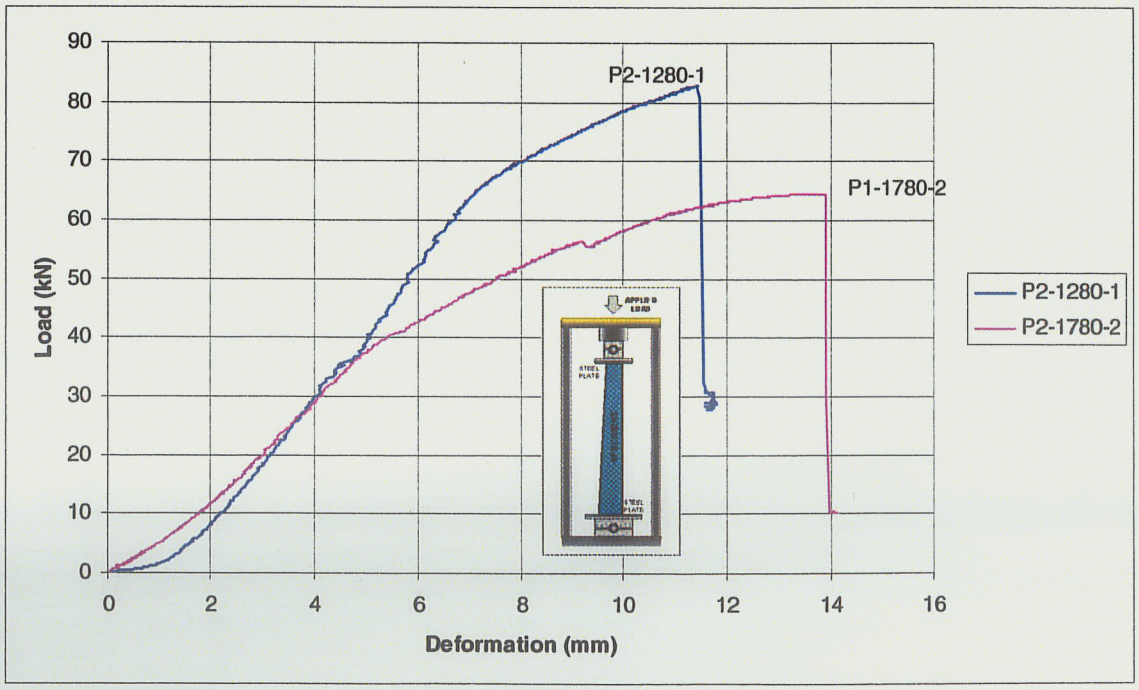

Figure 5-7 Load-deformation curve for Phase II specimens

Figure 5-8 Typical ripples occurred on Phase II specimens

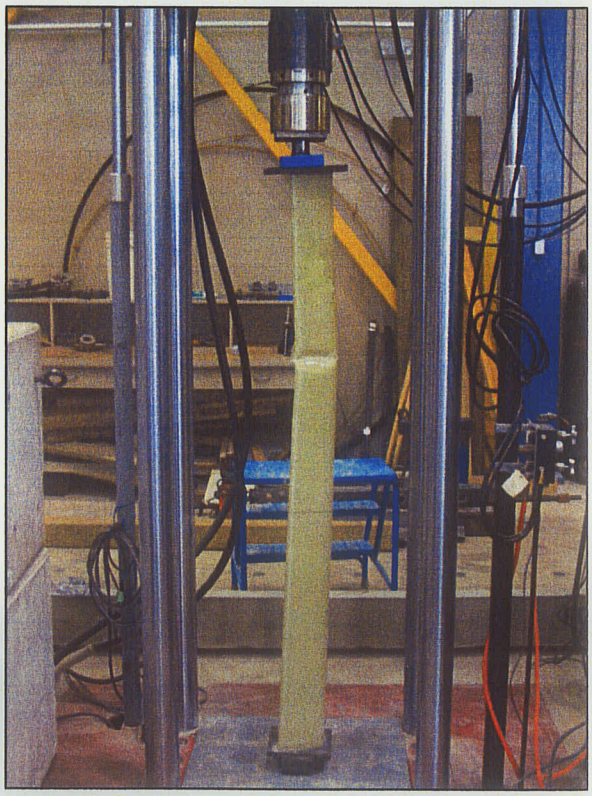

Figure 5-9 Local buckling of specimen P2-1780-2

5.4 PHASE III

Three eight-cell jointed GFRP tower specimens, P3-1, P3-1R, and P3-2, were tested under cantilever bending until failure to obtain the following data:

a) the load-deflection characteristics;

b) the strain distribution; and,

c) the failure mechanism.

5.4.1 Load-Deflection Characteristics

The load-deflection curves for P3-1, P3-1R, and P3-2 specimens at different locations are shown in **Figures 5-10**, **5-11**, and **5-12**, respectively. It should be noted that after specimen P3-1 was tested to failure, it was repaired and tested again. This specimen is listed as P3-1R. **Figure 5-13** shows the slip displacement of the specimens that occurred at the concrete foundation as recorded by two LVDTs placed on the tension and compression sides of the specimen. This slip caused an increase in the tip deflection of the specimens tested. Hence, the tip deflection of the tested specimens includes both the deflection due to bending and the rigid body movement of the tower due to slip at the foundation as previously discussed in Section 4.5.3.3. The load-tip deflection curve of Phase III specimen after taking into account the shifting effect is illustrated in **Figure 5-14**. The actual ultimate tip deflection of the Phase III specimens was not recorded since the LVDTs were removed before failure of the

specimen in order to prevent damage to the LVDTs. The towers, however, had reached their ultimate capacity and were undergoing considerable deformation which the instrumentation was removed.

The load-deflection relationship of the towers was linear up to the point when the first indication of local buckling. However, the towers were able to sustain additional load until total failure of the specimens occurred. The towers exhibited post buckling strength, unlike those of Phase I specimens, where the single cells exhibited a sudden drop in the load right after the local buckling occurred. This ability of the individual cells to redistribute the load to other cells after local buckling is significant and demonstrates that the cells in the towers work as a group rather than as individual units.

The structural behavior of specimen P3-2 was consistent with that of specimen P3-1. The stiffness of specimens P3-1 and P3-2 were 293.41 kN/m and 283.22 kN/m, respectively and the average stiffness was 291.32-kN/m. A load-tip deflection diagram of specimen P3-1R, as shown in **Figure 5-14**, exhibits two distinct stages of structural behavior. In the first stage before specimen P3-1R reached the load of 2.85 kN, the average stiffness is 289.31 kN/m, which is similar to those of P3-1 and P3-2. In the second stage, after the load reached 2.85-kN, the specimen P3-1R started to have a wrinkle on the compression side and at the same location where the specimen P3-1 failed. This caused a drastic decrease in the stiffness of specimen P3-1R to around 156 kN/m and an

increase in the tip deflection. Thus, the repair technique was not as effective as assumed and more work in this area is required in the future.

The ultimate load carrying capacity and the corresponding deflections for the two towers, P3-1 and P3-2, are summarized in **Table 5-2**. The average ultimate load carrying capacity, tip deflection of specimens P3-1 and P3-2 were 19.11 kN and 76.90 mm, respectively. The test results showed a small variation in the ultimate load and tip deflection as illustrated in **Table 5-2**. This is because both specimens had the same fiber orientations. The ultimate load carrying capacity of specimen P3-1R was 20.97 kN, which was similar to those of P3-1 and P3-2. However, the tip deflection of P3-1R was almost twice of that of P3-1 and P3-2. This is attributed to the loss of stiffness after compressive failure of P3-1 in the previous test.

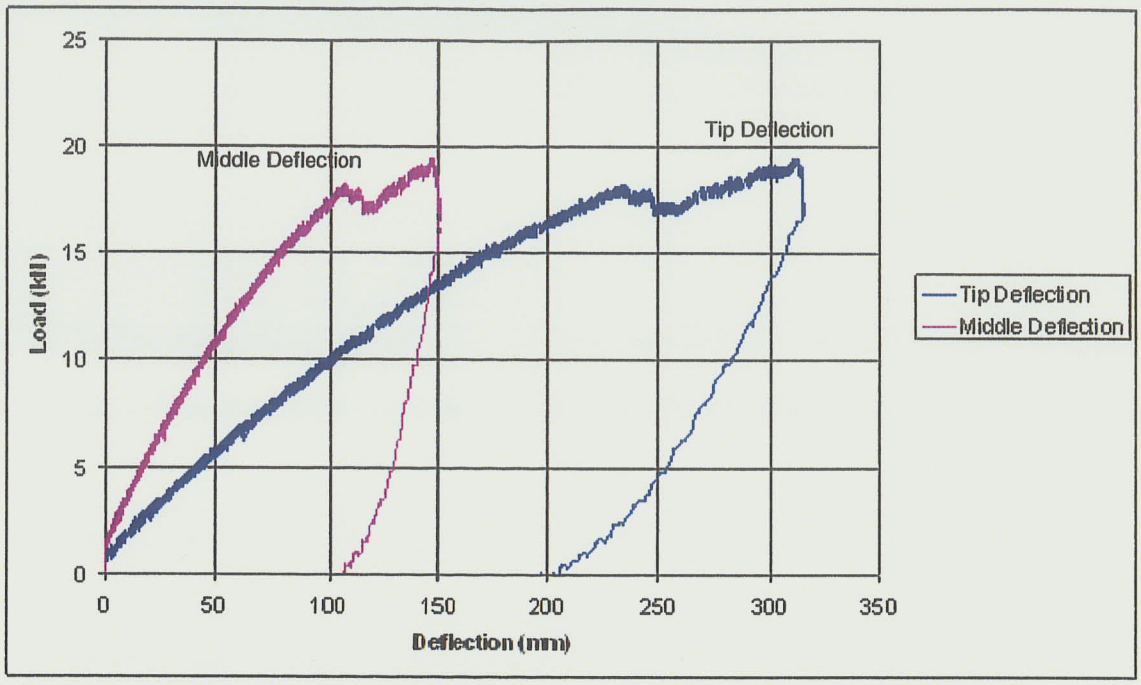

Figure 5-10 Load-deflection curve for P3-1 specimen

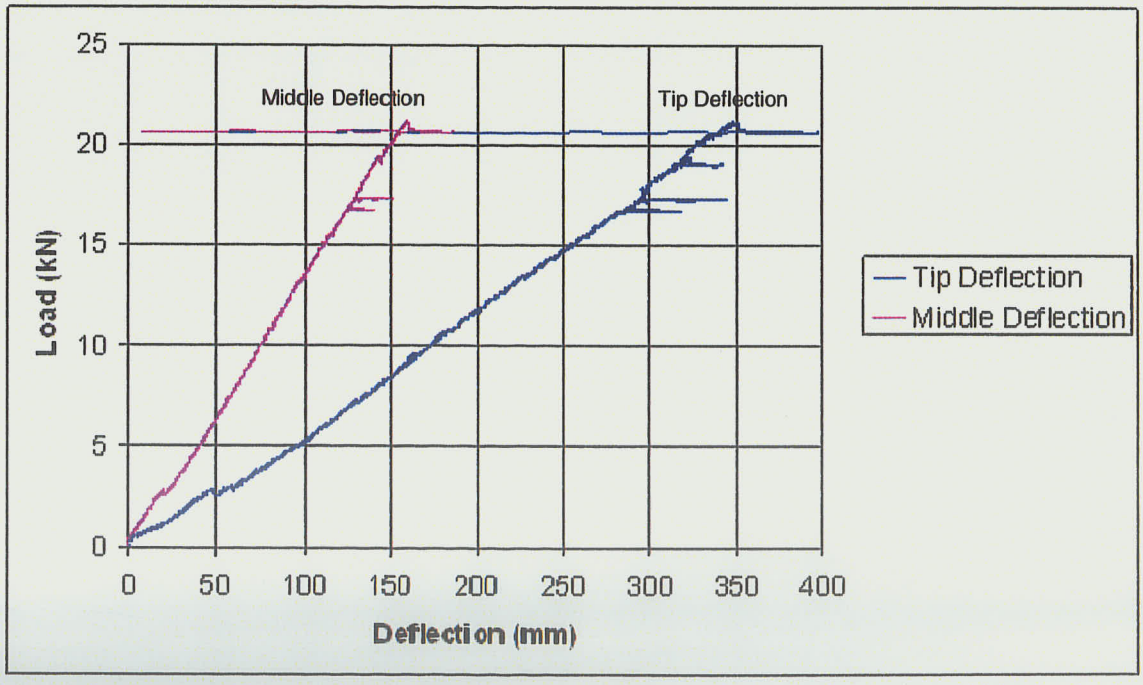

Figure 5-11 Load-deflection curve for P3-1R specimen

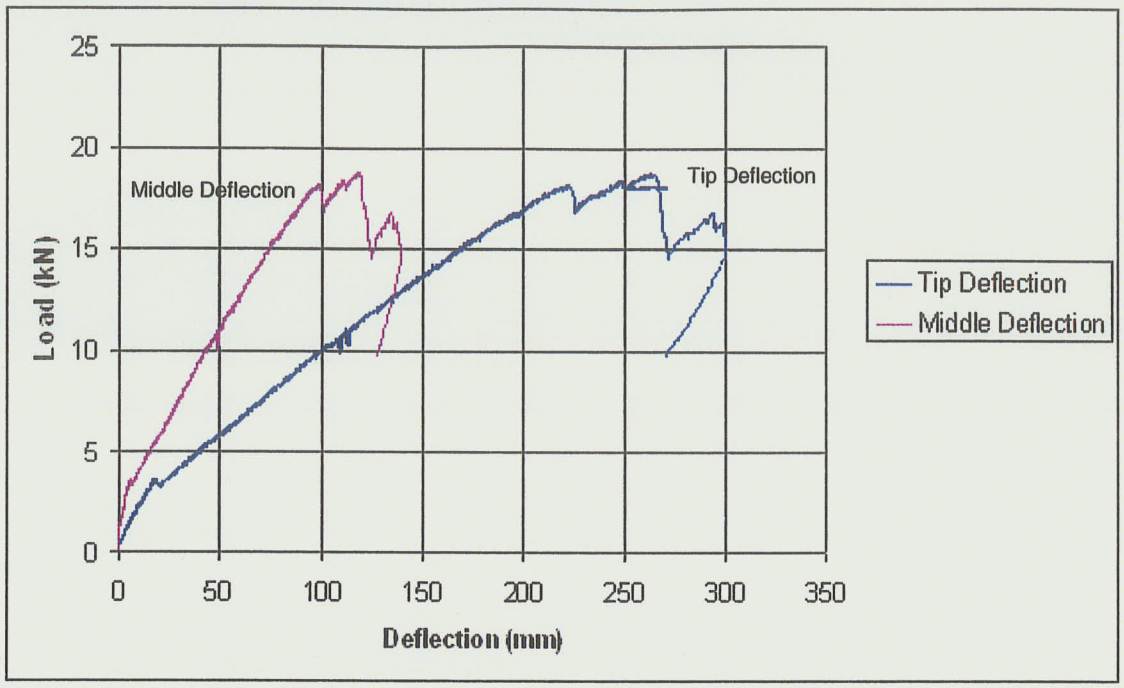

Figure 5-12 Load-deflection curve for P3-2 specimen

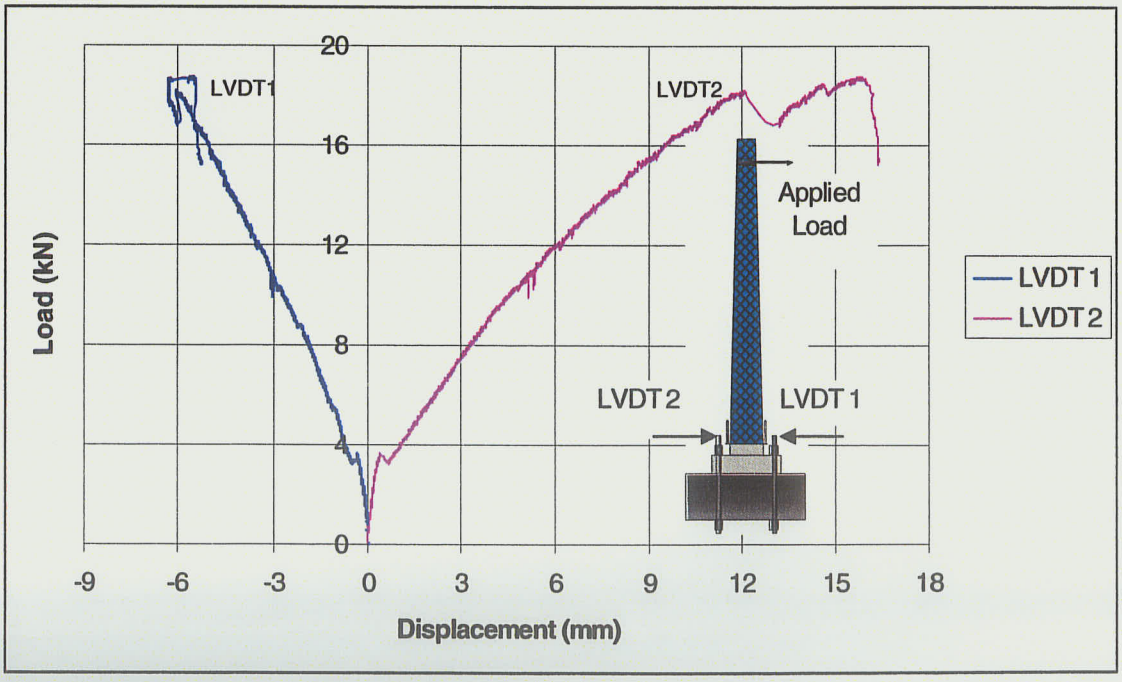

Figure 5-13 Load-displacement curve at the base of P3-2 specimen

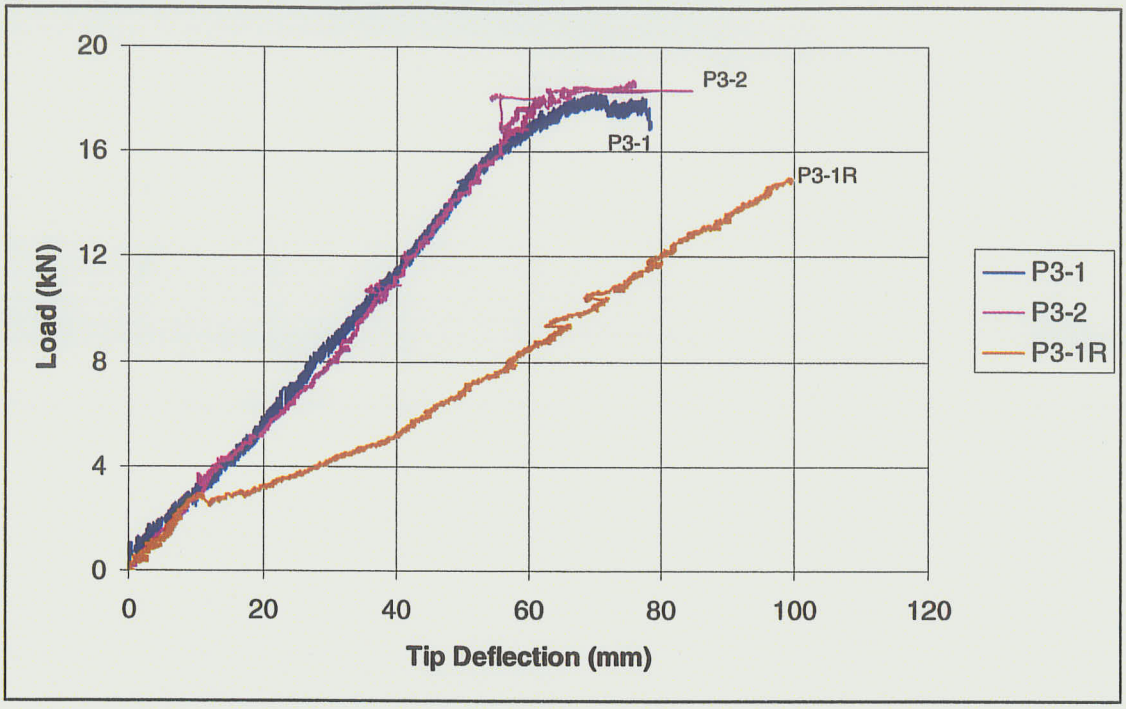

Figure 5-14 Load-tip deflection curves for tower specimens

Table 5-2 Phase III results

Specimen	Ultimate load (kN)	Tip deflection (mm)	Stiffness (kN/m)
P3-1	19.48	78.21	293.41
P3-2	18.74	75.59	289.22
Average	19.11	76.90	291.32
P3-1R	20.97	121.21	289.31*/156.26**

* First segment of P3-1R load-deflection diagram
** Second segment of P3-1R load-deflection diagram

5.4.2 Strain Distribution

The load-strain relationships of Phase III specimens tested are discussed in this section. In P3-1, P3-1R, and P3-2 specimens, strains were monitored at twenty-four locations as described in the previous chapter.

Typical load versus longitudinal compressive strain diagrams for specimen P3-1, P3-1R, and P3-2 are shown in **Figures 5-15**, **5-16**, and **5-17**, respectively. The strain gages used on the compression side, namely C1, C2, C3, C4, C5, C6, and C7, were located at heights of 585, 685, 785, 885, 985, 1085, and 1185 mm, respectively, from the base. In the beginning, the relationship between load and strain was linear. When the load reached approximately 8 kN, "ripples", as shown in **Figure 5-18**, were observed on the compression side of the specimens. The ripples caused a reversal in the strains, as shown in **Figures 5-15**, **5-16**, and **5-17**. The relationship between load and strain became nonlinear after the ripples appeared.

Figures 5-19, **5-20**, and **5-21** show typical load versus longitudinal compressive strain in the vicinity of the connection between the lower and upper segments of specimen P3-1, P3-1R, and P3-2, respectively. The strain gages JC1, JC2, JC3, JC4, and JC5 were located at heights of 2400, 2450, 2565, 2680, and 2730 mm, respectively from the base, as described in the previous chapter. The relationship between load and longitudinal compressive stains at JC2, JC3, and

JC4 where the shell thickness was double was fairly linear. There was no local buckling in this area. The strains in JC1 and JC5 were affected by local buckling on the compression side of the specimen. Therefore, the relationship between load and stain in JC1 and JC5 was nonlinear. Unfortunately, the ultimate strains were not recorded since the local buckling did not occur where the strain gages were attached.

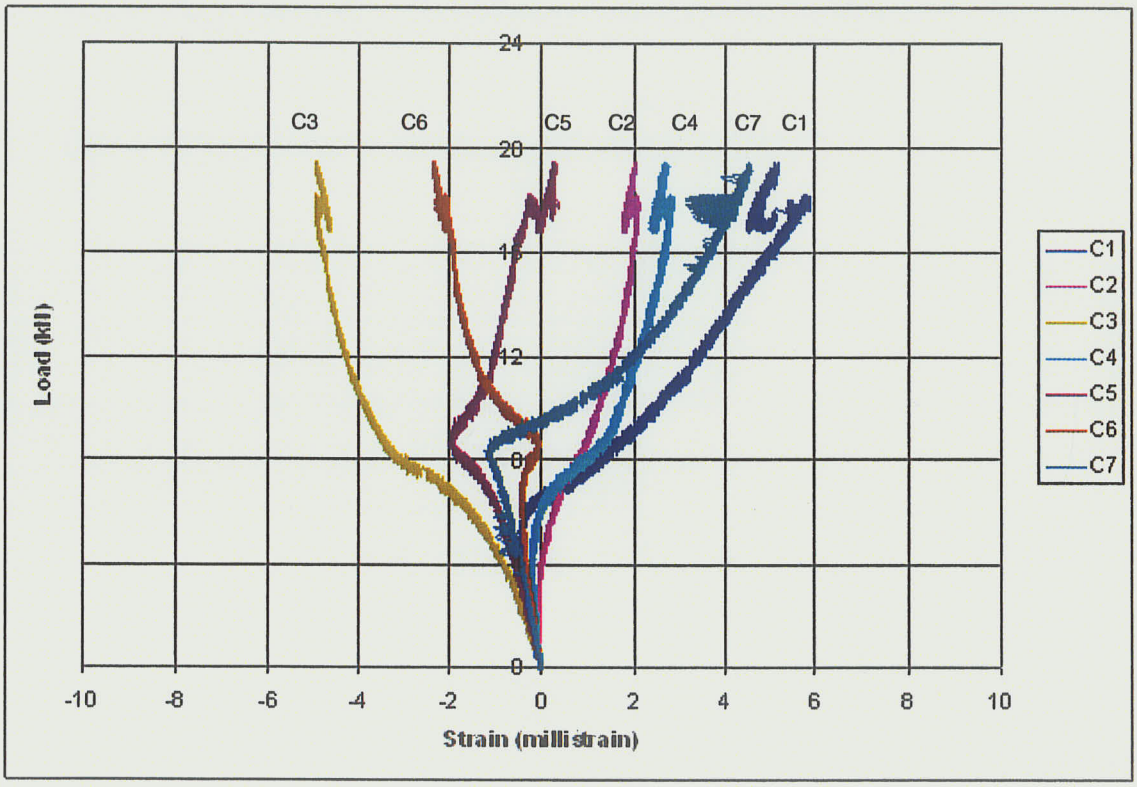

Figure 5-15 Load-longitudinal compressive strain curve for P3-1 specimen

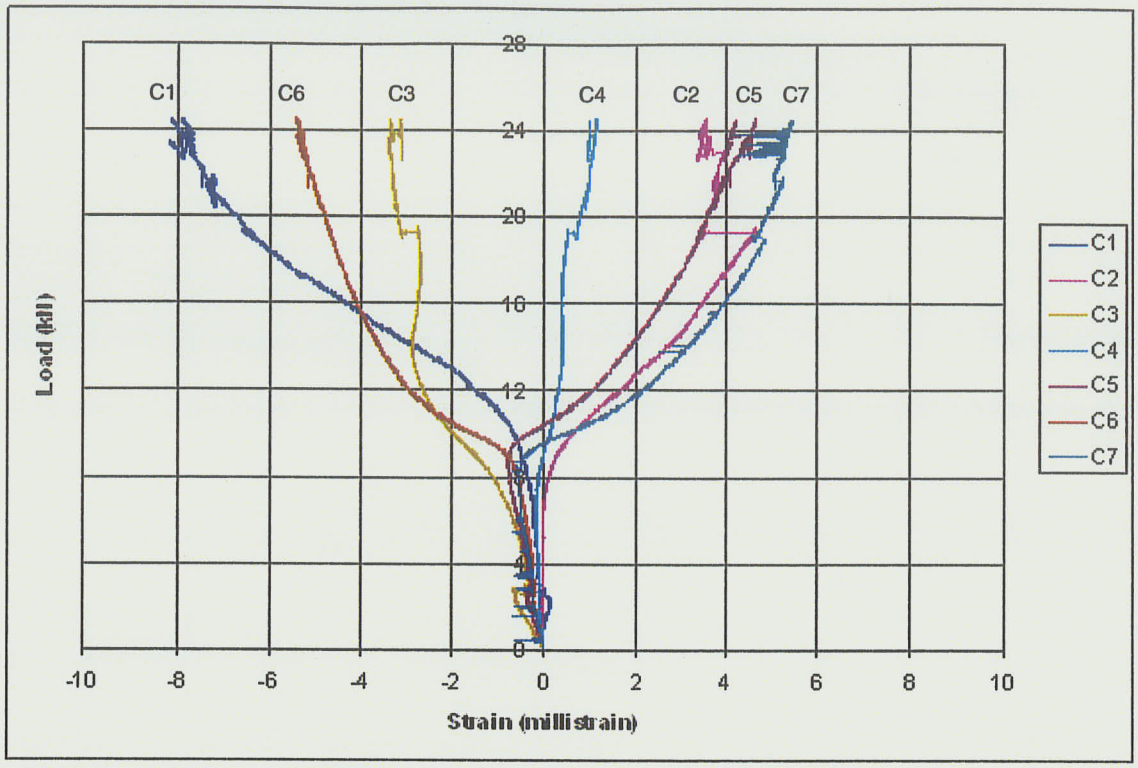

Figure 5-16 Load-longitudinal compressive strain curve for P3-1R specimen

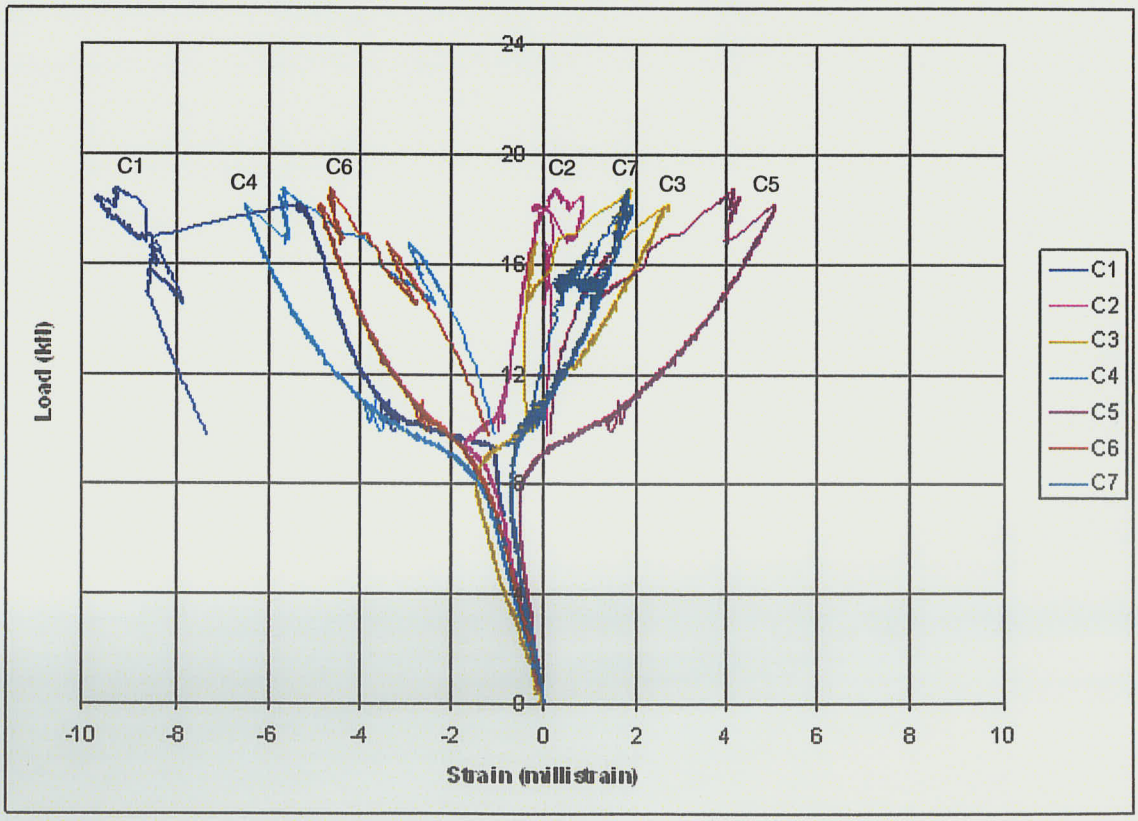

Figure 5-17 Load-longitudinal compressive strain curve for P3-2 specimen

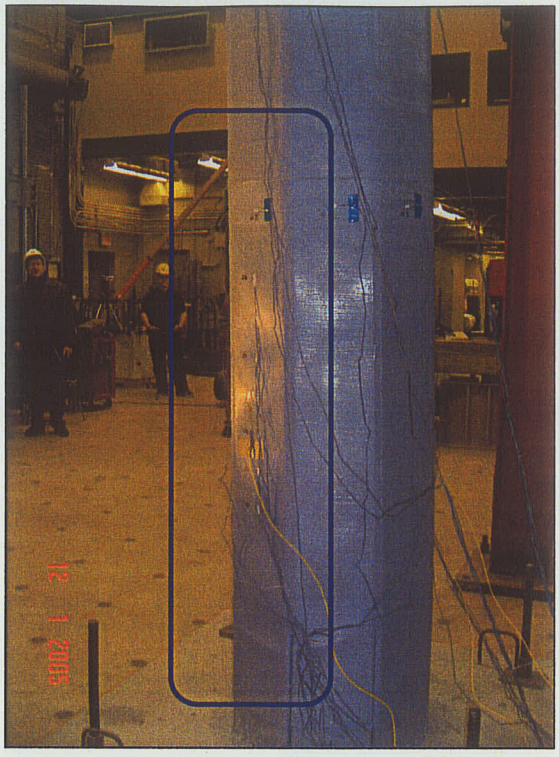

Figure 5-18 Typical ripples occurred on Phase III specimens

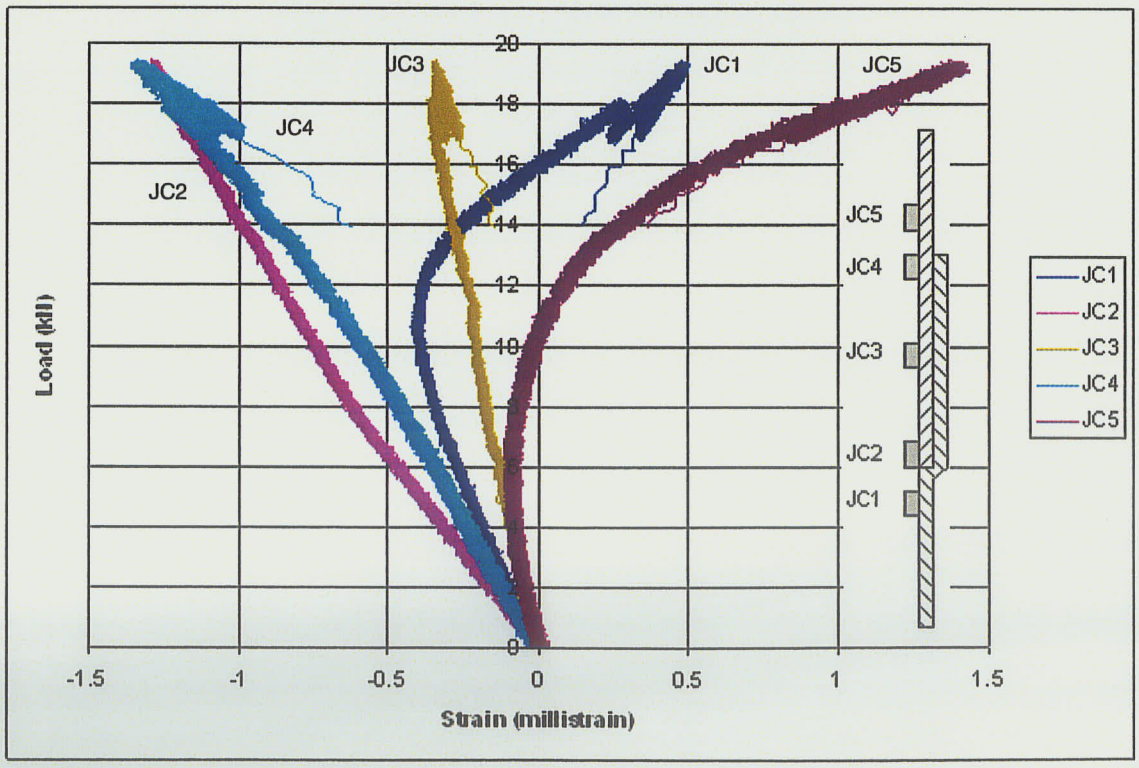

Figure 5-19 Load-longitudinal compressive strain curve at the joint for P3-1 specimen

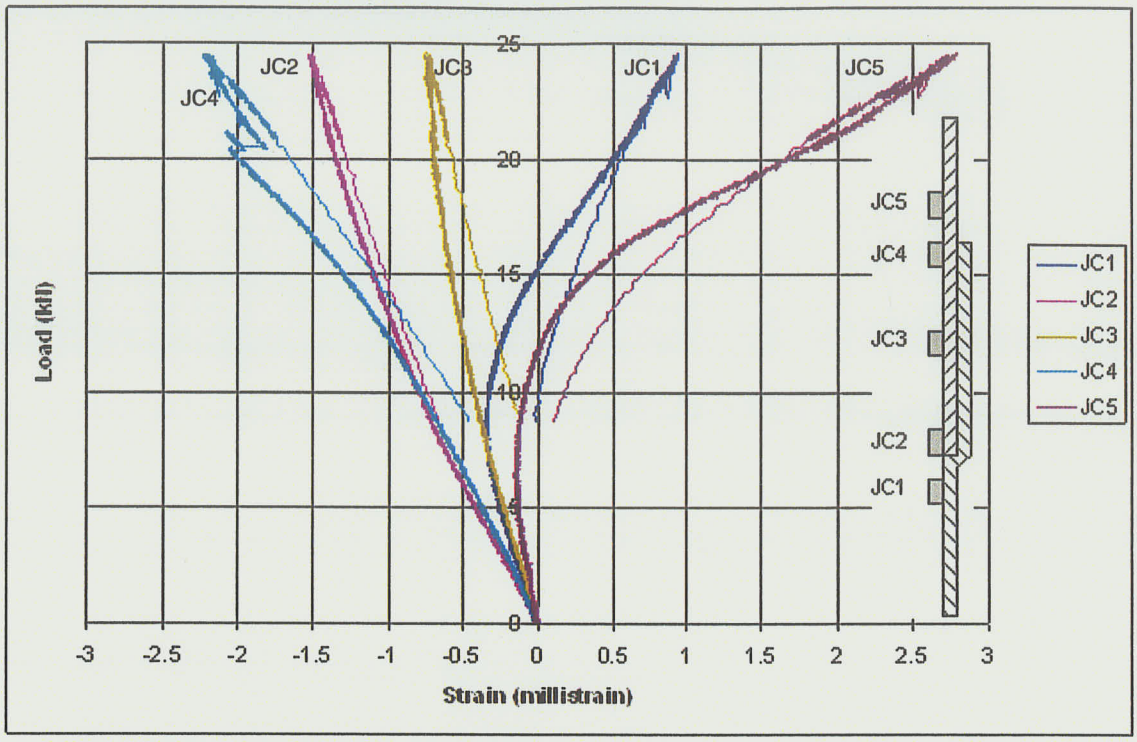

Figure 5-20 Load-longitudinal compressive strain curve at the joint for P3-1R specimen

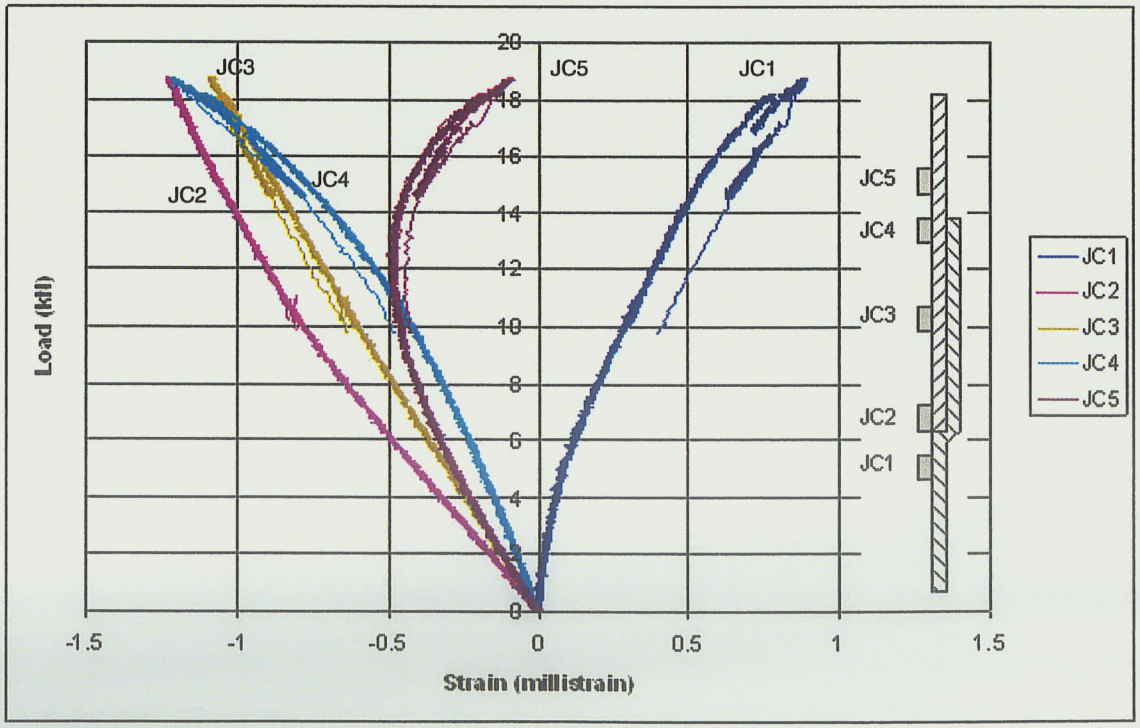

Figure 5-21 Load-longitudinal compressive strain curve at the joint for P3-2 specimen

Load versus longitudinal tensile strain diagrams for specimen P3-1 is shown in **Figures 5-22**. The strain gages used on the tension side, T1, T2, T3, T4, T5, T6, T7, were located at heights of 585, 685, 785, 885, 985, 1085, and 1185 mm, respectively from the base. **Figure 5-23** shows typical load versus longitudinal tensile strain in the vicinity of the connection between the lower and upper segments of specimen P3-1. The strain gages JC1, JC2, JC3, JC4, and JC5 were located at heights of 2400, 2450, 2565, 2680, and 2730 mm, respectively from the base, as described in the previous chapter. The relationship between load and strain was linear in all the locations.

According to Figures 5-22 and 5-23, the strains obtained from group T strain gages were approximately three times those from group JT strain gages. The ultimate strains at the joint and at the base region were around 1000 με (1%) and 3000 με (3%), respectively. This is attributed to the fact that the shell thickness in the JT region was twice that in the T region and also the applied bending stresses were higher in the T region. A similar behavior was founded on specimen P3-2.

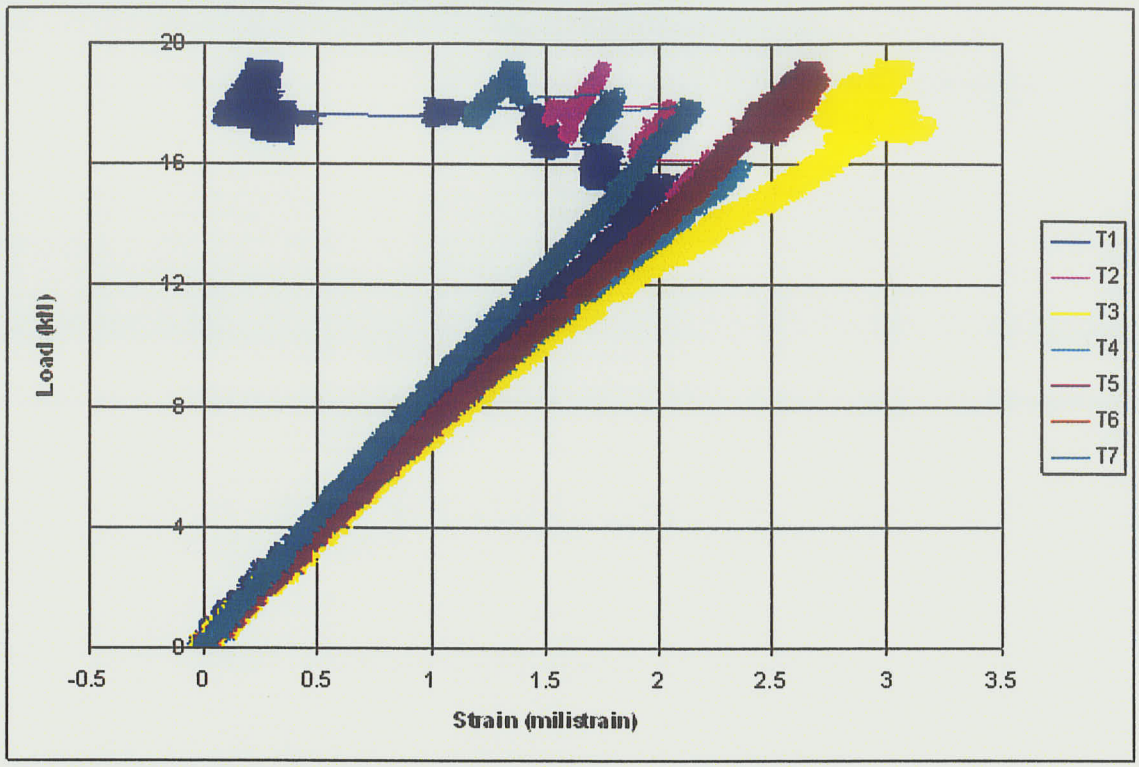

Figure 5-22 Load-longitudinal tensile strain curve for P3-1 specimen

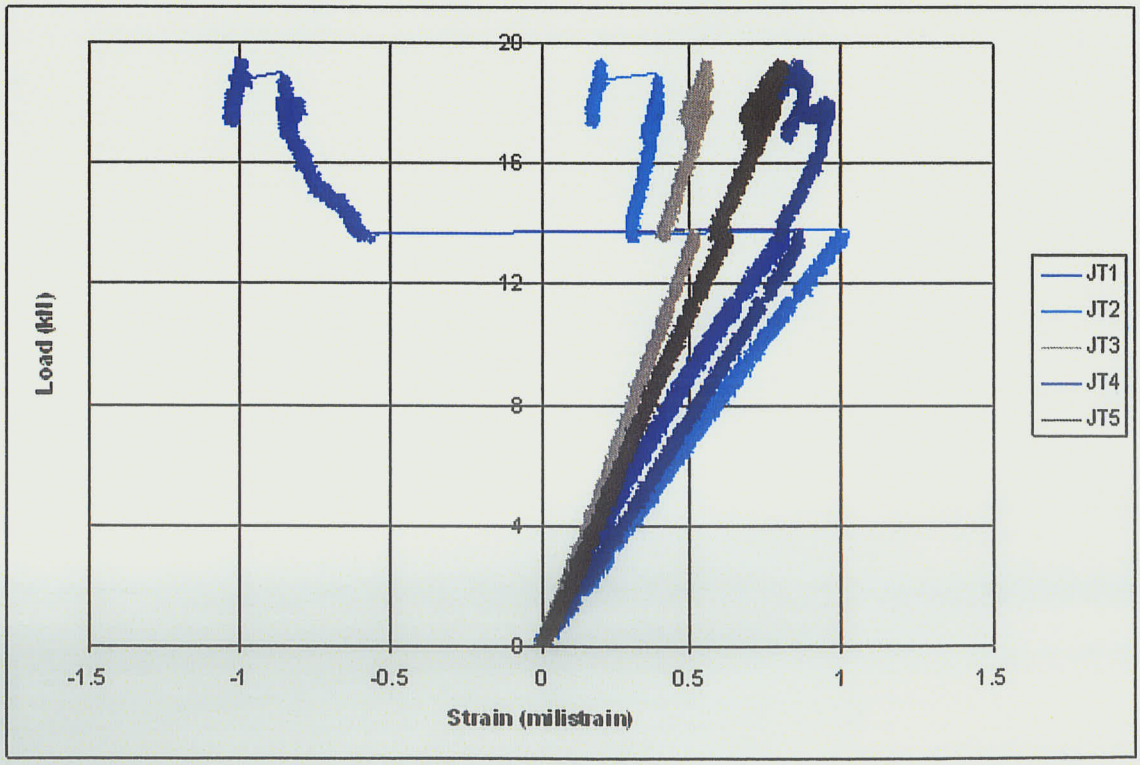

Figure 5-23 Load-longitudinal tensile strain curve at the joint for P3-1 specimen

5.4.3 Failure Modes

While the two towers (P3-1 and P3-2) reached approximately the same ultimate load, their mode of failure was different from each other. Specimens P3-1 failed due to material failure at a section of maximum compressive stress and was characterized by shear rupture of the fibers on the compression side of the specimen within the foundation as illustrated in **Figure 5-24 (a)**. Specimen P3-1R, repaired specimen P3-1, started to rapture at the same location where specimen P3-1 failed at a very low load and then the unidirectional matt used in the repair was delaminated from the specimen and fractured, as shown in **Figure 5-24 (b)**. After removal of the specimen P3-1R, it was observed that the concrete inserts on the tension side had suffered extensive damage which was subsequently repaired for the testing of tower specimen P3-2. Specimen P3-2 failed by local buckling at a height of 515 mm above the base, as shown in **Figure 5-25.**

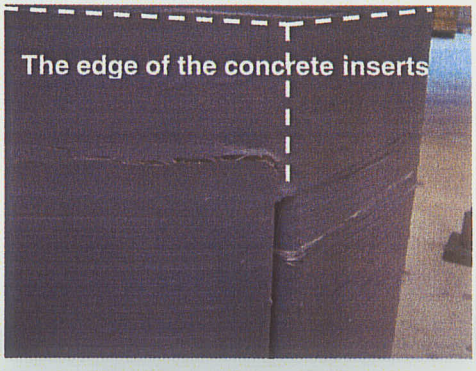

(a) Specimen P3-1

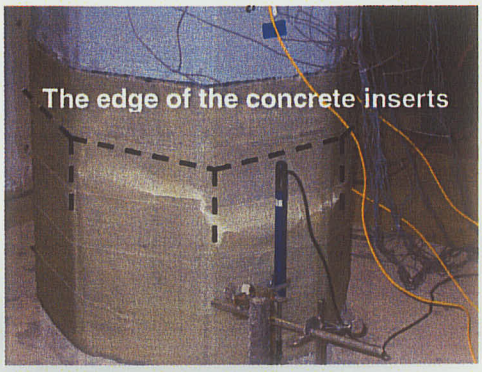

(b) Specimen P3-1R

Figure 5-24 Shear rapture failure for Phase III specimens

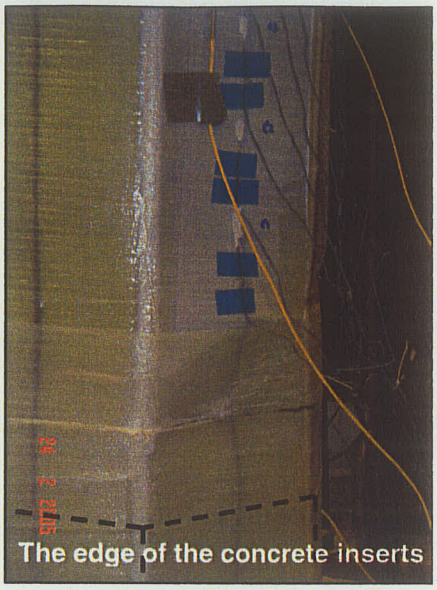

Figure 5-25 Local buckling failure of specimen P3-2

5.5 MATERIAL CHARACTERIZATION

In order to determine the mechanical properties of the FRP materials used in experimental program, several standard tests were conducted according to the current ASTM standards using test coupons described in Chapter 4. The results from these tests are summarized in **Table 5-3**. A more detailed explanation of the stress-strain material characteristics obtained through the mechanized tests is given in the subsequent sections.

Table 5-3 Material properties

Parameters	Units	Filament Wound Coupons (FW)	Unidirectional Coupons (UD)
E_1^t	GPa	23.06	28.49
E_2^t	GPa	5.42	9.38
G_{12}	GPa	2.09	2.41
ν_{12}	-	0.31	0.34
F_1^{tu}	MPa	632.62	597.13
F_2^{tu}	MPa	15.72	18.08
F_1^{cu}	MPa	258.7	361.55
F_2^{cu}	MPa	52.81	65.95
F^{su}	MPa	48.67	47.03

where, E_1 and E_2 are the elastic modulus in the fiber direction, transverse fiber direction, respectively; G_{12} is the shear modulus; F_1^{tu} and F_1^{cu} are the ultimate tensile and compressive strength in the fiber direction, respectively; F_2^{tu} and F_2^{cu} are the ultimate tensile and compressive strength in the transverse fiber direction, respectively; and F^{su} is the ultimate shear strength.

5.5.1 Longitudinal Tensile Stress-Strain Behavior

Typical stress-strain curves obtained from five longitudinal filament wound coupons and five longitudinal unidirectional tensile coupons are illustrated in

Figures 5-26 and **5-27**, respectively. Strain readings were taken from strain gages attached to the coupons. Unfortunately, the ultimate strains could not be recorded since the strain gages have a limited range and they failed before the coupons ultimately failed. The coupons were tested to failure and the ultimate loads were recorded. Based on these loads, the ultimate stress for each coupon was then computed. These ultimate stresses for longitudinal filament wound coupons and longitudinal unidirectional tensile coupons are listed in **Tables 5-4** and **5-5**, respectively. The modulus of elasticity for tension coupons was determined from the linear portion of the stress-strain diagrams.

The values of the modulus of elasticity and the ultimate stress computed according to the rules of mixture using data from the material supplier are 34 GPa and 1600 MPa, respectively. The calculated values of the modulus of elasticity of longitudinal filament wound coupons and longitudinal unidirectional tensile coupons are 23.06 GPa and 28.49 GPa, respectively. The calculated values of the ultimate stress of longitudinal filament wound coupons and longitudinal unidirectional tensile coupons are 632.62 MPa and 579.13 MPa, respectively. These values are lower than those obtained by using data from the manufacturer of the materials and the volume fractions. It should be noted that the physical properties given by manufacturer are those of the fibers prior to any manufacturing process. During fabrication, fibers do break and therefore, not all fibers are available to transfer load. Also, the alignment of the fiber in the coupons affects the ultimate capacity.

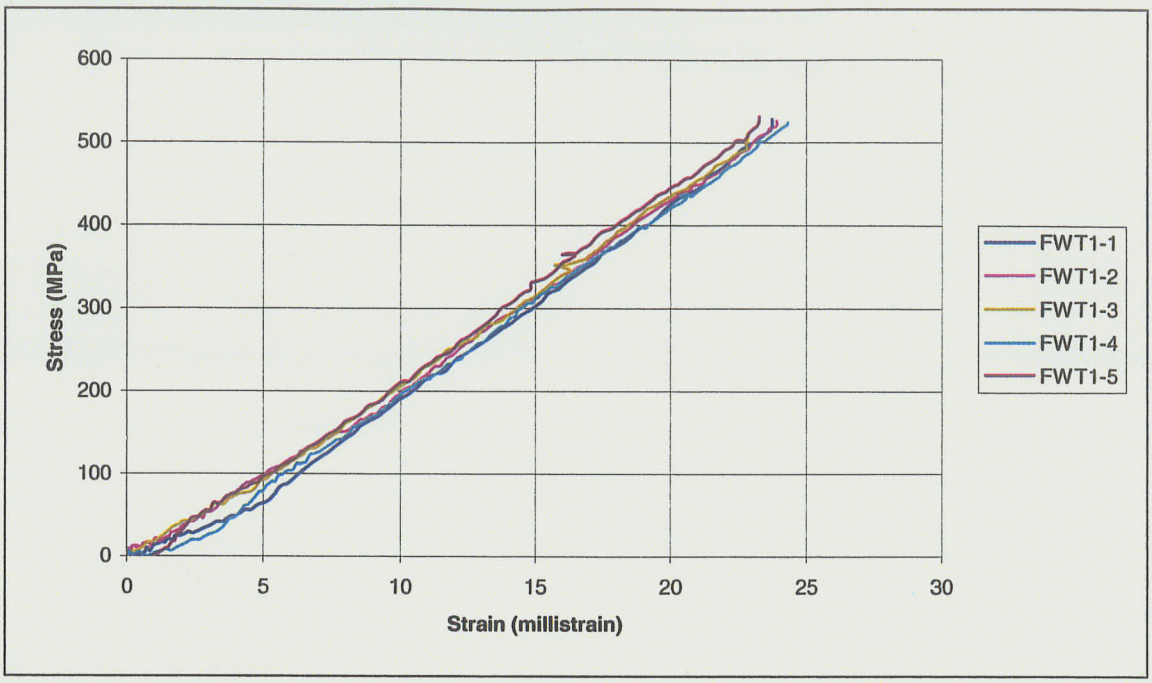

Figure 5-26 Longitudinal tensile stress-strain relationship (FW)

Table 5-4 Longitudinal filament wound tensile coupon test results

Coupon	Area (mm^2)	F_1^{tu} (MPa)	E_1^t (GPa)	υ_{12}^t
FWT1-1	12.50	704.74	23.80	0.32
FWT1-2	12.40	668.74	22.21	0.34
FWT1-3	12.26	551.45	22.65	0.33
FWT1-4	12.47	636.25	22.93	0.25
FWT1-5	12.71	601.93	23.71	0.29
Average	12.47	632.62	23.06	0.31
C.O.V. (%)	1.31	9.37	2.97	11.09

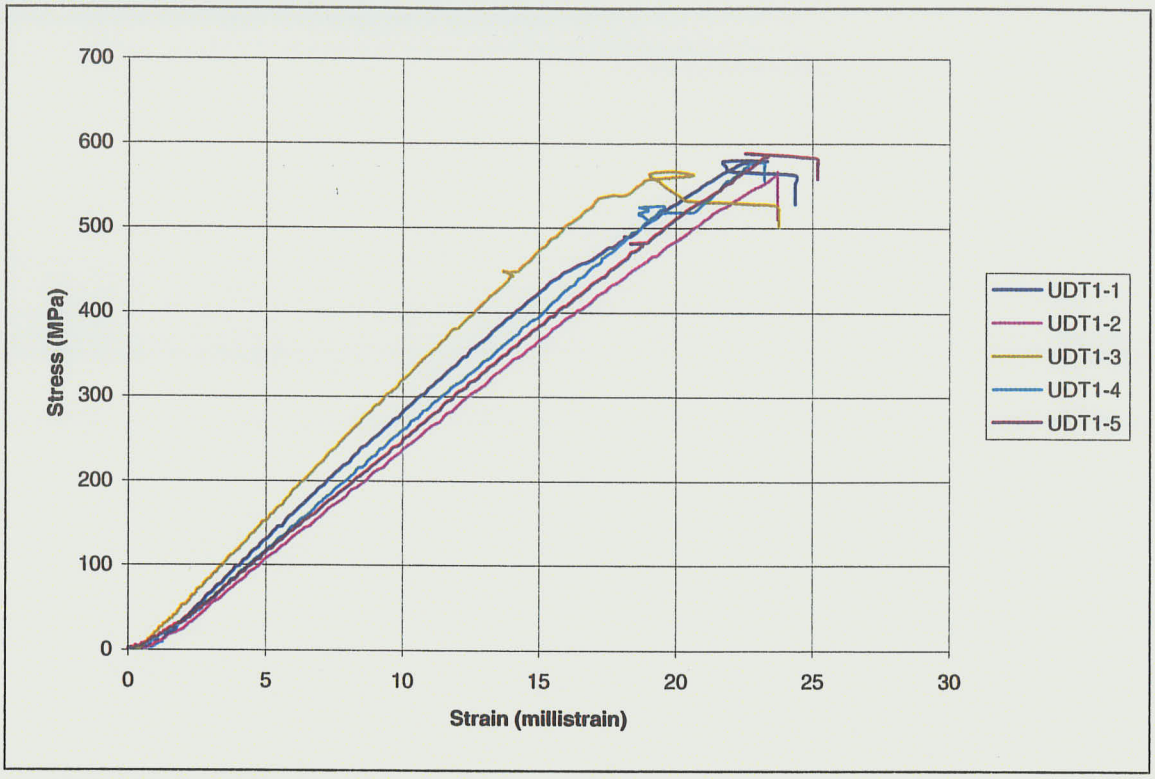

Figure 5-27 Longitudinal tensile stress-strain relationship (UD)

Table 5-5 Longitudinal unidirectional tensile coupon test results

Coupon	Area (mm^2)	F_1^{tu} (MPa)	E_1^t (GPa)	υ_{12}^t
UDT1-1	21.60	579.40	29.69	0.49
UDT1-2	22.17	566.33	25.94	0.32
UDT1-3	21.12	566.23	32.01	0.38
UDT1-4	21.03	590.68	28.07	0.28
UDT1-5	21.69	593.02	26.76	0.25
Average	21.52	579.13	28.49	0.34
C.O.V. (%)	2.15	2.21	8.51	27.62

5.5.2 Transverse Tensile Stress-Strain Behavior

Typical stress-strain curves obtained from five transverse filament wound coupons and five transverse unidirectional tensile coupons are shown in **Figures 5-28** and **5-29**, respectively. Strain readings were taken from strain gages attached to the coupons. The coupons were tested to failure and the ultimate loads were recorded. Based on these loads, the ultimate stress for each coupon was then calculated. These ultimate stresses for transverse filament wound coupons and transverse unidirectional tensile coupons are listed in **Tables 5-6** and **5-7**, respectively. The modulus of elasticity for the tension coupons was computed from the linear portion of the stress-strain diagrams. The calculated values of the modulus of elasticity of transverse filament wound coupons and transverse unidirectional tensile coupons are 5.42 GPa and 9.38 GPa, respectively. The calculated values of the ultimate stress of transverse filament wound coupons and transverse unidirectional tensile coupons are 5.72 MPa and 18.08 MPa, respectively. Both the modulus of elasticity and the ultimate stress of transverse unidirectional tensile coupons were higher than those of transverse filament wound coupons because in the unidirectional coupon there were fibers woven in the transverse direction. Even though these fibers are used to form the unidirectional matt, they also provide some load resistance in the transverse direction.

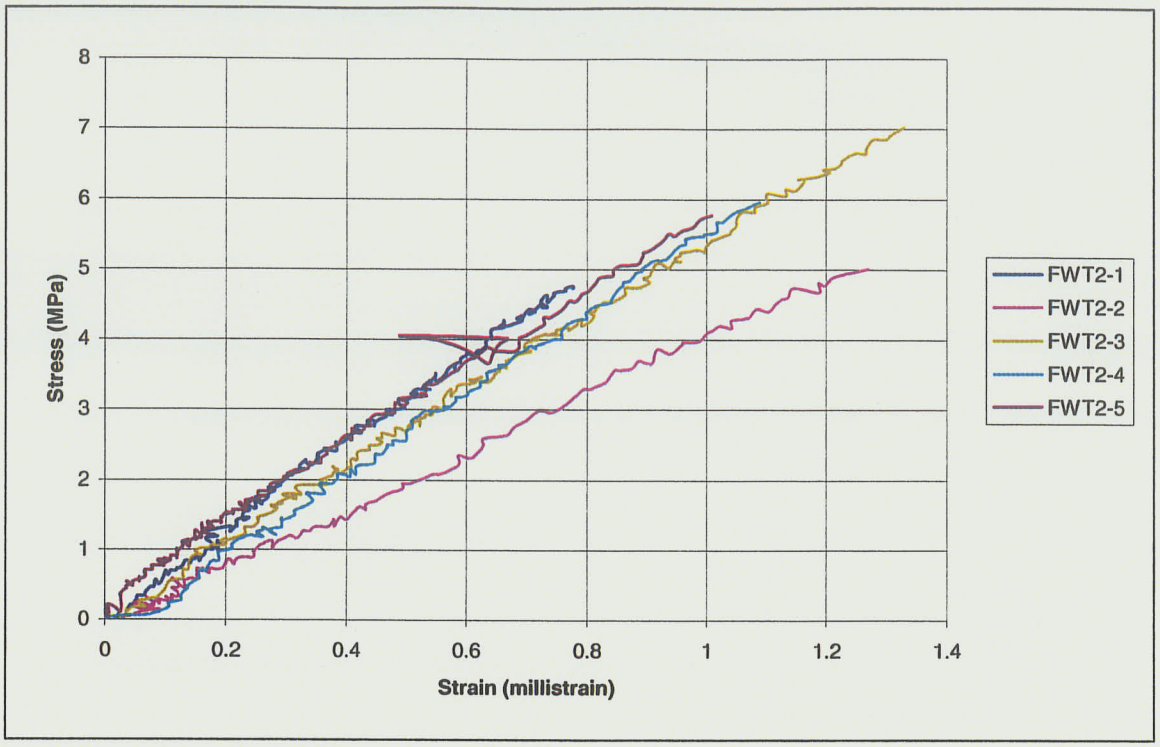

Figure 5-28 Transverse tensile stress-strain relationship (FW)

Table 5-6 Transverse filament wound tensile coupon test results

Coupon	Area (mm^2)	F_2^{tu} (MPa)	E_2^t (GPa)	υ_{21}^t
FWT2-1	28.90	4.76	6.38	0.075
FWT2-2	28.09	5.00	4.06	0.106
FWT2-3	28.28	7.02	5.33	0.077
FWT2-4	27.37	5.95	5.74	0.076
FWT2-5	28.63	5.84	5.58	0.109
Average	28.25	5.72	5.42	0.088
C.O.V. (%)	2.07	15.60	15.74	19.71

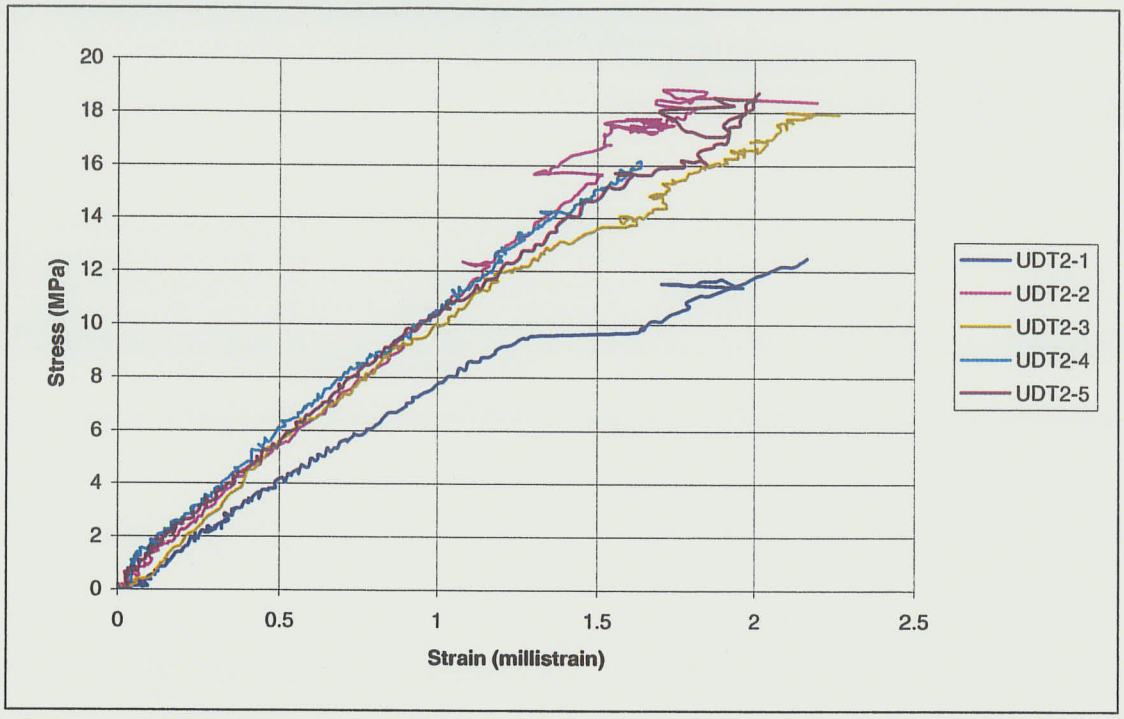

Figure 5-29 Transverse tensile stress-strain relationship (UD)

Table 5-7 Transverse unidirectional tensile coupon test results

Coupon	Area (mm^2)	F_2^{tu} (MPa)	E_2^t (GPa)	υ_{21}^t
UDT2-1	47.48	14.59	7.67	0.10
UDT2-2	47.36	18.85	10.37	0.14
UDT2-3	48.58	20.94	9.61	0.12
UDT2-4	47.85	16.16	9.59	0.11
UDT2-5	46.96	19.85	9.65	0.12
Average	47.65	18.08	9.38	0.12
C.O.V. (%)	1.28	14.57	10.76	13.00

5.5.3 Longitudinal Compressive Stress-Strain Behavior

Stress-strain curves obtained from five transverse filament wound coupons and five transverse unidirectional compression coupons are shown in **Figures 5-30** and **5-31**, respectively. The coupons were tested to failure and the ultimate loads were recorded. Based on these loads and the measured cross-section area of the coupons, the ultimate compressive stress for each coupon was then computed. These ultimate stresses for longitudinal filament winding coupons and longitudinal unidirectional compression coupons are summarized in **Tables 5-8** and **5-9**, respectively. The modulus of elasticity for the compression coupons was calculated from the linear segment of the stress-strain diagrams. The calculated values of the modulus of elasticity of longitudinal filament wound coupons and longitudinal unidirectional compression coupons are 36.10 GPa and 46.69 GPa, respectively. The calculated ultimate stress of longitudinal filament winding coupons and longitudinal unidirectional compression coupons are 258.70 MPa and 361.55 MPa, respectively. It should be noted that the ultimate tensile stress of both filament wound coupons and unidirectional coupons is much higher then the ultimate compressive stress as composites tend to be weaker in compression due to buckling of the fibers.

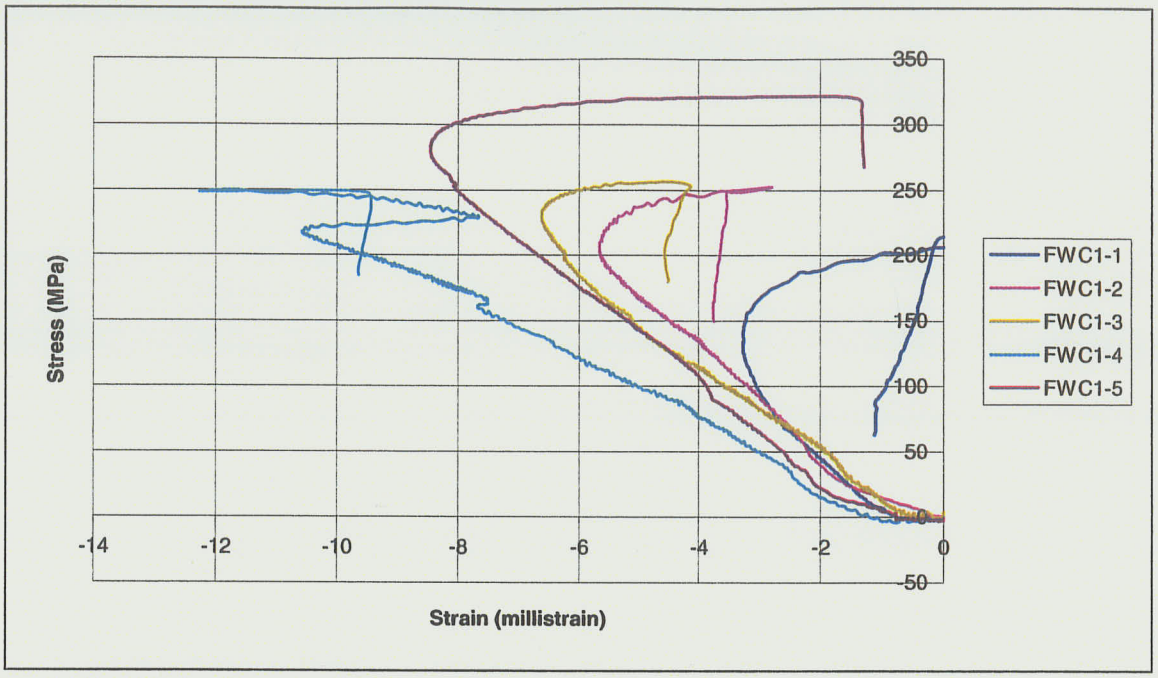

Figure 5-30 Longitudinal compressive stress-strain relationship (FW)

Table 5-8 Longitudinal filament wound compression coupon test results

Coupon	Area (mm^2)	F_1^{cu} (MPa)	E_1^c (GPa)	υ_{12}^c
FWC1-1	11.52	214.69	45.33	0.32
FWC1-2	11.67	252.06	41.99	0.46
FWC1-3	11.57	256.13	32.76	0.31
FWC1-4	12.25	249.21	23.97	0.43
FWC1-5	12.59	321.39	36.44	0.28
Average	11.92	258.70	36.10	0.36
C.O.V. (%)	4.00	14.98	23.11	22.51

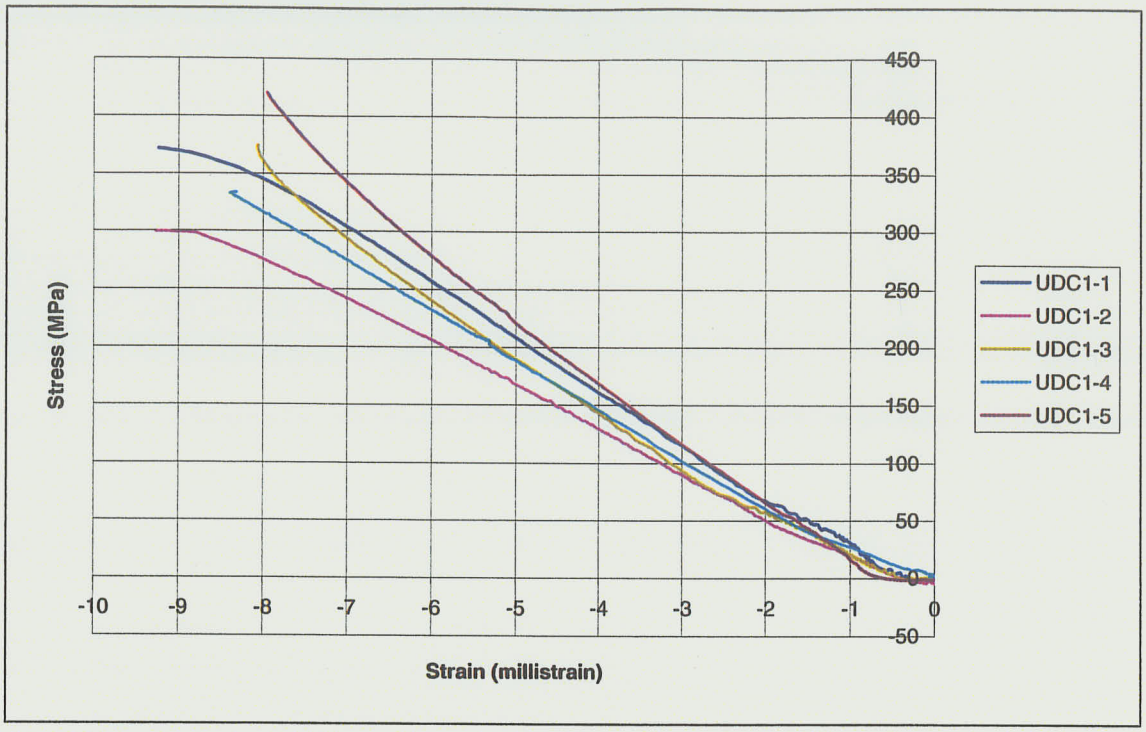

Figure 5-31 Longitudinal compressive stress-strain relationship (UD)

Table 5-9 Longitudinal unidirectional compression coupon test results

Coupon	Area (mm^2)	F_1^{cu} (MPa)	E_1^c (GPa)	υ_{12}^c
UDC1-1	21.99	372.16	47.81	0.28
UDC1-2	22.23	299.53	38.69	0.38
UDC1-3	21.58	375.29	48.41	0.37
UDC1-4	21.74	333.33	43.30	0.38
UDC1-5	21.49	427.41	55.22	0.37
Average	21.61	361.55	46.69	0.36
C.O.V. (%)	1.29	13.32	13.23	11.78

5.5.4 Transverse Compressive Stress-Strain Behavior

Typical stress-strain diagrams obtained from five transverse filament wound coupons and five transverse unidirectional compression coupons are shown in **Figures 5-32** and **5-33**, respectively. The coupons were tested to failure and the ultimate loads were recorded. Coupon FWC2-1 failed prematurely during installation in the test fixture. Therefore, this coupon was not included in the analysis of the results. In addition, the strain gage used in coupon UDC2-3 failed to work properly due to poor bonding. The ultimate stress for each coupon was then calculated using the measured cross-section area of the coupons and the ultimate load recorded during the testing. The test results of both transverse filament wound coupons and transverse unidirectional compression coupons are summarized in **Tables 5-10** and **5-11**, respectively. The modulus of elasticity for compression coupons was computed from the linear segment of the stress-strain curves. The calculated values of the modulus of elasticity of transverse filament winding coupons and transverse unidirectional compression coupons are 11.81 GPa and 13.80 GPa, respectively. The ultimate compressive stress of transverse filament wound coupons and transverse unidirectional coupons are 52.81 MPa and 62.95 MPa, respectively. The transverse compressive stress is much higher than the transverse tensile stress as expected since the transverse tensile stress is based on the bond strength between the fibers and resin only.

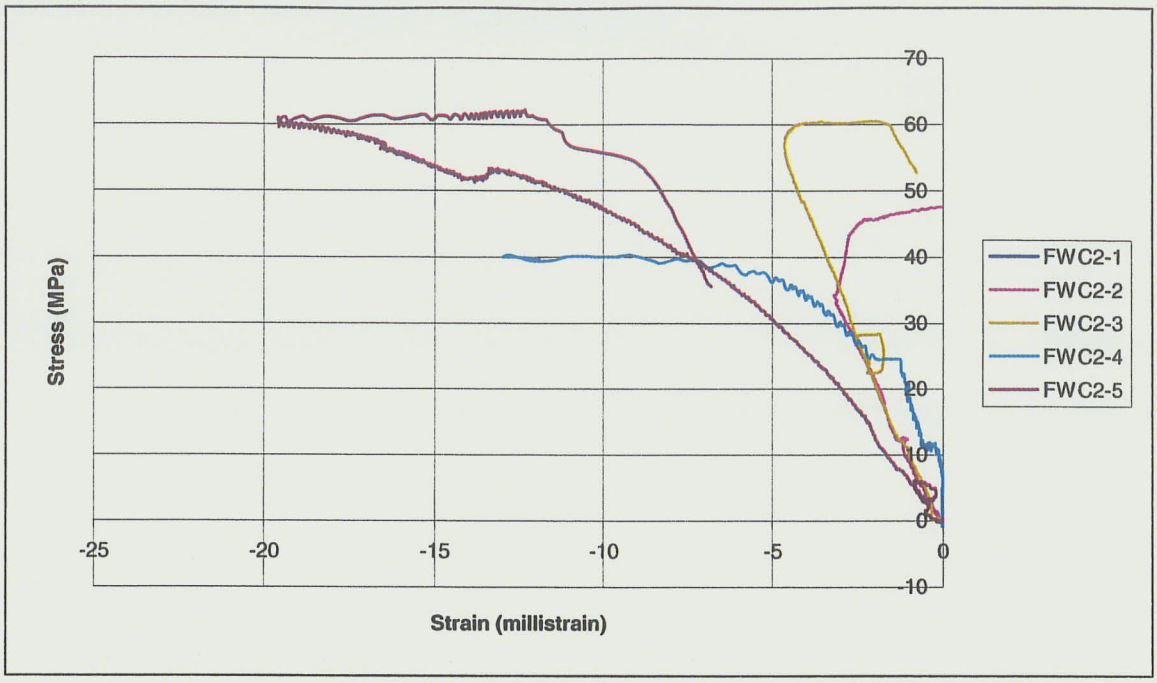

Figure 5-32 Transverse compressive stress-strain relationship (FW)

Table 5-10 Transverse filament wound compression coupon test results

Coupon	Area (mm^2)	F_2^{cu} (MPa)	E_2^c (GPa)	υ_{21}^c
FWC2-1	10.79	-	-	-
FWC2-2	11.35	48.18	10.86	0.09
FWC2-3	11.23	60.51	12.32	0.12
FWC2-4	12.46	40.29	16.50	0.15
FWC2-5	12.55	62.26	7.57	0.10
Average	11.68	52.81	11.81	0.12
C.O.V. (%)	6.74	19.77	31.37	22.32

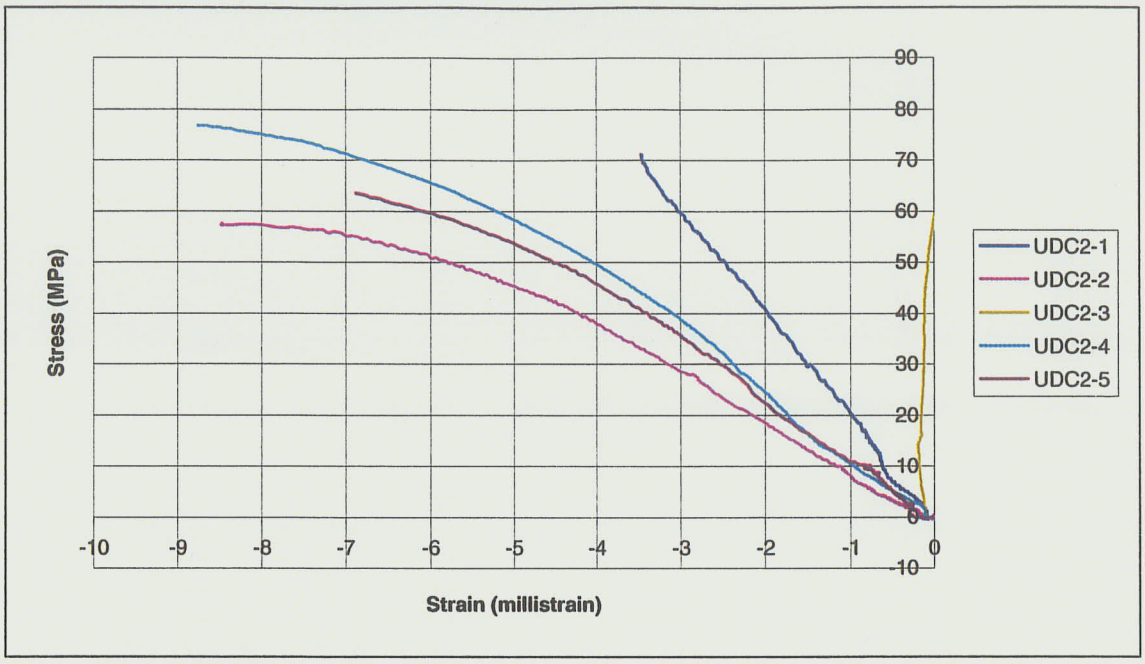

Figure 5-33 Transverse compressive stress-strain relationship (UD)

Table 5-11 Transverse unidirectional compression coupon test results

Coupon	Area (mm^2)	F_2^{cu} (MPa)	E_2^c (GPa)	υ_{21}^c
UDC2-1	19.39	72.52	19.83	0.13
UDC2-2	20.06	57.46	10.20	0.08
UDC2-3	19.99	59.95	-	-
UDC2-4	20.30	75.71	13.57	0.10
UDC2-5	17.37	64.10	11.61	0.09
Average	19.42	65.95	13.80	0.10
C.O.V. (%)	6.14	11.99	30.81	22.41

5.5.5 Shear Stress-Strain Behavior

The stress-strain curves for both filament wound and unidirectional coupons are illustrated in **Figures 5-34** and **5-35**, respectively. The strain gages recorded strain up to failure. The coupons were tested to failure and the ultimate loads were recorded. The shear modulus for the tested coupons was calculated from the linear portion of the stress-strain curves. The ultimate shear stress was computed using the measured shear areas of the coupons and the ultimate load attained. The results of both filament wound and unidirectional coupons are listed in **Tables 5-12** and **5-13**, respectively. The calculated values of the shear modulus of filament wound and unidirectional coupons are 2.09 GPa and 2.41 GPa, respectively. The ultimate shear stresses of filament winding and unidirectional coupons are 48.67 MPa and 47.03 MPa, respectively. It can be seen that the measured shear modulus and shear stress of both filament winding and unidirectional coupons are similar, since the same glass fibers were used in both coupons.

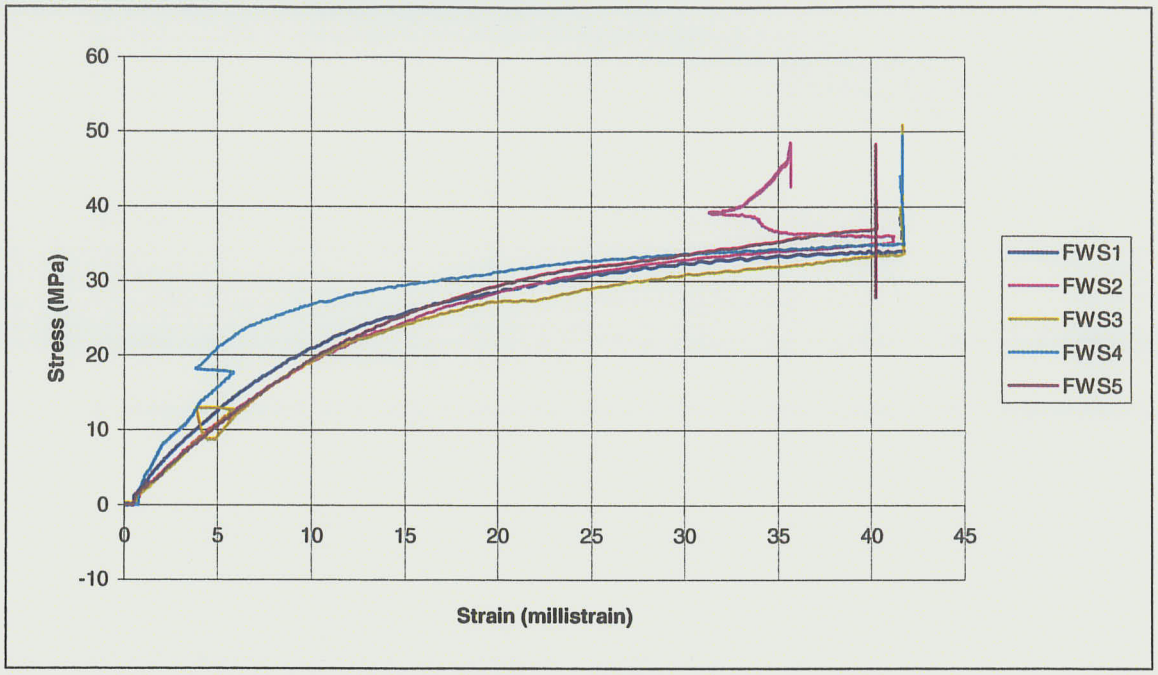

Figure 5-34 Shear stress-strain relationship (FW)

Table 5-12 Filament wound shear coupon test results

Coupon	Area (mm^2)	F^{su} (MPa)	G_{12} (GPa)
FWS1	20.34	46.02	1.93
FWS2	20.77	48.59	1.88
FWS3	19.67	50.90	1.92
FWS4	19.81	49.52	2.81
FWS5	20.53	48.35	1.92
Average	20.22	48.67	2.09
C.O.V. (%)	2.33	3.68	19.25

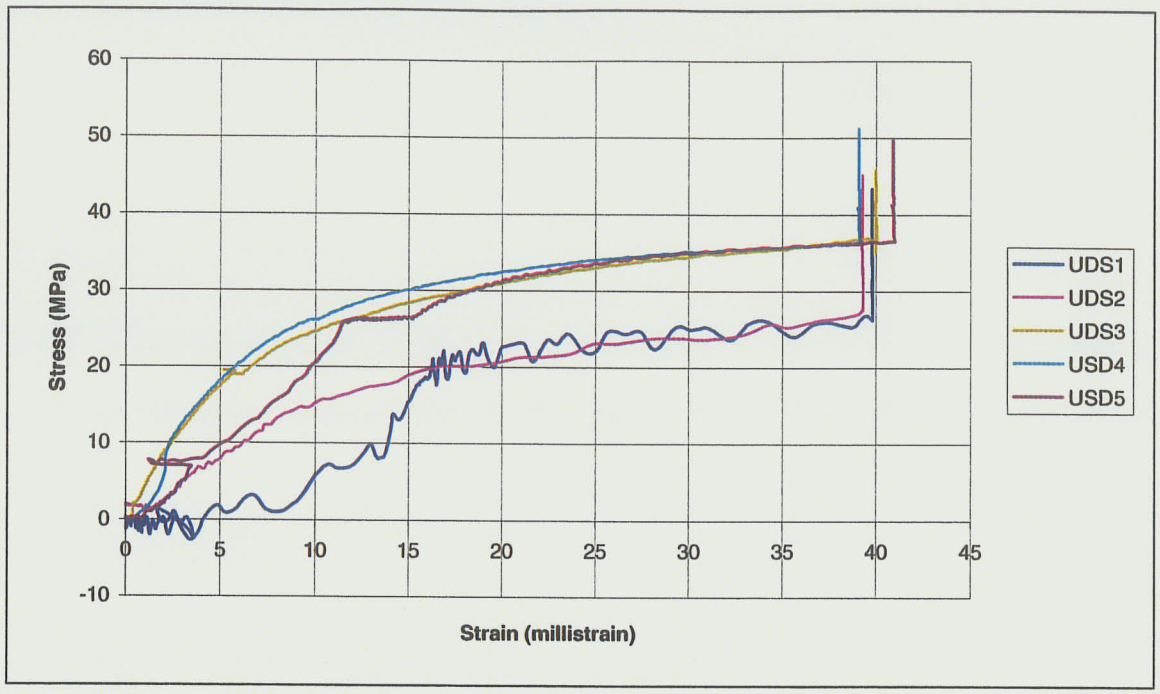

Figure 5-35 Shear stress-strain relationship (UD)

Table 5-13 Unidirectional shear coupon test results

Coupon	Area (mm^2)	F^{su} (MPa)	G_{12} (GPa)
UDS1	21.97	43.38	2.54
UDS2	21.10	45.06	1.69
UDS3	21.30	45.71	2.79
UDS4	20.93	51.24	2.93
UDS5	21.39	49.78	2.08
Average	21.34	47.03	2.41
C.O.V. (%)	1.85	7.08	21.49

CHAPTER 6

NUMERICAL ANALYSIS

6.1 GENERAL

Since the multi-cell segmented FRP wind turbine tower has been proposed as an alternative tower for use in remote areas where the cost of transportation and erection prohibits the use of tubular steel towers as well as in offshore applications, an understanding of their structural behavior is needed before developing design guidelines. Knowledge of this structural behavior could be obtained from testing multi-cell segmented FRP towers and interpreting the results. However, it is unrealistic and costly to acquire the structural behavior entirely from test results. Hence, it is vital to develop analytical tools that are capable of predicting the structural behavior of multi-cell segmented FRP towers without the need for extensive experimental testing. The analytical models must, however, be validated through comparison with experimental results.

In the current study, the ANSYS software program was used to develop a finite element model to simulate the structural behavior of single cells under lateral

bending and compression as well as that of eight-cell jointed towers under lateral bending. Large deflections and cross-section distortion were taken into account in the analysis and proper failure criteria were used in order to determine the ultimate load. This model was verified through comparison with the experimental results obtained from the static testing of specimens in Phase I, Phase II and Phase III of the research program.

6.2 FINITE ELEMENT MODELING

The basic concept of a finite element technique is to use a finite number of defined elements whose displacement behavior is described by a fixed number of degrees of freedom to predict the structural behavior of structures.

6.2.1 Element Selection

In this study, to model the composite tower, an eight-node quadrilateral layered shell element was used. This element, which is designated by ANSYS as SHELL 99, is a 100 layer shell structure, as shown in **Figure 6-1**. The element has six degrees of freedom at each node, translations in the nodal x, y, and z directions, and rotations about the nodal x, y, and z axes.

This element was chosen because of its ability to: a) handle unlimited number of layers with constant or variable thickness; b) account for large deflections; c) predict failure by the means of three different failure criteria; and, d) handle membrane stresses and strains in the process. The material properties are defined for this element in terms of the principal axes of the element. Using a single lamina for reference, the element coordinate system defines the x-axis as running parallel to the fibers direction, the y-axis as running perpendicular to the fiber direction, and the z-axis as running through the thickness of the element, as shown **Figure 6-2.**

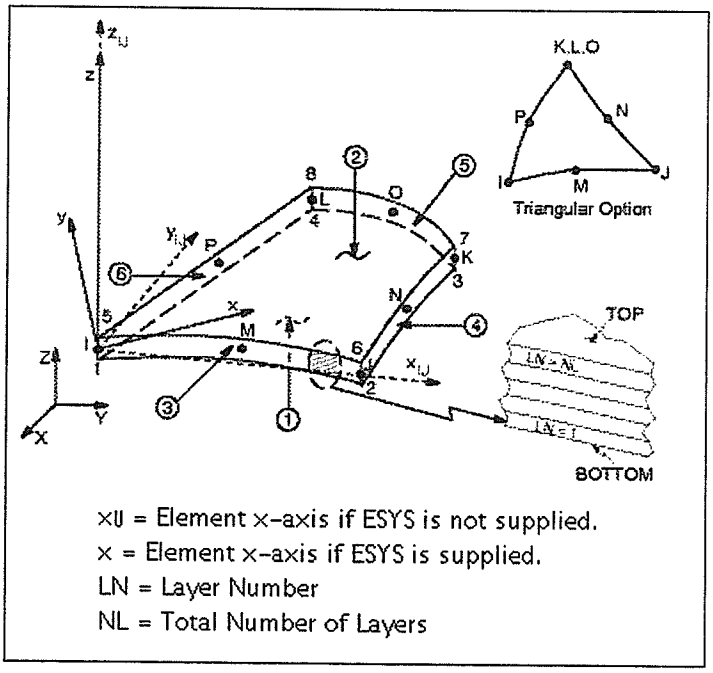

Figure 6-1 SHELL99 linear layered structural shell (ANSYS, 2002)

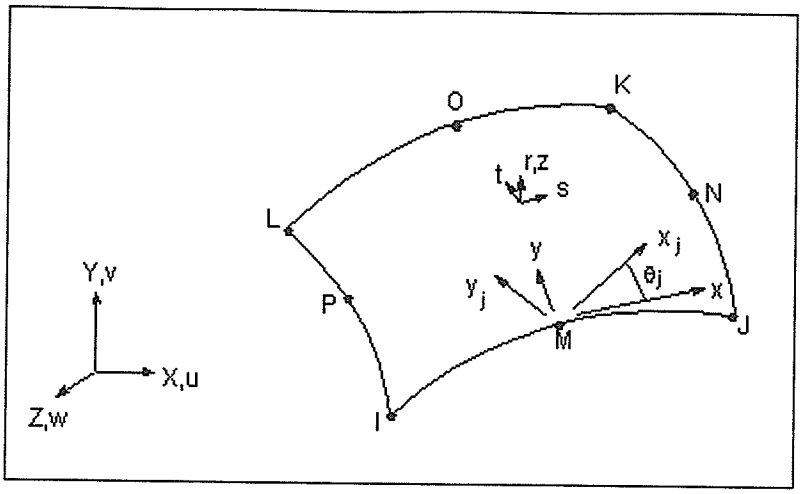

Figure 6-2 Element coordinate system (ANSYS, 2002)

6.2.2 Failure Criterion

The Tsai-Wu failure criterion was adopted in the analysis to predict the ultimate capacity of the composite structures by using the stresses obtained from a finite element analysis and then comparing them to the material strengths. This failure criterion was chosen since it accounts for the interaction between different stress components. In the Tsai-Wu failure criterion, the failure surface in the stress space is described by the following equation:

$$\xi = A + B \qquad \textit{Equation 6.1}$$

where

ξ = value of Tsai-Wu failure criterion

$$A = -\frac{(\sigma_x)^2}{\sigma_{xt}^f \sigma_{xc}^f} - \frac{(\sigma_y)^2}{\sigma_{yt}^f \sigma_{yc}^f} - \frac{(\sigma_z)^2}{\sigma_{zt}^f \sigma_{zc}^f} + \frac{(\sigma_{xy})^2}{(\sigma_{xy}^f)^2} + \frac{(\sigma_{yz})^2}{(\sigma_{yz}^f)^2} + \frac{(\sigma_{xz})^2}{(\sigma_{xz}^f)^2}$$
$$+ \frac{C_{xy}\sigma_x\sigma_y}{\sqrt{\sigma_{xt}^f \sigma_{xc}^f \sigma_{yt}^f \sigma_{yc}^f}} + \frac{C_{yz}\sigma_y\sigma_z}{\sqrt{\sigma_{yt}^f \sigma_{yc}^f \sigma_{zt}^f \sigma_{zc}^f}} + \frac{C_{xz}\sigma_x\sigma_z}{\sqrt{\sigma_{xt}^f \sigma_{xc}^f \sigma_{zt}^f \sigma_{zc}^f}}$$

$$B = \left(\frac{1}{\sigma_{xt}^f} + \frac{1}{\sigma_{xc}^f}\right)\sigma_x + \left(\frac{1}{\sigma_{yt}^f} + \frac{1}{\sigma_{yc}^f}\right)\sigma_y + \left(\frac{1}{\sigma_{zt}^f} + \frac{1}{\sigma_{zc}^f}\right)\sigma_z$$

In order to avoid failure, the value of the ξ must be less than unity, and hence, the structural failure is predicted when ξ is equal to or greater than unity. The terms in **Equation 6.1** are defined as fellows:

σ_x, σ_y, and σ_z are stresses obtained from the analysis of any layers in the x, y, and z directions, respectively;

σ_{xy}, σ_{yz}, and σ_{xz} are shear stresses obtained from the analysis of any layers in the xy, yz, and xz planes, respectively;

σ_{xt}^f, and σ_{xc}^f are the tensile and compressive failure stresses of the material in the x direction, respectively;

σ_{yt}^f, and σ_{yc}^f are the tensile and compressive failure stresses of the material in the y direction, respectively;

σ_{zt}^f, and σ_{zc}^f are the tensile and compressive failure stresses of the material in the z direction, respectively;

σ_{xy}^f, σ_{yz}^f, and σ_{xz}^f are the failure shear stresses of the material in the xy, yz, and xz planes, respectively; and

C_{xy}, C_{yz}, and C_{xz} are the coupling coefficients used in the Tsai-Wu theory in the xy, yz, and xz planes, respectively.

The Tsai-Wu coupling coefficient must be between -1.0 and 1.0. This requirement is necessary to ensure that the failure surface intercepts each stress axis and the shape of the surface is a closed one.

6.2.3 Geometric Nonlinearity

An FRP structure experiences large deformations during testing, and therefore, changes in its geometric configuration take place that cause the structure to respond in a nonlinear fashion. Thus, the geometric nonlinearity must be taken into account in the analysis. The large deflections result in changes to the element orientation, and, consequently, changes in the element stiffness matrix. To deal with this problem, the element stiffness matrix is continuously updated using the Newton-Raphson iterative procedure. The Newton-Raphson method is based on the incremental procedure in which a series of successive linear iterations converge to the actual nonlinear solution, as illustrated in **Figure 6-3**. In this procedure, the element tangent stiffness matrix is updated as given in following expression:

$$[K_e] = \int_{vol} [T_n]^T [B_v][D][B_v][T_n] d(vol) \qquad \textbf{Equation 6.2}$$

where, $[T_n]$ is the orthogonal transformation matrix relating the original element coordinates to the deformed element coordinates. The deformed element coordinate differs from the original element coordinate by the amount of rigid body rotation. Hence, $[T_n]$ is computed by separating the rigid body rotation from the total deformation $\{u_n\}$ using the polar decomposition theorem.

The element restoring force is:

$$\{F_e\} = \int_{vol} [T_n]^T [B_v][D]\{\varepsilon_n^{el}\} d(vol) \qquad \textbf{Equation 6.3}$$

where, the elastic strain is computed from:

$$\{\varepsilon_n^{el}\} = [B_v]\{u_n^d\} \qquad \textbf{Equation 6.4}$$

and $\{u_n^d\}$ is the element deformation which causes straining.

The process used to account for the large deflections can be summarized as a three-step process for each element:

1. Determine the updated transformation matrix $[T_n]$ for the element;
2. Extract the deformational displacement from the total element displacement $\{u_n\}$ for computing the stresses as well as the restoring force $\{F_e\}$; and,

3. After the rotational increments in $\{\Delta u\}$ are computed, update the node rotations appropriately.

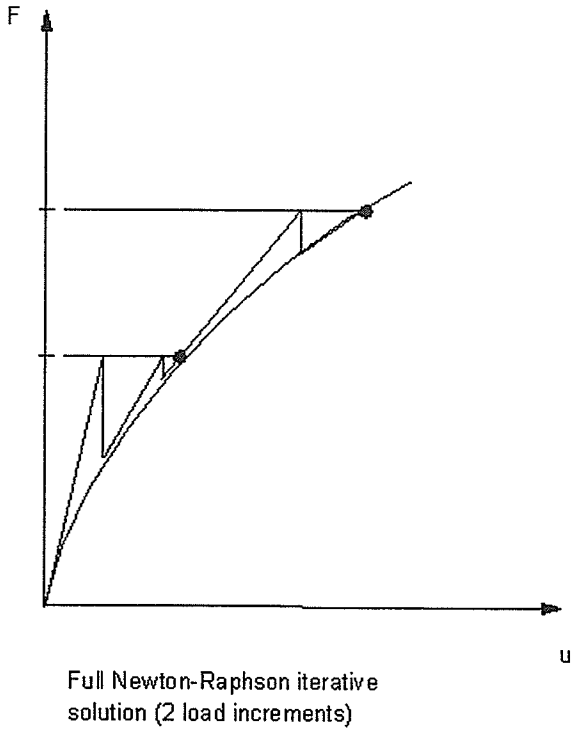

Figure 6-3 Newton-Raphson iterative procedure (ANSYS, 2002)

6.3 FINITE ELEMENT ANALYSIS OF TESTED SPECIMENS AND DISCUSSION OF THE RESULTS

The finite element model discussed in the previous section was used to analyze the specimens tested in Phases I, II, and III specimens. The main objective of this analysis was to determine the ultimate load carrying capacity, the tip deflection at the failure, and the failure mode of tested specimens and compare

those to the experimental results. The load-deflection curves as well as the strain distribution within the specimens were also obtained through the analysis and the results were compared to the experimental results.

6.3.1 Modeling of Specimens in Phase I

As the first step in the modeling process, the geometric boundaries of the single cell specimen (Phase I specimen) were defined. Key points were applied to define those boundaries and the surface areas were then generated. Finally, the corners of the sections were filleted to model the actual specimen dimensions.

Once the geometric shape of the specimen was established, the discretization process was performed to subdivide the FRP specimen into equivalent finite element systems. It is commonly known that the more refined the finite element mesh is, the more accurate the results. Therefore, a fine mesh was then applied in the bottom part of the specimens where the failure was expected to occur. A coarser finite element mesh was used in the upper portion of the FRP specimens. One thousand and eight hundred elements were used to model the specimens in Phase I, as illustrated in **Figure 6-4**.

The element size was gradually increased with an aspect ratio of 1:5 at the base toward the top of the specimen. All degrees of freedom (u_x, u_y, u_z, rot_x, rot_y, and rot_z) were restrained at the end of the composite sleeve or at 312 mm from the

base to simulate the fixed end condition. To simulate the concentrated load applied to the specimen at 97 mm below the top of the specimen, loads were assigned to all the nodes at the location. The load was applied in 500 N increments to a maximum load of 5000 N, in order to obtain a load-time response of the model.

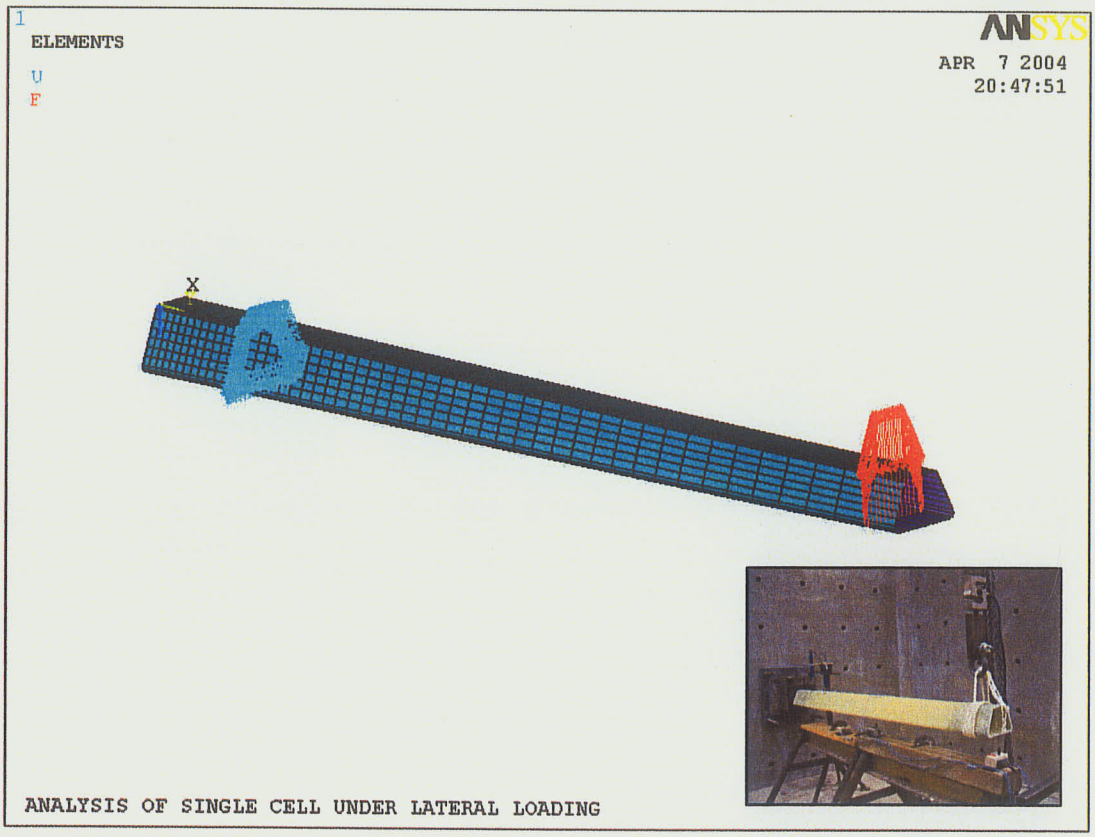

Figure 6-4 ANSYS FEM model of Phase I specimen

In the current study, the geometric nonlinear analysis was taken into account for large deformations. To determine the ultimate load carrying capacity of the specimens in Phase I, the Tsai-Wu failure criterion was adopted. The ultimate load was obtained when the failure criterion is equal to unity unless divergence

occurred prior to reaching this failure criterion. Divergence of the solution indicates that local buckling occurs within the specimen.

A typical input file for Phase I specimens using the ANSYS finite element software program is given in **Appendix C**.

The finite element results of a Phase I specimen show the divergence of the solution prior to reaching the failure criterion indicating the occurrence of local buckling within the model. **Figure 6-5** shows the distribution of Tsai-Wu failure criteria values. The maximum Tsai-Wu value, which occurred on the tension side, was 0.83. The criterion value was less than unity, which indicates that the specimen did not suffer a material failure. The local buckling failure occurred on the compression side near the base of the specimen, as illustrated in **Figure 6-6**. This failure matches well with the experimental results.

The load-tip deflections from both the experimental program and the finite element results are shown in **Figure 6-7**. The ultimate load predicted by the finite element model correlated well with the results obtained from the experiment. The average failure load of 3.72 kN was closed to the failure load of 4.05 kN predicted by the finite element model, as listed in **Table 6-1**. The average ultimate tip deflection obtained from the experimental program was 156.81 mm, which was slightly higher than 132.56 mm obtained from the finite element model. Furthermore, the average stiffness obtained from experimental

data was 24.25 kN/m, which was comparable to 30.5 kN/m predicted by the finite element model.

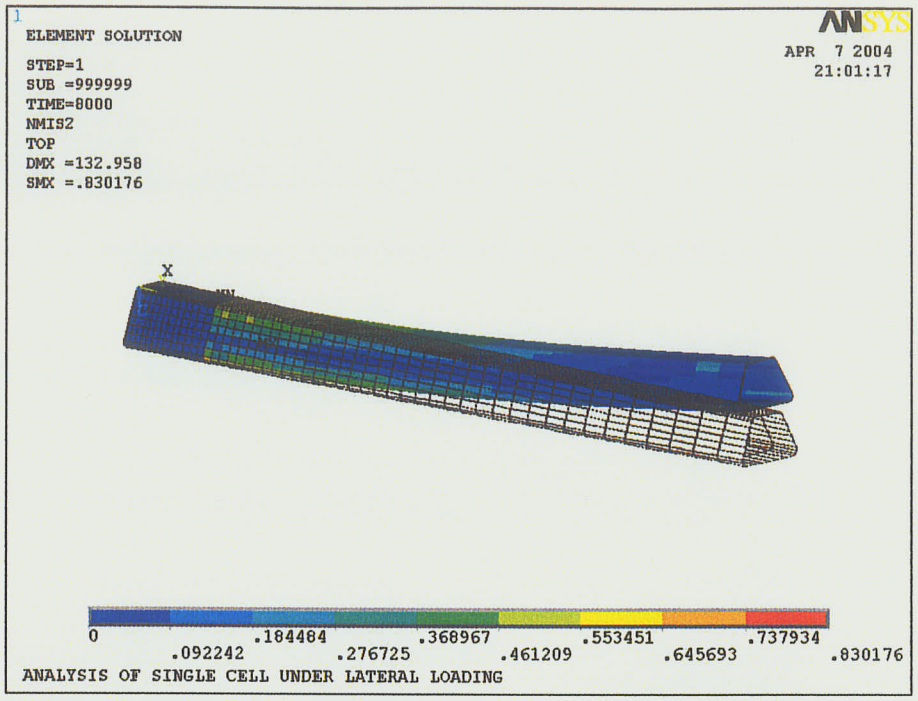

Figure 6-5 Distribution of Tsai-Wu failure criteria values for Phase I specimens

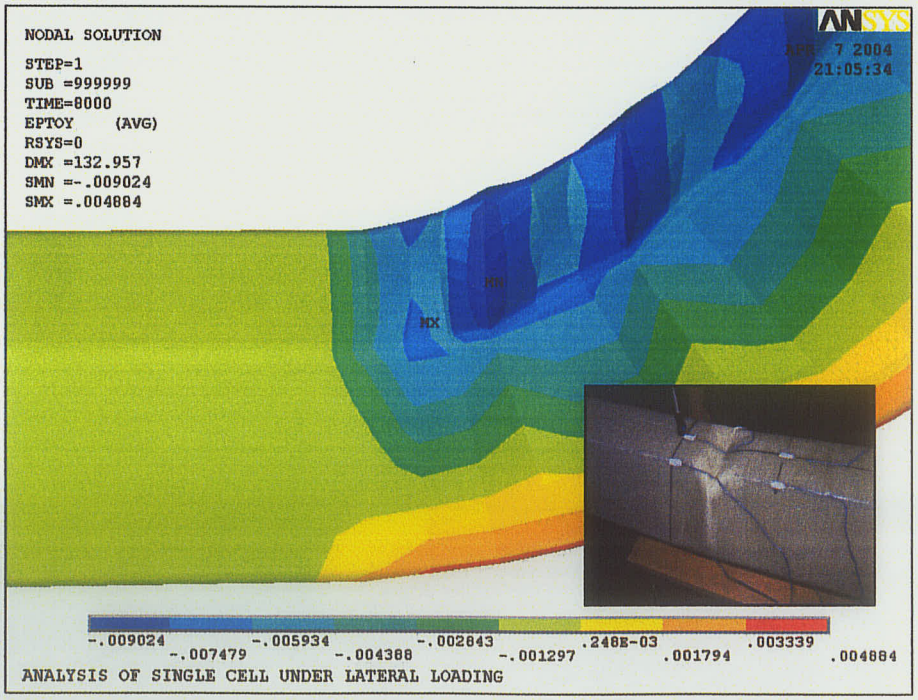

Figure 6-6 Local buckling of Phase I specimen

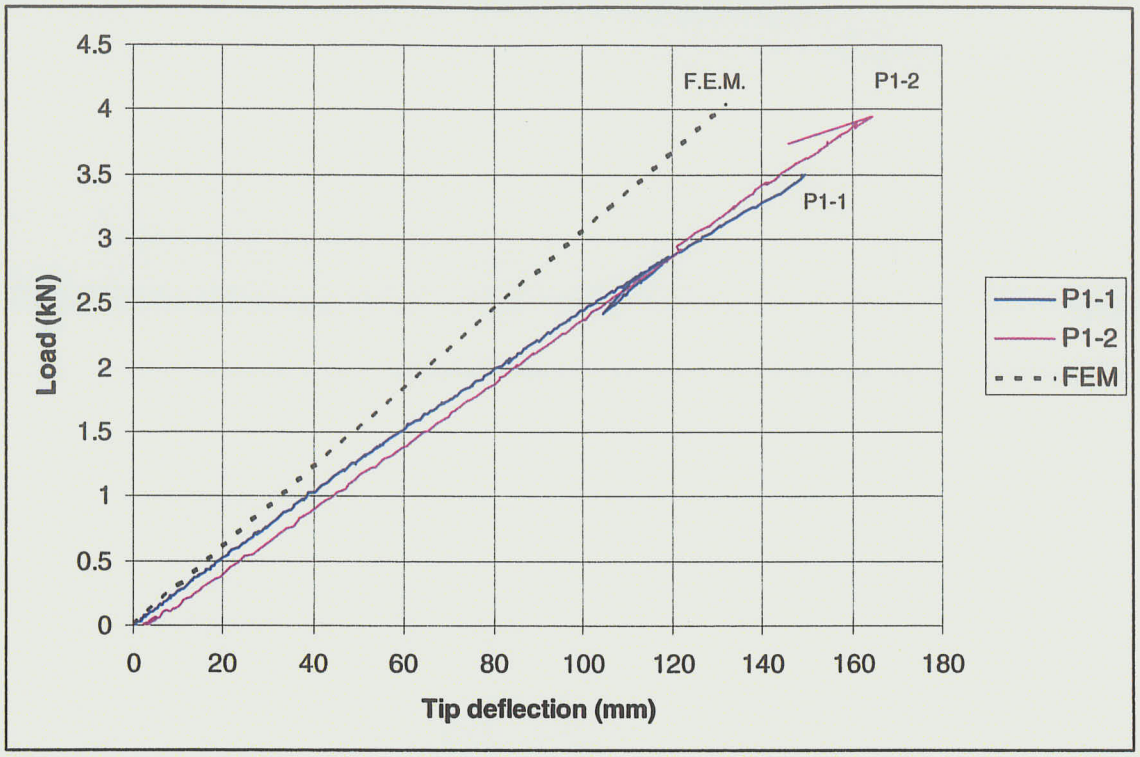

Figure 6-7 Load-tip deflection diagram comparison for Phase I specimens

Table 6-1 Comparison between experimental and finite element results for Phase I specimens

Specimen	Ultimate load (kN)	Tip deflection (mm)	Stiffness (kN/m)
P1-1 P1-2	3.50 3.94	149.09 164.52	24.90 23.60
Average	3.72	156.81	24.25
F.E.M.	4.05	132.56	30.50

6.3.2 Modeling of Specimens in Phase II

The same procedure used to model the specimen in Phase I was used to create the geometric shape of the Phase II specimens. The same key points were applied to define the boundaries and surface areas were then generated. As before, the corners were filleted to model the actual specimen dimensions. The discretization process was then performed to subdivide the FRP specimen into equivalent finite element systems. Five hundred and seventy six elements were used to model the Phase II specimens, as shown in **Figure 6-8**.

The element size used was constant throughout the model. Degrees of freedom (u_x, u_y, and u_z) were restrained at the base to simulate the pinned support condition.

The buckling analysis was used to determine the ultimate load in this case. A unit load is usually used to extract the eigenvalues. The eigenvalues calculated by the buckling analysis represent buckling load factors. Therefore, if a unit load is specified, the load factors represent the buckling loads. In this study, a unit load was used and was divided by the number of nodes at the top of the model in order to determine the constant load per node. This load was later assigned to all nodes at that location. A typical input file for Phase II specimens using ANSYS finite element software program is given in **Appendix C**.

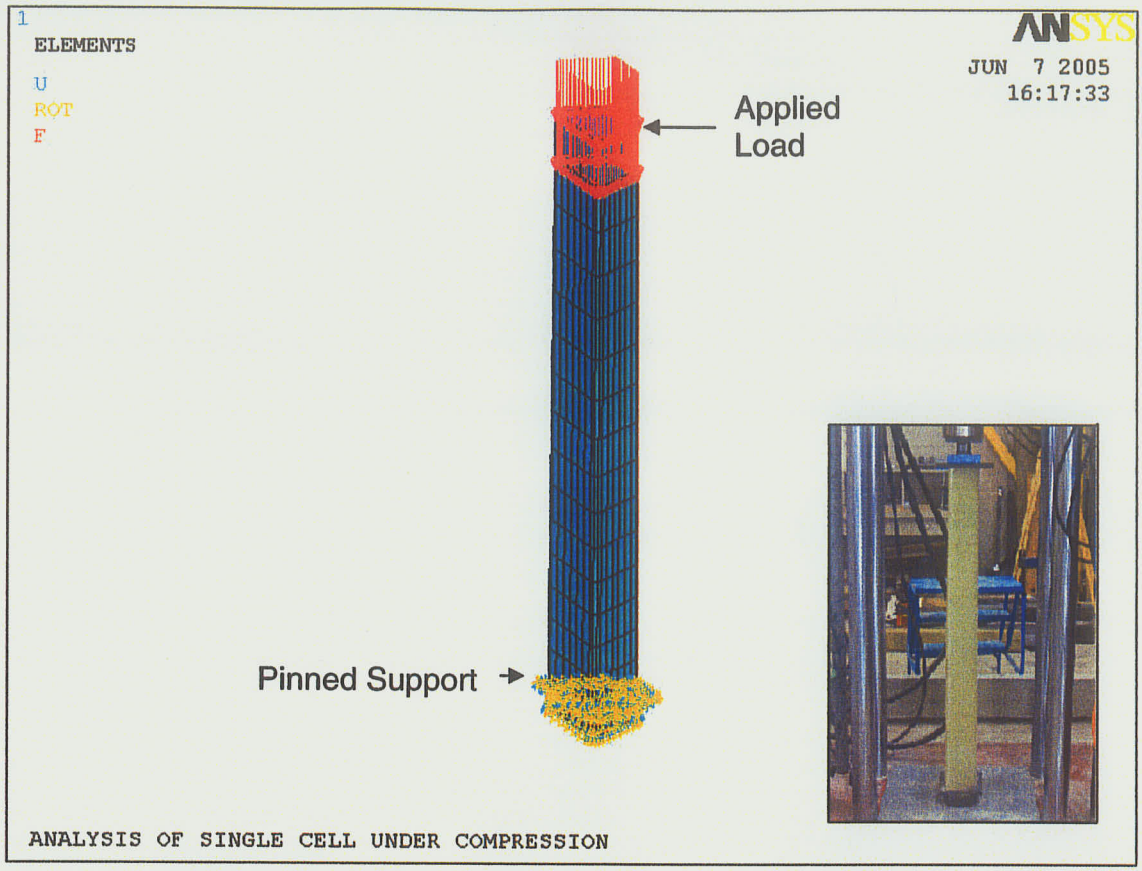

Figure 6-8 ANSYS FEM model of Phase II specimen

The finite element model was used to predict the ultimate failure load for the specimens in Phase II. **Figure 6-9** shows the theoretical deformed shape of specimen P2-1280-1 at the ultimate load. The buckled shape of the specimen has a strong correlation with that observed in the experimental program.

The failure loads obtained from experimental program and the failure loads obtain from the finite element model for Phase II specimens are listed in **Table 6-2**. The ratio between the experimental failure load and the finite element failure load is also given in **Table 6-2**. The average ratio was 0.891. This indicates that

there was a good correlation between the failure load predicted by the finite element model and the experimental results.

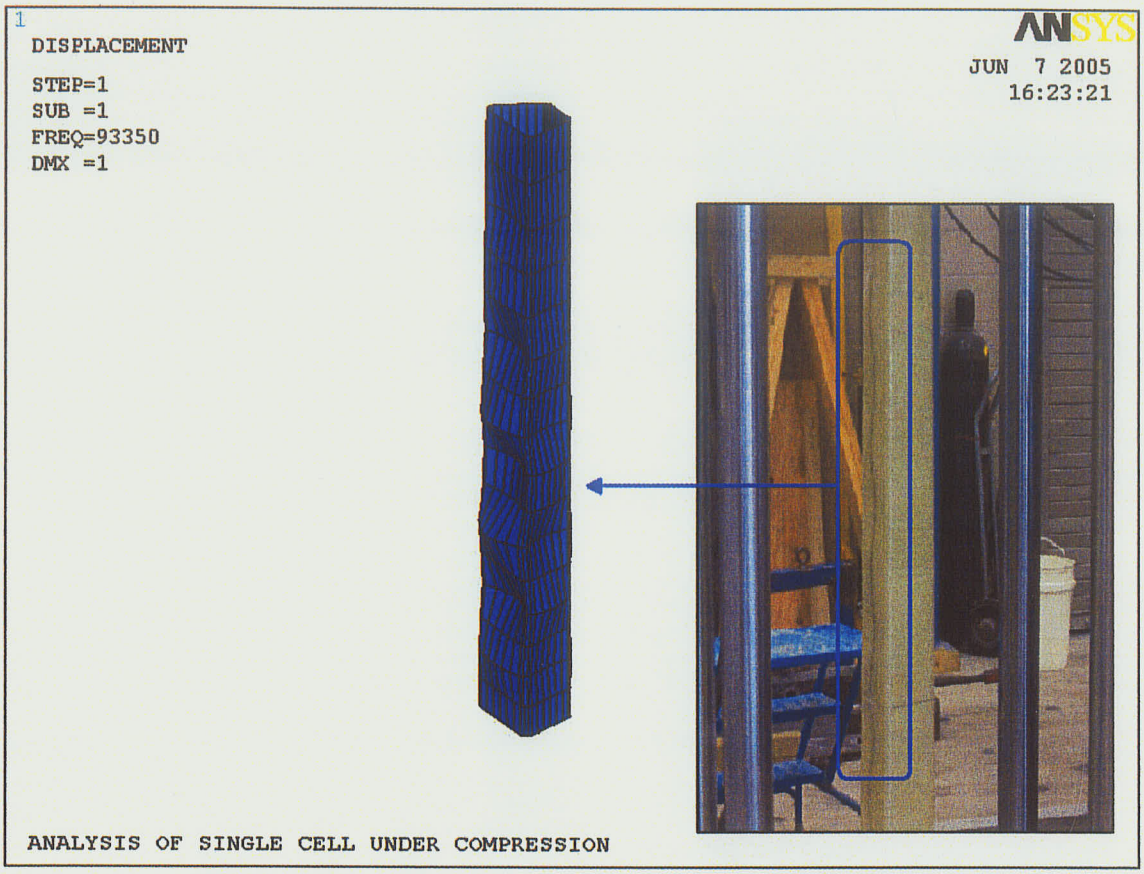

Figure 6-9 Deformed shape of specimen P2-1280-1

Table 6-2 Comparison between experimental and finite element results for Phase II specimens

Specimen	P_{exp} (kN)	$P_{F.E.M.}$ (kN)	$P_{exp}/P_{F.E.M.}$
P2-1280-1	82.89	93.35	0.888
P2-1780-2	64.38	72.03	0.894
Average	-	-	0.891

6.3.3 Modeling of Specimens in Phase III

In the case of the tower specimens tested in Phase III, the FRP tower was modeled into 3 parts: the top section, the joint section, and the bottom section, as illustrated in **Figure 6-10**. The thickness in the joint section was twice that of the top and bottom sections. The variation of element size was employed to provide a finer mesh in the area where the maximum stress and failure region were anticipated. A total of two thousand nine hundred and forty four elements were used to model the towers.

The base of the tower was assumed to be perfectly fixed and the section of the tower cells that were placed into the concrete inserts at the base was ignored in the analysis. Hence, all the degrees of freedom (u_x, u_y, u_z, rot_x, rot_y, and rot_z) were restrained at the end of the concrete inserts or at 330 mm from the base to simulate the fixed end condition. As shown in **Figure 6-11**, a lateral load was applied at nodes, 305 mm below the tip of the FRP tower in 500 N increments to a maximum load of 25,000 N, in order to obtain a load-time response of the model. The tower was modeled in the global coordinate system with the load being applied perpendicular to the x axis.

In this study, a geometric nonlinear analysis was used to account for the cross-section deformation and the large deflections. The wavefront procedure was

used in the ANSYS program to solve the system of simultaneous linear equations developed by the finite element model.

To determine the ultimate capacity of the towers, the load step was specified. The load step was automatically divided into unequal substeps whose range depended on the behavior of the FRP tower analyzed from previous substep. The ANSYS program adjusts the stiffness matrix to reflect the nonlinear changes in the FRP tower stiffness at the end of each substep. The breaking strength is determined according to the Tsai-Wu failure criterion, unless divergence occurred before reaching the failure criterion. Divergence of the solution indicates the occurrence of local buckling failure within the specimen.

The ANSYS input file for Phase III specimen model is given in **Appendix C** of this thesis. This input can be easily modified to handle different configurations of FRP towers.

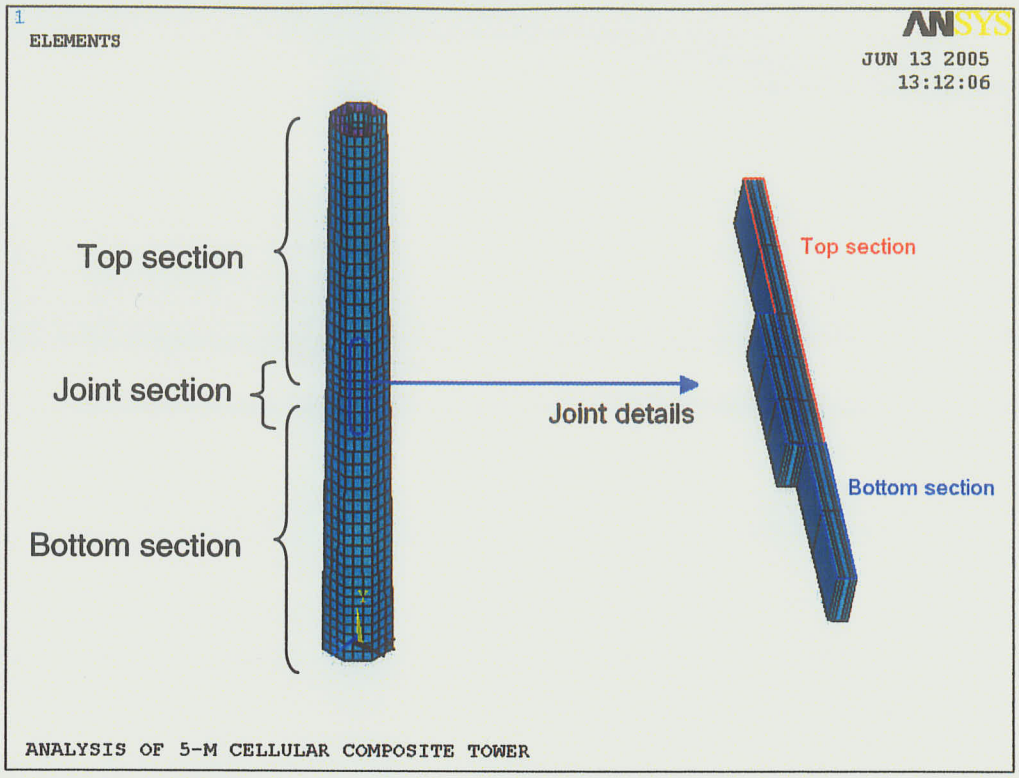

Figure 6-10 Joint details of Phase III specimen

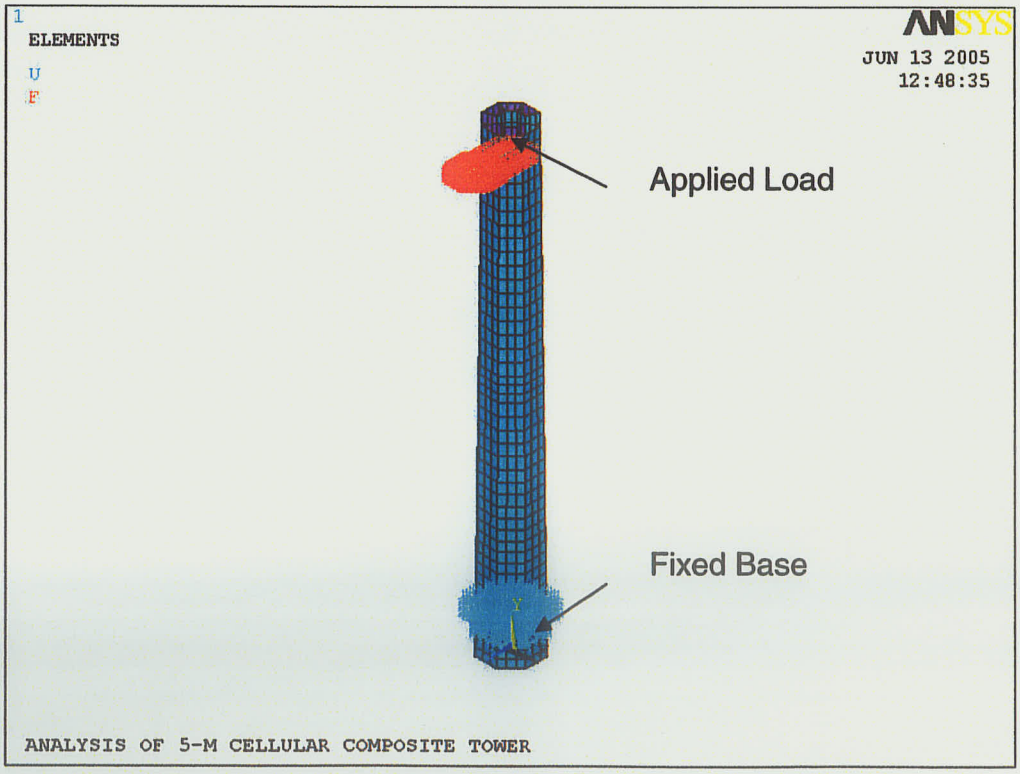

Figure 6-11 ANSYS FEM model of Phase III specimen

The eight-cell jointed FRP towers tested in Phase III were modeled using the finite element model described above. The load-tip deflection curve obtained from the finite element model is shown along with the experimental results in **Figure 6-12.** It should be noted that specimen P3-1R, the repaired P3-1 specimen, is not included in this comparison since it had been damaged before repairing it.

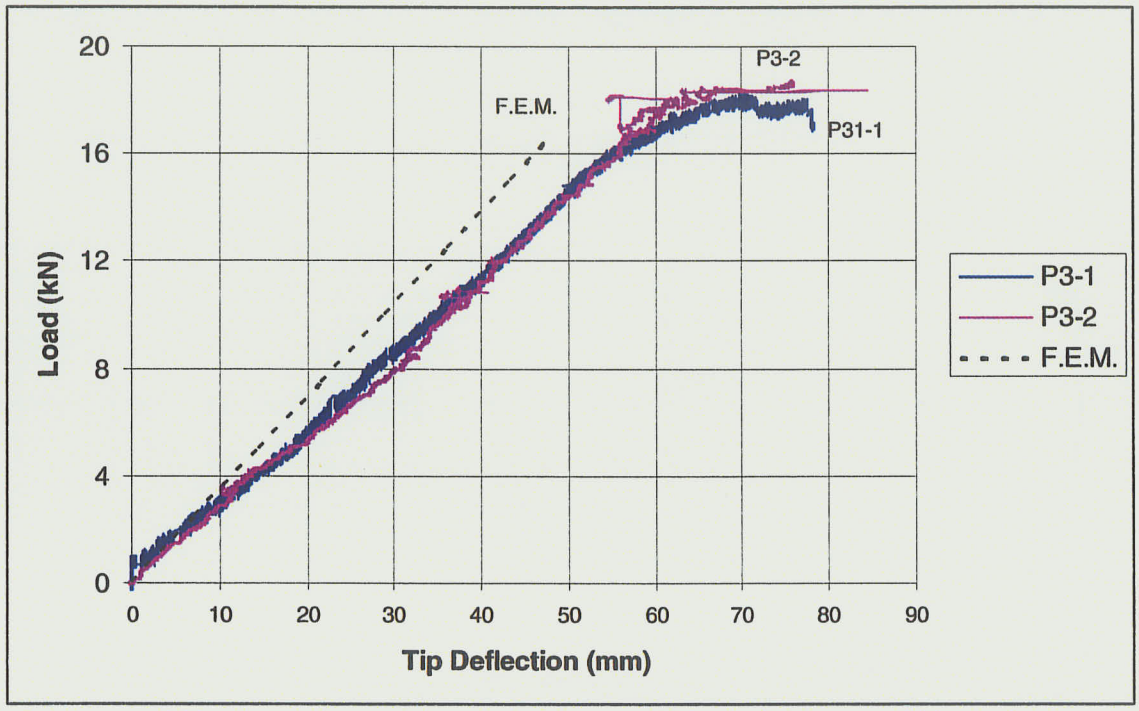

Figure 6-12 Load-tip deflection diagram comparison for Phase III specimens

The results shown in **Figure 6-12** indicate that the finite element model provides a good prediction of the structural behavior of the FRP towers tested in Phase III. In addition, the results also indicate that the FRP towers analyzed by the finite element method were approximately 20 percent stiffer than the actual tested FRP

towers. The load-tip deflection behavior predicted by the finite element model is linear relationship whereas the towers tested exhibited a linear behavior up to approximately 84 percent of the ultimate load. For loads greater than 84 percent of ultimate load, the behavior was nonlinear. This can be attributed to the damage accumulation and progressive failure on the micro scale of the tested specimens.

A comparison between the experimental ultimate load and the ultimate load predicted by the finite element model for the tower is given in **Table 6-3**. The ratios between the ultimate loads obtained from experimental program and the ultimate load predicted by the finite element method were 1.13 and 1.17. The average ratio was 1.15. This indicates that there is a good correlation between the failure load predicted by the finite element model and the experimental results with the experimental results being about 15 percent higher than the predicted ultimate load.

Table 6-3 Comparison between experimental and finite element failure load for Phase III specimens

Specimen	P_{exp} (kN)	$P_{F.E.M.}$ (kN)	$P_{exp}/ P_{F.E.M.}$
P3-1	19.48	16.63	1.17
P3-2	18.74	16.63	1.13
Average	19.11	16.63	1.15

Figure 6-13 shows the deformed shape obtained from the finite element model for Phase III specimens. The distribution of Tsai-Wu failure criterion value along the specimen at the ultimate load is illustrated in **Figure 6-14**. As shown in **Figure 6-14**, the Tsai –Wu failure value is less than unity at the ultimate load. This indicates that the failure mode was due to instability (the local buckling failure) and not due to material failure. The Phase III specimens, indeed, failed by local buckling on the compression side near the base, as shown in **Figure 6-15**. **Figure 6-16** shows the Von Mises stress distribution along Phase III specimen. The maximum stress predicted by the finite element model was 44.62 MPa, which occurred near the base inside the failure zone.

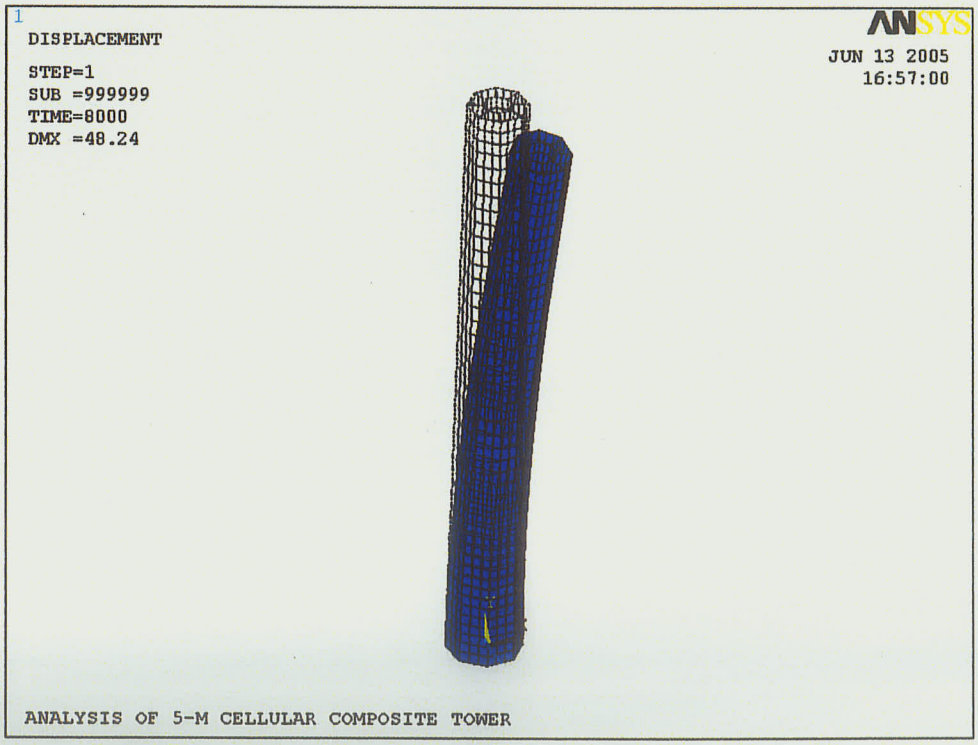

Figure 6-13 Deformed shape of Phase III specimens

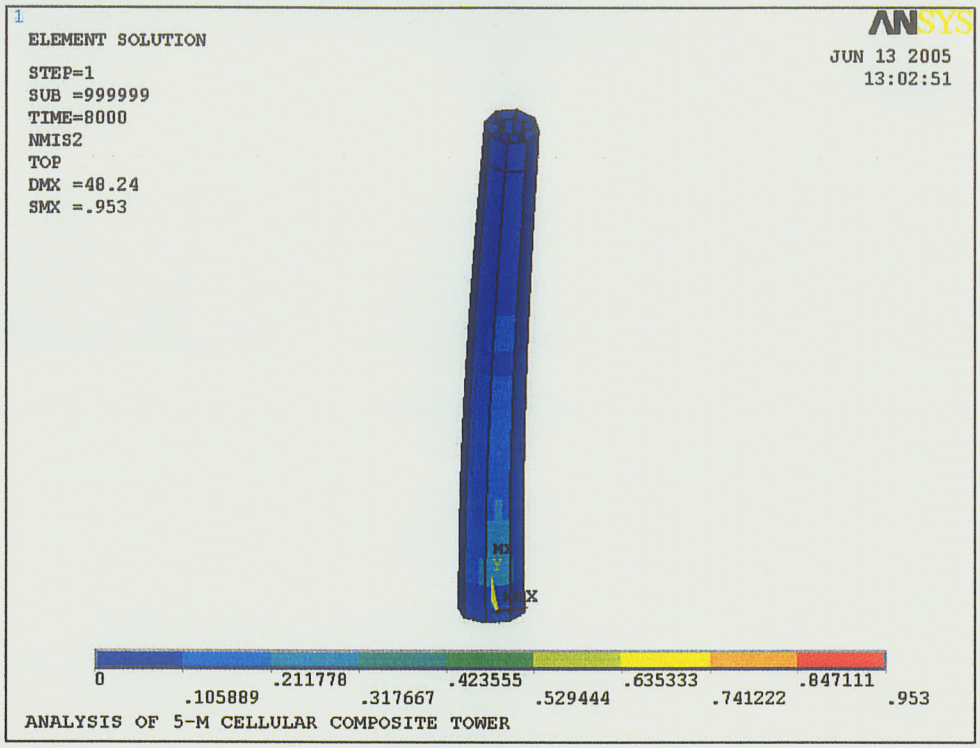

Figure 6-14 Distribution of Tsai-Wu failure criteria values for Phase III specimens

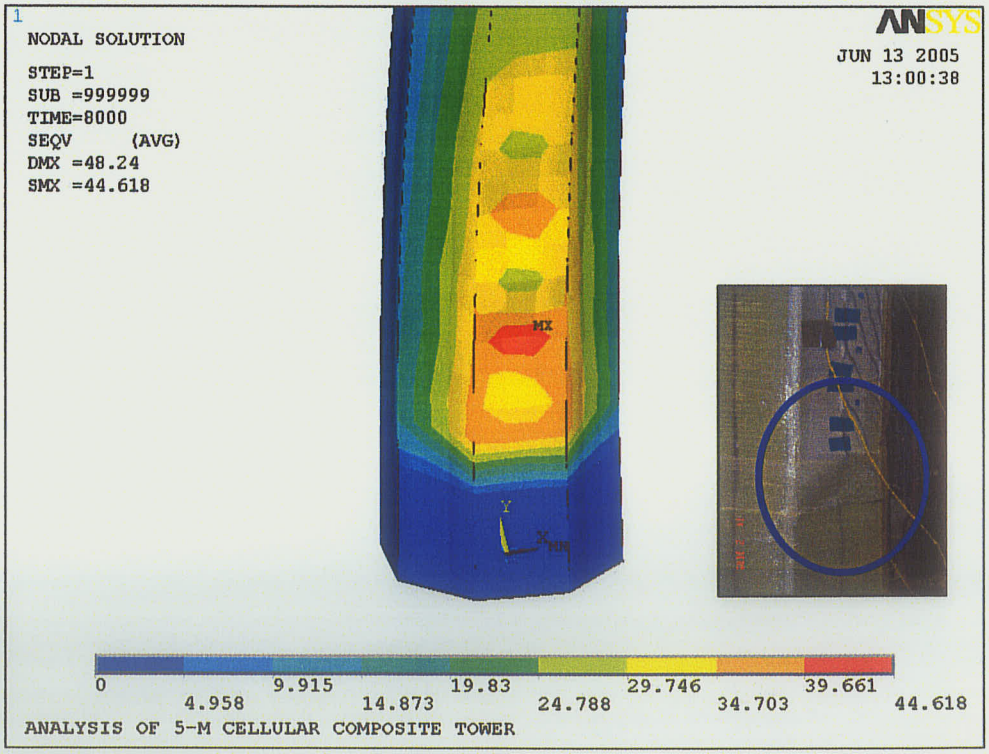

Figure 6-15 Local buckling of Phase III specimen

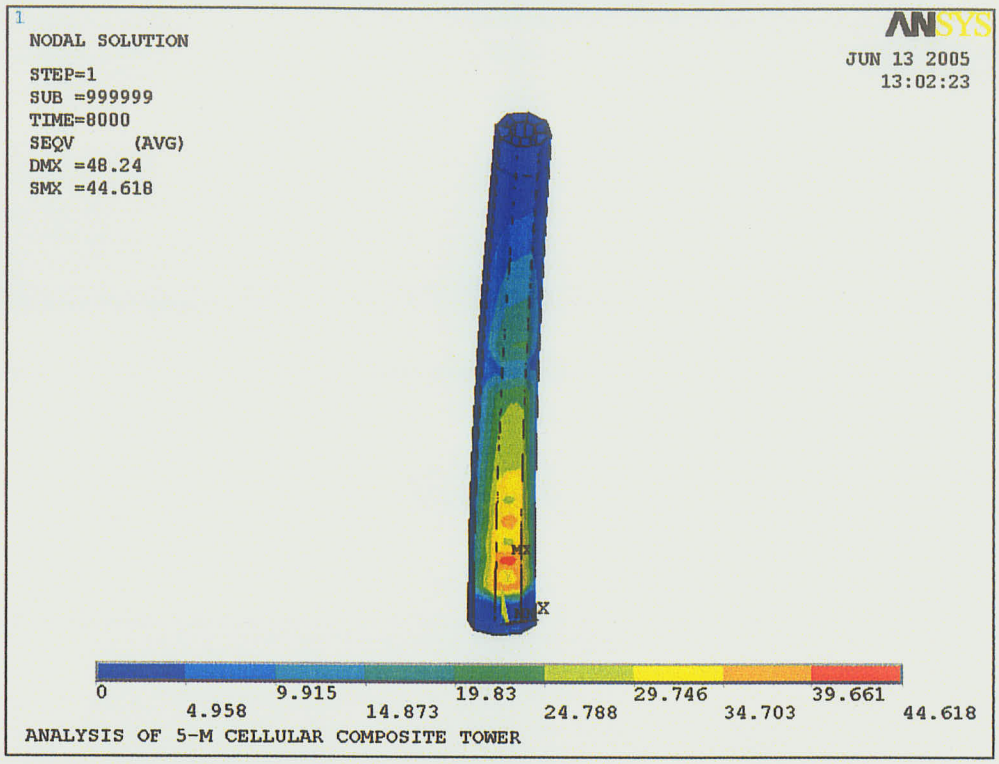

Figure 6-16 Stress distribution for Phase III specimens

In order to evaluate the finite element model further, the strains recorded in the experimental program were compared with the strains obtained through the finite element analysis. Longitudinal strains in both tension and compression side of the FRP tower were examined. The longitudinal strain distributions along FRP tower on both tension and compression side at failure load are shown in **Figure 6-17** and **6-18**, respectively.

According to the finite element model, the highest longitudinal tensile strain occurred at the end of concrete insert (near the base of the tower). The strains decrease toward the top of the tower. It should be noted that the shell thickness

in the joint section was twice that of the top and bottom sections. Hence, the longitudinal tensile strains at the joint area decrease in that region, as predicted by the finite element method. The tensile strains in the joint area obtained from experimental program compared well with the strains obtained from the finite element model. However, the experimental tensile strains near the base were higher than the strains obtained from the finite element model. This is due to fact that the cross-section distorts (ovalization) at that location giving rise to an increase in the tensile strains in that location.

A similar strain distribution pattern was found on the compression side of the tower. The compressive strains in the joint area obtained from experimental program compared well with the strains obtained from the finite element model, since there is less effect of ovalization. However, the compressive strains in the bottom section near the base obtained from experimental program fluctuated considerably from the theoretical values. This is due to the effect of both local buckling on the compression side and ovalization, which the finite element model does not take into consideration.

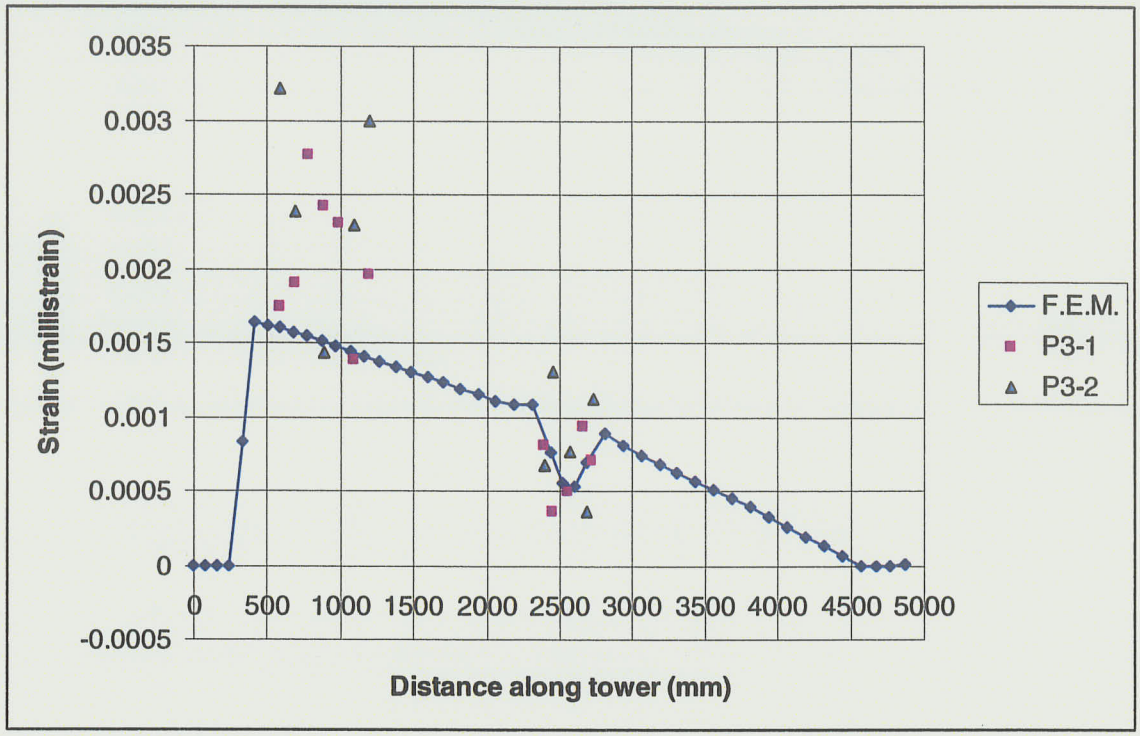

Figure 6-17 Longitudinal strain distribution along Phase III specimen on tension side at failure

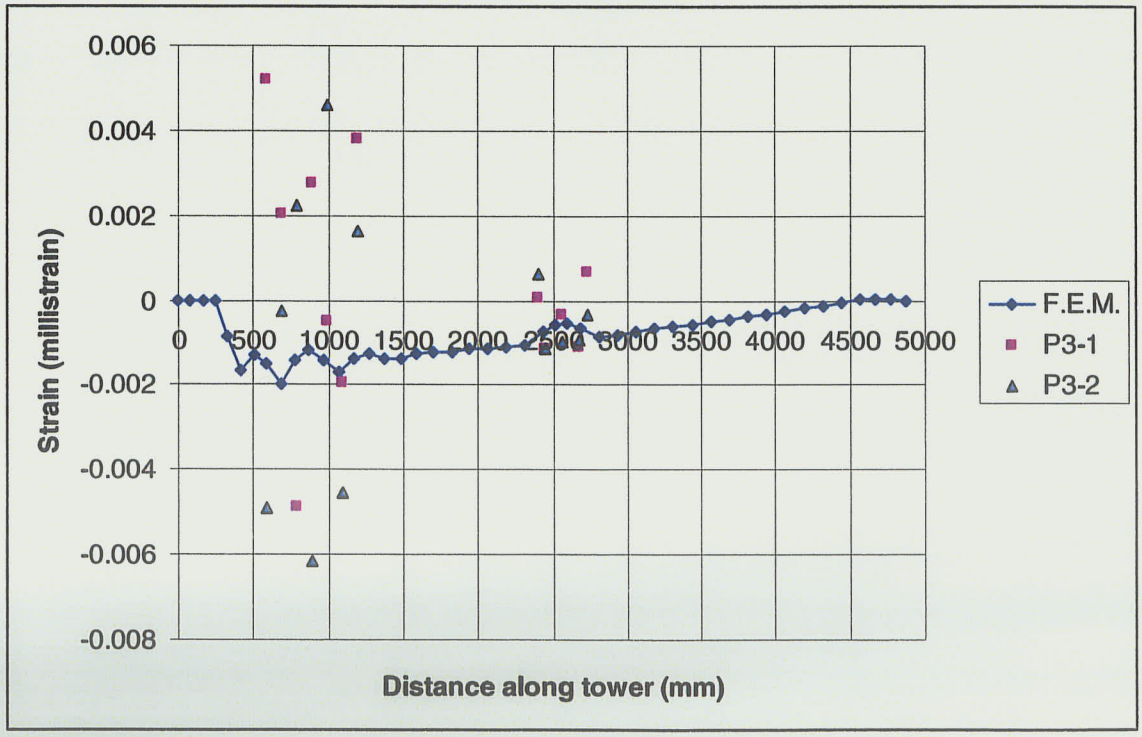

Figure 6-18 Longitudinal strain distribution along Phase III specimen on compression side at failure

CHAPTER 7

DESIGN OF WIND TURBINE TOWERS

7.1 GENERAL

In this chapter, the load requirements and the preliminary design of three 50 m wind turbine towers are discussed. Each tower was designed with different materials namely, steel, GFRP, and CFRP. The load requirements for the wind turbine towers were determined according to the Germanischer Lloyd: Rules and Regulations, Part 1 – Wind Energy (1993) and the National Building Code of Canada (1995). The steel, GFRP, and CFRP towers were designed to support a 750 kW wind turbine. The finite element analysis was used for designing the 750kW wind turbine towers. The ANSYS software program was used to develop the finite element model. The structural behavior of the composite towers was compared to the tubular steel tower and the results are discussed in this chapter.

7.2 DESIGN LOADS

There are two types of loads that need to be taken into account: loads acting on the tower and loads transferred from the wind turbine to the top of the tower. The wind turbine tower should be designed to resist these loads and their combination.

7.2.1 Load Acting on the Tower

The following loads were taken onto account in the design of the tower

- Dead load
- Live load due to snow, ice and rain
- Live load due to wind
- Live load due to earthquake

a) Dead load

Dead loads are computed on the basis of the unit weight of the materials. Dead loads consist of the particular self-weight of the shell, linings, ladders, and any permanent equipment.

b) Live load due to snow, ice and rain

Live loads are determined according to Nation Building Code of Canada (1995). The specific snow loading, S, due to snow accumulation on the structure shall be calculated from the formula:

$$S = S_s(C_b C_w C_s C_a) + S_r \qquad \textit{Equation 7.1}$$

where

S_s = the ground snow load

S_r = the associated rain load

C_b = the basic roof snow load factor

C_w = the wind exposure factor

C_s = the slope factor, and

C_a = the accumulation factor.

c) Live load due to wind

The wind turbine tower was designed for all loads and/or deflections caused by wind on the tower calculated in accordance to the National Building Code of Canada (1995). The force of the wind on a tower of circular cross-section is taken as the resultant horizontal pressure on its projected area considered as bands of uniform loading applied to the tower within height zones. A force shall

not be less than the design pressure specified by **Figure 7-1**. Total wind force acting on the tower is,

$$F = C_f q C_g C_e A \qquad \textit{Equation 7.2}$$

where

C_f = force coefficient $d\sqrt{qC_e} > 0.167$

q = $C\overline{V}^2$ is the reference wind pressure

C_g = the gust effect factor

C_e = the expose factor

A = the projected area of the tower

C = 650×10^{-6} for $\overline{V}$ in m/s

$\overline{V}$ = the reference wind speed.

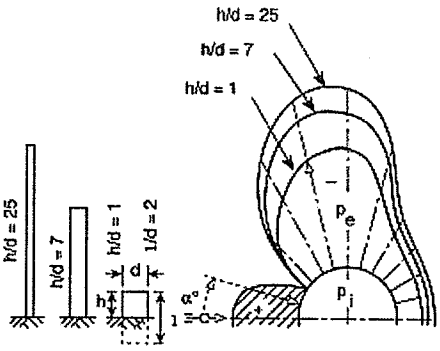

TOTAL FORCE $F = C_f \cdot q \cdot C_g \cdot C_e \cdot A$, where $A = d \cdot h$

C_f : FORCE COEFFICIENT FOR $d\sqrt{qC_e} > 0.167$

Slenderness h/d →	25	7	1
Cross section and roughness	C_f	C_f	C_f
Moderately smooth, (metal, timber, concrete)	0.7	0.6	0.5
Rough surface (rounded ribs h = 2%d)	0.9	0.8	0.7
Very rough surface (sharp ribs h = 8%d)	1.2	1.0	0.8
Smooth and rough surface sharp edges	1.4	1.2	1.0

C_p : EXTERNAL PRESS. COEFF. FOR $d\sqrt{qC_e} > 0.167$ and moderately smooth surface

h/d	l/d	α =	0°	15°	30°	45°	60°	75°	90°	105°	120°	135°	150°	165°	180°
25	50	C_p	+1.0	+0.8	+0.1	−0.9	−1.9	−2.5	−2.6	−1.9	−0.9	−0.7	−0.6	−0.6	−0.6
7	14	C_p	+1.0	+0.8	+0.1	−0.8	−1.7	−1.6	−2.2	−1.7	−0.8	−0.6	−0.5	−0.5	−0.5
1	2	C_p	+1.0	+0.8	+0.1	−0.7	−1.2	−1.6	−1.7	−1.2	−0.7	−0.5	−0.4	−0.4	−0.4

$\Delta p = p_i - p_e$ $\quad p_i = C_{pi} \cdot q \cdot C_g \cdot C_e$ $\quad p_e = C_p \cdot q \cdot C_g \cdot C_e$ Stack fully operating $C_{pi} = +0.1$; Stack throttled $C_{pi} = -0.8$

Figure 7-1 Wind coefficients (NBCC, 1995)

d) Live load due to earthquake

The wind turbine towers were also designed to withstand the minimum lateral seismic forces. The minimum lateral seismic forces, V, were calculated from the formula:

$$V = \left(\frac{V_e}{R_f}\right)U \qquad \textit{Equation 7.3}$$

where

V_e = the equivalent lateral force at the base of the structure

R_f = force modification factor

U = 0.6.

7.2.2 Loads Transferred from the Wind Turbine to Tower

According to the Germanischer Lloyd: Rules and Regulations, Part 1 – Wind Energy (1993), wind turbine towers should be designed to resist not only the following load cases, but also their combinations when they exist:

- Dead loads (self-weight of the wind turbine)
- Normal operating loads
- Extreme operating loads
- Annual wind (10 minutes)
- Annual gust (5 seconds)

- 50-year wind (10 minutes)
- 50-year gust (5 seconds)
- Generator short circuit (blackout)
- Rotor eccentricity.

The coordinate system used in determining the loads is shown in **Figure 7-2** where XN is in the wind direction.

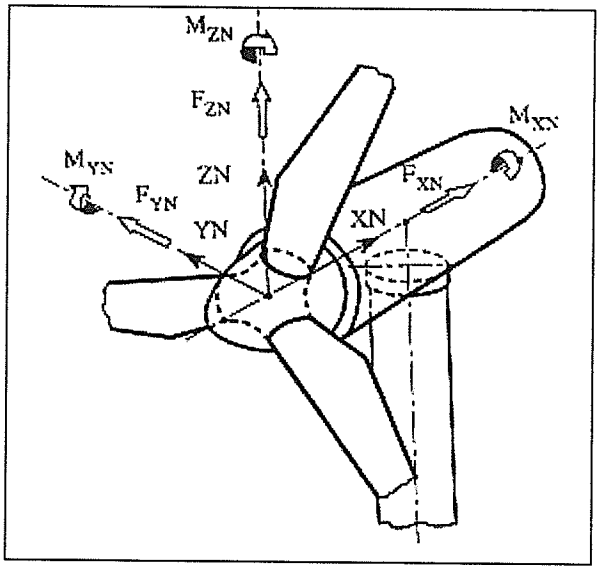

Figure 7-2 Wind turbine coordinate system (Germanischer Lloyd: Rules and Regulations, Part 1 – Wind Energy, 1993)

a) Dead loads

Dead load is due to the mechanical system stored at the top of the tower. There are three main weight components, which should be included in the calculations: the blades, the nacelle, and the rotor

The total axial load, F_z, is the result of combining the above weight components. There is also a mass eccentricity for the rotor that needs to be taken into account. This eccentricity is calculated by the following expression:

$$e_m = 0.05R \qquad \textit{Equation 7.4}$$

where, R is rotor radius. Because of the eccentricity, there is a moment, M_y, developed at the top of the tower.

b) Normal operating loads

During normal operation, a mean pressure, P_n, dependent on the rated wind speed, v_r, is used and shall be calculated from the formula:

$$P_n = C_{fb}\rho\frac{v_r^2}{2} \qquad \textit{Equation 7.5}$$

where,

C_{fb} = 8/9

ρ = the air density

v_r = the rated wind speed in m/s.

Thus, the force acting on the top of the tower is

$$F_x = P_n A \qquad \textbf{Equation 7.6}$$

where, A is the rotor swept area.

The eccentricity of the load that is developed during normal operation caused by turbulence, influence of oblique wind flow, and tower shadow is given by the formula:

$$e_w = \frac{wR^2}{2v_r^2} \qquad \textbf{Equation 7.7}$$

where, w is an extreme wind gradient over the swept rotor area. This eccentricity of the applied force produces an additional moment, M_y.

During the operation of the wind turbine, the rotor rotates around its axis and causes the resisting moment. This moment is proportional to the electrical power output, P_{el}, and to the inverse of the rotational speed of the rotor, n, in rpm. More specifically it is given by the formula

$$M_x = 14\frac{P_{el}}{n} \qquad \textbf{Equation 7.8}$$

While the wind turbine is operating, if it necessary to stop the blades, a hydraulic breaking system is used. The breaking of the wind turbine creates an overturning moment at the top of the tower. This moment is assumed to be twice the value derived from ***Equation 7.8***.

c) Extreme operating loads

Loads due to extreme operation are treated like normal operating loads, but the wind speed is converted to extreme condition speed (gust wind speed, v_b) using the gust factor, k_b, where the gust factor is equal to 5/3. Therefore, the gust wind speed becomes,

$$v_b = k_b v_r \qquad \textit{Equation 7.9}$$

The gust wind speed needs to be compared to the cut-out speed of the wind turbine. The value, whichever is less, is used to determine the wind pressure acting on the swept area of the rotor. The wind pressure is determined by the following expression:

$$P_b = C_{fb}\rho\frac{v_b^2}{2} \qquad \textit{Equation 7.10}$$

Therefore, the horizontal force, F_x, acting on the top of the tower is calculated using ***Equation 7.6***.

Loads from oblique wind flow or wind gradients must also be taken into account since the wind can change in direction during operation. This force is characterized as a lateral wind impact and its magnitude can be calculated as,

$$F_y = \pm\frac{1}{\sqrt{2}}P_n A \qquad \textit{Equation 7.11}$$

This force acting on the rotor in the Y direction results in bending moments in the rotor shaft and retarding moments in the nacelle yaw gear.

Similarly to the normal operating condition, the moment caused by the electrical power generating is to be calculated using ***Equation 7.8.***

d) Annual wind (10 minutes)

The annual wind is the mean of wind averaged over 10 minutes with an exceeding probability of once a year. Annual wind speed is specified as 80 percent of the corresponding 50-year wind speed. Normally, wind data are collected at a reference height, h^*, (10 meters). In order to determine the wind pressure at hub height, h, the 10-minutue mean wind speed has to be adjusted to hub height as follows:

$$v(h) = v\left(\frac{h}{h^*}\right)^{\alpha} \qquad \textit{Equation 7.12}$$

where

v = the wind speed

h^* = the reference height

α = 0.16 for wind and 0.11 for gust.

If the annual wind speed at hub height is more than the cut-out speed for the wind turbine, the stagnation pressure, P_s, should be used. The stagnation pressure is given as:

$$P_s = \frac{v^2}{1600} \qquad \textit{Equation 7.13}$$

Therefore, the horizontal force, F_x, applied at the top of the tower is determined using ***Equation 7.6***, where the surface area of the vane is used.

The gust effect must be taken into account since it may deviate by an angle of up to $\pm 15^{\circ}$ from the wind direction. This results in a force acting on the rotor in the Y direction, which also creates bending moments in the rotor shaft and retarding moments, M_z, in the nacelle yaw gear.

e) Annual gust (5 seconds)

The annual gust is the maximum wind speed averaged over 5 seconds with an exceeding probability of once a year. The annual gust speed is specified as 80 percent of the corresponding 50-year gust speed. Similar to the annual wind (10 minutes) condition, the gust wind speed has to be adjusted to hub height by using ***Equation 7.12***. The wind pressure and the horizontal force, F_x, acting at the top of the tower are calculated in the same manner as in the annual wind (10 minutes) condition.

The lateral load, F_y, caused by the oblique wind flow or wind gradients need to be considered and is assumed to have the same magnitude as the horizontal force. This lateral force results in bending moments in the rotor shaft and retarding moments, M_z, in the nacelle yaw gear.

f) 50-year wind (10 minutes)

The 50-year wind is the mean of wind averaged over 10 minutes with an exceeding probability of once in 50 years. Similar to annual wind (10 minutes) condition, the 50-year wind has to be adjusted to hub height using ***Equation 7.12***. The loads in this case are determined in the same manner as those in annual wind (10 minutes) condition.

g) 50-year gust (5 seconds)

The 50-year gust is the maximum wind speed averaged over 5 seconds with an exceeding probability of once in 50 years. Similar to annual gust (5 seconds) condition, the 50-year gust has to be adjusted to hub height using ***Equation 7.12***. The loads in this case are determined in the same process as those in annual gust (5 seconds) condition.

h) Generator short circuit (blackout)

In the event of a short circuit in the generator or the connection cables, peaks in torque may occur. If the generator short circuit moment is unknown, eight times the moment caused by the electrical power generating shall be assumed for synchronous generators (Germanischer Lloyd: Rules and Regulations, Part 1 – Wind Energy, 1993).

i) Rotor blade eccentricity

During the installation of blades on the rotor/nacelle, the actual tolerance is to be taken into account. If this is not known, the following eccentricity applies:

$$e_r = 0.005R \qquad \textit{Equation 7.14}$$

The horizontal force acting at the top of the tower is determined by the formula

$$F_x = me_r\Omega^2 \qquad \textit{Equation 7.15}$$

where

m = the mass of the rotor blades

Ω = the angular velocity of the rotor.

7.2.3 Load Combinations

The combinations of the above load cases are given in the **Table 7-1**.

Table 7-1 Load combinations

Load combinations / Load cases	1	2	3	4	5	6
Dead load	x	x	x	x	x	x
Normal operating load	x					
Extreme operating load		x				
Annual wind (10 min)			x			
Annual gust (5 sec)				x		
50-year wind (10 min)					x	
50-year gust (5 sec)						x
Blackout			x		x	
Rotor eccentricity	x	x				
Earthquake	x					

As shown in the **Table 7-1**, there are six possible load combinations.
The first load combination is referred to as a normal operating condition, which combines dead loads, loads due to normal operation, loads due to eccentricity caused during installation of the rotor, and the earthquake loads.

The second load combination is referred to as an extreme operating condition and does not combine the loads due to earthquake. Under this condition, the wind turbine works under a wind speed very close to the cut-out speed.

The third load combination is referred to as an operating condition under annual wind over a period of 10 minutes. In this scenario, forces caused by a generator short circuit (blackout) are included.

The fourth load combination is referred to as an operating condition under annual gust over a period of 5 seconds. Since the wind frequency is very small, it is extremely rare to combine it with other load cases caused by fault condition.

The fifth load combination is referred to as an operation condition under 50-year wind over a period of 10 minutes. Similarly to the third load combination, loads due to blackout are included.

The last load combination is referred to as an operating condition under 50-year gust over a period of 5 seconds. Similarly to the fourth load combination, other loads due to fault condition are not included.

In order to form the load combinations, the appropriate load factors, which are given in **Table 7-2**, are applied to the various loads components according to the load case group (Germanischer Lloyd: Rules and Regulations, Part 1 – Wind Energy, 1993).

Table 7-2 Safety factors for loads

Load cases	Load factors
Dead load	1.10
Normal operating load	1.20
Extreme operating load	1.20
Annual wind (10 min)	1.50
Annual gust (5 sec)	1.50
50-year wind (10 min)	1.00
50-year gust (5 sec)	1.00
Blackout	1.00
Rotor eccentricity	1.35
Earthquake	1.00

7.3 DESIGN OF 750 KW WIND TURBINE TOWERS

7.3.1 General Information

The technical data of a 750 kW wind turbine (NM48/750) are listed in **Tables 7-3** and **7-4**. This technical information was provided by NEG Micon (2002). For this example, it was assumed that the wind turbine tower is located in Churchill, Manitoba, Canada. Three types of towers were designed to support the 750 kW wind turbine. The first tower was assumed to be made of steel while the other two towers were assumed to be made of advanced composite materials, namely glass fiber reinforced polymers (GFRP), and carbon fiber reinforced polymer (CFRP). The composite towers were comprised of eight cells. The towers analyzed in this example, shown in **Figure 7-3**, have the following characteristics parameters: a height of 50 m, a diameter at the base of 3.5 m, and a diameter at the top of 2.5 m. The composite towers have a constant inner diameter of 2 m.

Table 7-3 Wind turbine parameters

Parameter	Value
Nominal Power (kW)	750
Nominal wind speed (m/s)	16
Cut-in speed (m/s)	4
Cut-out speed (m/s)	25
Rotor speed (rpm)	22
Rotor diameter (m)	48.2
Rotor swept area (m^2)	1824
No of blades	3
Hub height (m)	50

Table 7-4 Wind turbine mass distribution

Component	Mass (kg)	Center of gravity (m)
Blade	3x3466	7.85 (from rotor center)
Hub	2997	-
Total rotor	13395	2.237 (upwind from tower center)
Machine frame	4850	0.75 (downwind from tower center)
Gearbox	4670	1.04
Generator	3450	3.50
Main shaft	2015	-1.00
Cover	600	1.50
Yaw bearing	562	0.00
Rest	2815	-
Total nacelle	19000	1.125

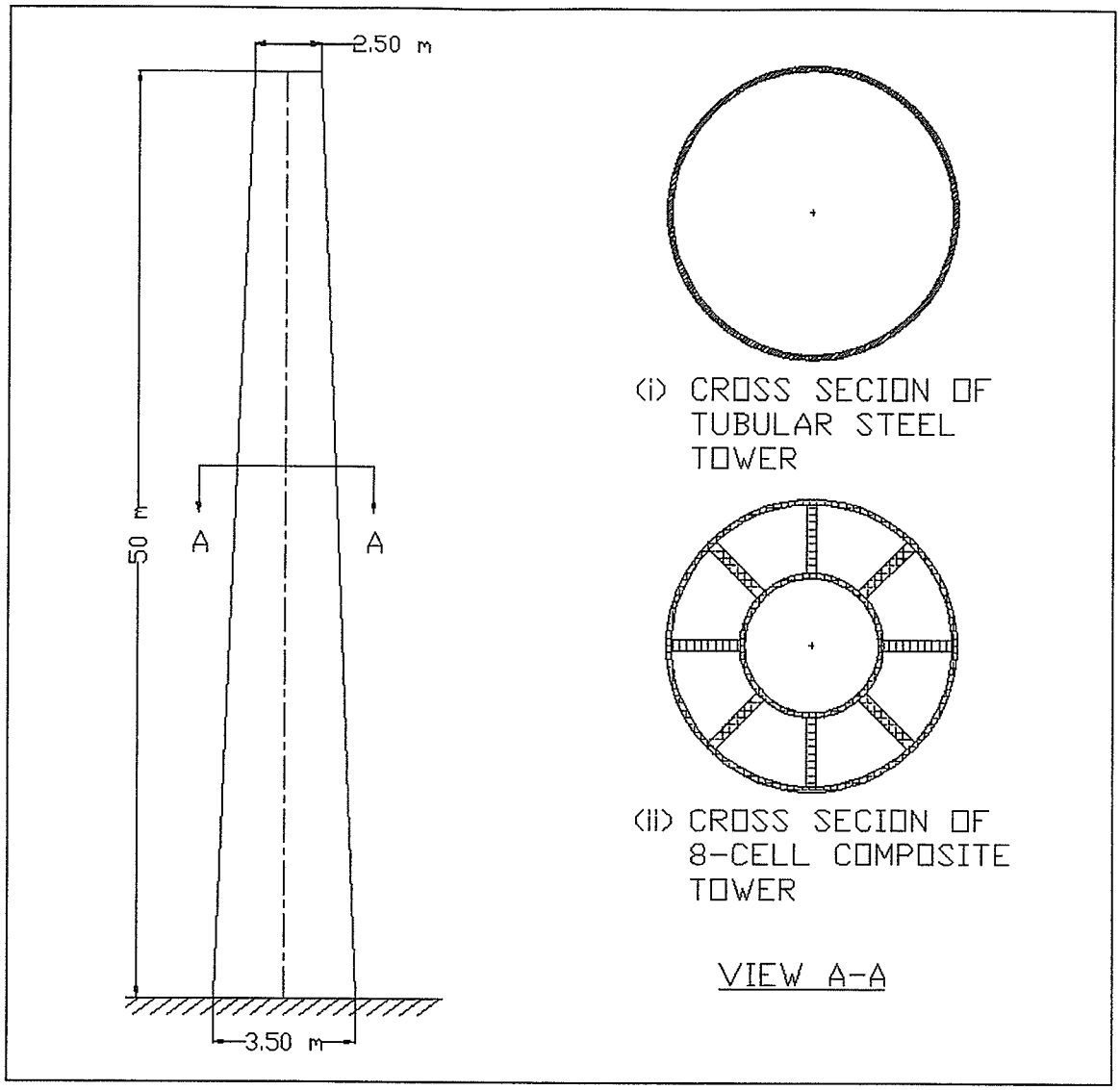

Figure 7-3 Tower dimensions

The Young's modulus for the steel tower material of 200,000 MPa and the yield strength of 350 MPa were assumed. For composite towers, the fiber volume ratio of 0.60 was assumed. The material elastic properties and the ultimate strength of GFRP and CFRP used are given in **Table 7-5**.

Table 7-5 Material elastic properties and the ultimate strength of GFRP and CFRP

Properties	GFRP (E-glass/epoxy)	CFRP (Carbon/epoxy)
V_f	0.60	0.60
Density (g/cm^3)	1.95	1.58
E_1 (GPa)	44.60	142
E_2 (GPa)	12.46	10.30
G_{12} (GPa)	4.85	7.20
ν_{12}	0.24	0.27
F_1^{tu} (MPa)	1300	2280
F_1^{cu} (MPa)	691	1440
F_2^{tu} (MPa)	47	57
F_2^{cu} (MPa)	130	228
F^{su} (MPa)	44	71

where, E_1 and E_2 are the elastic modulus in the fiber direction, transverse fiber direction, respectively; G_{12} is the shear modulus; F_1^{tu} and F_1^{cu} are the ultimate tensile and compressive strength in the fiber direction, respectively; F_2^{tu} and F_2^{cu} are the ultimate tensile and compressive strength in the transverse fiber direction, respectively; and F^{su} is the ultimate shear strength.

7.3.2 Loads on the Wind Turbine Tower

The typical distribution of wind pressure acting on the tower is shown in **Figure 7-4.** The summarized lateral wind pressure and factored lateral wind pressure, calculated according to the National Building Code of Canada (1995), as mentioned in previous section, are given in **Table 7-6.** The loads transferred from the wind turbine to the tower were determined according to the Germanischer Lloyd: Rules and Regulations, Part 1 – Wind Energy (1993) and the summarized factored loads and their combination are given in **Tables 7-7** and **7-8.**

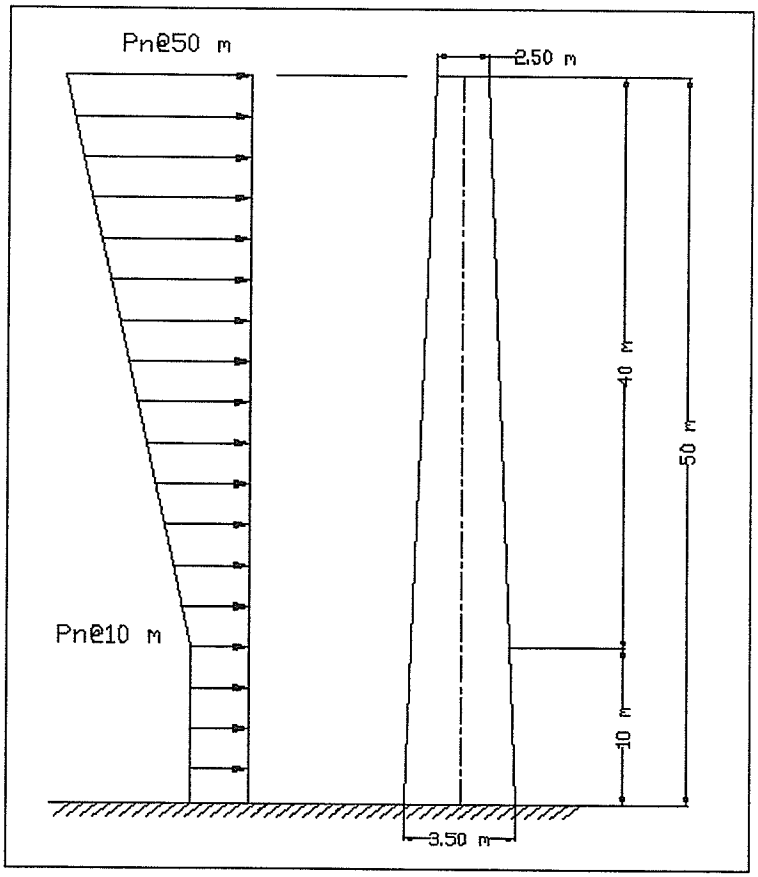

Figure 7-4 Distribution of wind pressure acting on the tower

Table 7-6 Wind pressure acting on the tower

Load combinations	Wind pressure (kN/m^2)		Factored wind pressure (kN/m^2)	
	0-10 m	50 m	0-10 m	50 m
1	0.22	0.26	0.35	0.42
2	0.53	0.64	0.84	1.01
3	0.53	0.80	0.84	1.26
4	1.05	1.58	1.65	2.48
5	0.85	0.85	1.33	1.33
6	1.65	1.65	2.59	2.59

Table 7-7 Summarized factored loads acting at the top of the tower

Load cases	Factored loads					
	F_x (kN)	F_y (kN)	F_z (kN)	M_x (kN-m)	M_y (kN-m)	M_z (kN-m)
Dead load	-	-	349.58	-	421.24	-
Normal operating load	311.28	-	-	1718.28	1412.46	-
Extreme operating load	760.00	-	-	572.79	-	1202.16
Annual wind (10 min)	126.65	-	-	-	-	75.39
Annual gust (5 sec)	209.82	-	-	-	-	482.59
50-year wind (10 min)	131.06	-	-	-	-	78.02
50-year gust (5 sec)	219.25	-	-	-	-	504.27
Blackout	-	-	-	3818.40	-	-
Rotor eccentricity	11.62	-	-	-	-	-

Table 7-8 Summarized load combinations

Load combinations	Factored loads					
	F_x (kN)	F_y (kN)	F_z (kN)	M_x (kN-m)	M_y (kN-m)	M_z (kN-m)
1	322.90	-	349.58	1718.28	2205.96	-
2	771.62	-	349.58	572.79	1289.31	1001.80
3	126.65	-	349.58	3818.40	563.72	50.26
4	209.82	-	349.58	-	657.29	321.73
5	131.06	-	349.58	3818.40	568.68	78.02
6	219.25	-	349.58	-	667.90	504.27

In **Table 7-8**, the additional moment due to eccentricity between the central of gravity of the nacelle and the tip of the tower of 1.125 meters have been added to the moment M_y. The additional moment is, therefore, equal to $M_y = 1.125F_x$.

The load combinations and wind pressures given in **Table 7-8** were used in the finite element analysis described below.

7.3.3 Finite Element Modeling

The finite element technique uses a finite number of elements whose displacement behavior is described by a fixed number of degrees of freedom to predict the structural behavior of structures. Modeling of the tubular steel and the composite wind turbine towers was carried out using the ANSYS finite element software and the theoretical model described earlier.

a) Modeling of the tubular steel wind turbine tower

To model the tubular steel wind turbine tower, an eight-node quadrilateral structural shell element was selected, as shown in **Figure 7-5**. This element is designated by ANSYS as SHELL93. The element is particularly well suited to model curved shells. The element has six degrees of freedom at each node: translations in the nodal x, y, and z directions and rotations about the nodal x, y, and z axes. The deformation shapes are quadratic in both in-plane directions. The element has plasticity, stress stiffening, large deflection, and large strain capabilities. The material properties used in the analysis are described in Section 7.3.1.

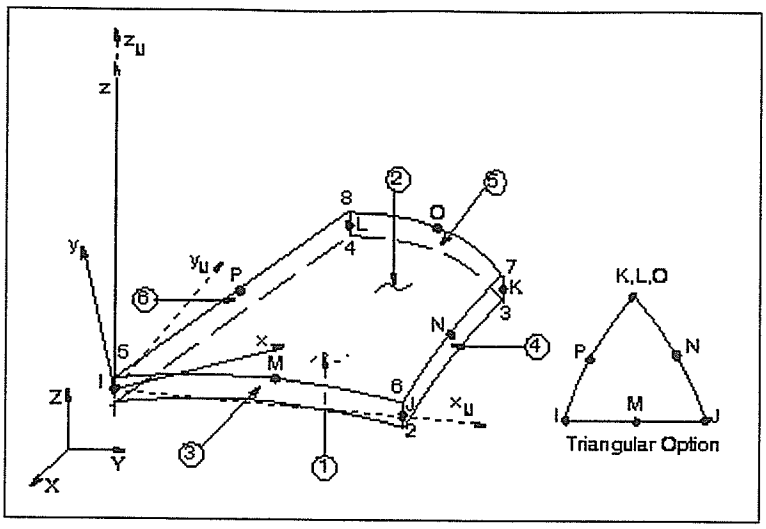

Figure 7-5 Eight-node quadrilateral structural shell element (ANSYS, 2002)

The discretization of the tubular steel tower is shown in **Figure 7-6.** The base of the tower is perfectly fixed. The loads, as described in section 7.3.2, were applied at the tip of the tower in 500 N increments to the maximum loads, in order to obtain a load-time response of the model. The tower needs to satisfy both the material strength and serviceability criteria. The ANSYS input file for the tubular steel wind turbine tower is given in **Appendix C.**

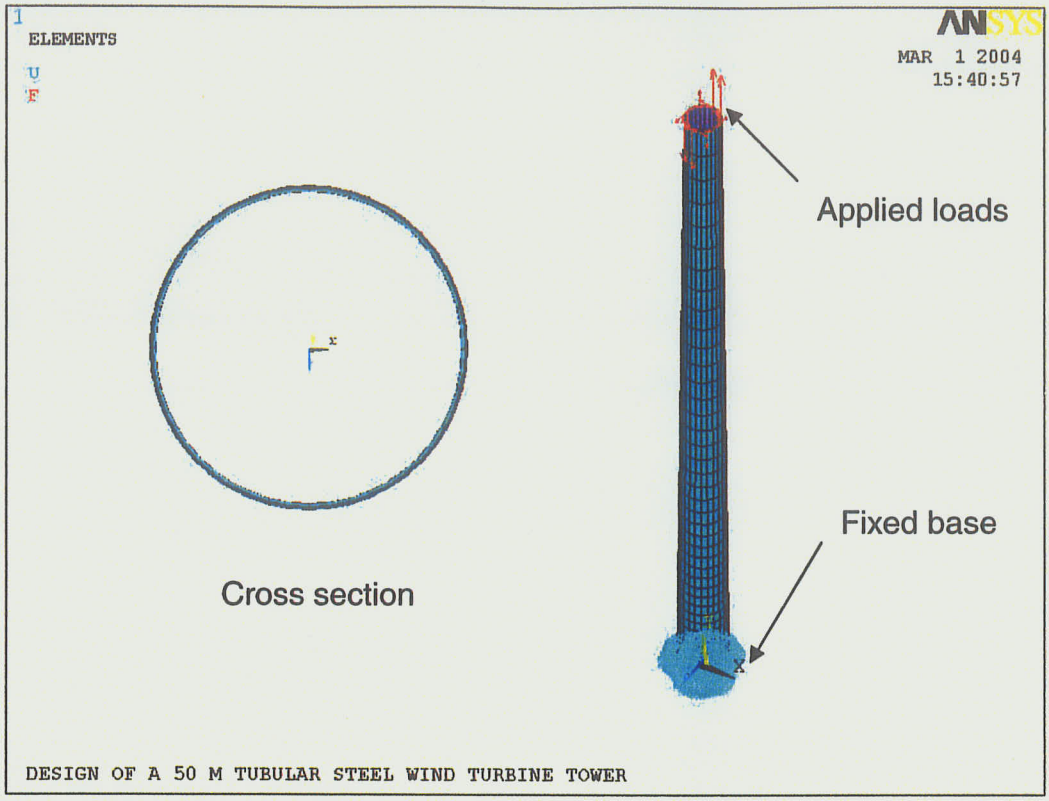

Figure 7-6 ANSYS model of tubular steel wind turbine tower

b) Modeling of the composite wind turbine towers

The geometry of both the GFRP and the CFRP wind turbine towers were built in ANSYS as shown in **Figure 7-7**. To model both the GFRP and the CFRP wind turbine towers, an eight-node quadrilateral layered shell element was selected as described in the previous chapter. This element is designated by ANSYS as SHELL99 and allowed the user to model up to 250 layers. The element has six degrees of freedom at each node: translations in the nodal x, y, and z directions and rotations about the nodal x, y, and z axes. This element was chosen mainly

because of its ability to be meshed over an area. Material properties for both the GFRP and the CFRP towers used in the analysis are described in Section 7.3.1.

As shown in **Figure 7-7**, the composite towers were modeled using eight-node layered shell elements and their dimensions were described in section 7.3.1. The base of the tower is perfectly fixed. The loads, as described in section 7.3.2, were applied at the tip of the tower in 500 N increments to the maximum loads, in order to obtain a load-time response of the model. Both towers were analyzed on the basis of material strength and serviceability criteria. The ANSYS input file for the CFRP wind turbine tower is given in **Appendix C**. A similar input file was used for the GRFP wind turbine tower.

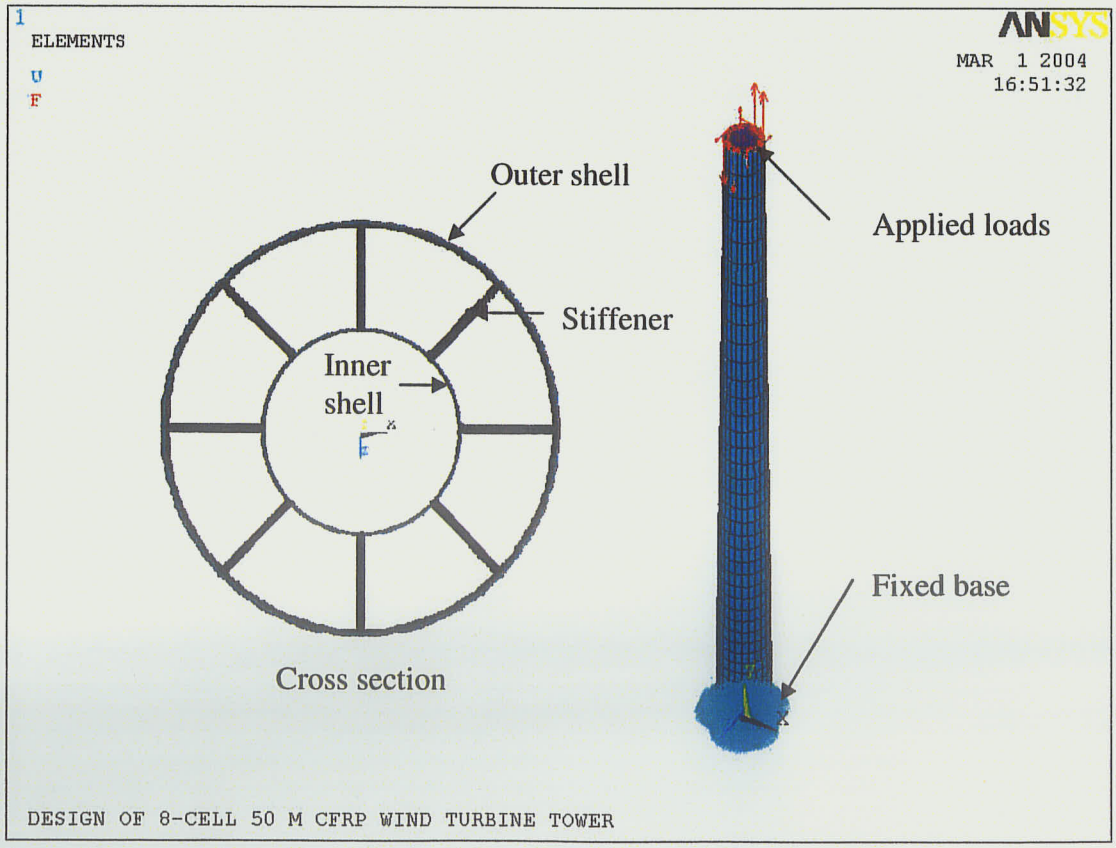

Figure 7-7 ANSYS model of CFRP wind turbine tower

7.3.4 Finite Element Results and Discussion

A summary of the analysis results from the finite element analysis of the 50 m tower supporting a 750 kW wind turbine is given in **Table 7-9**. The results include the tip deflection, the maximum stress, the failure criterion, and the total mass of the tower. In the analysis, the geometric non-linearity was taken into account since the large deflections were expected to occur in those towers.

Table 7-9 Summary of the analysis results of 750 kW tower wind turbine tower

Type of tower	Tip deflection (mm)	Maximum stress (MPa)	Tsai-Wu Criterion	Mass (kg)
Steel	560.45	219.01	-	85086.3
GFRP	967.25	69.59	0.39	78396.5
CFRP	627.74	150.94	0.18	47755.0

The analysis shows that a shell thickness of 23 mm is required for the tubular steel wind turbine tower, resulting in a total mass of 85.1 tons. The tip deflection of the steel tower is 560.45 mm, which is less than the serviceability limit for lateral deflection of 1 m. The serviceability limit for lateral deflection is defined as the distance between a rotor blade and a tower. The maximum stress of 219.01

MPa occurred near the base of the tower, as shown in **Figure 7-8**. This stress is less than the limit design strength of 315 MPa ($0.9F_y$).

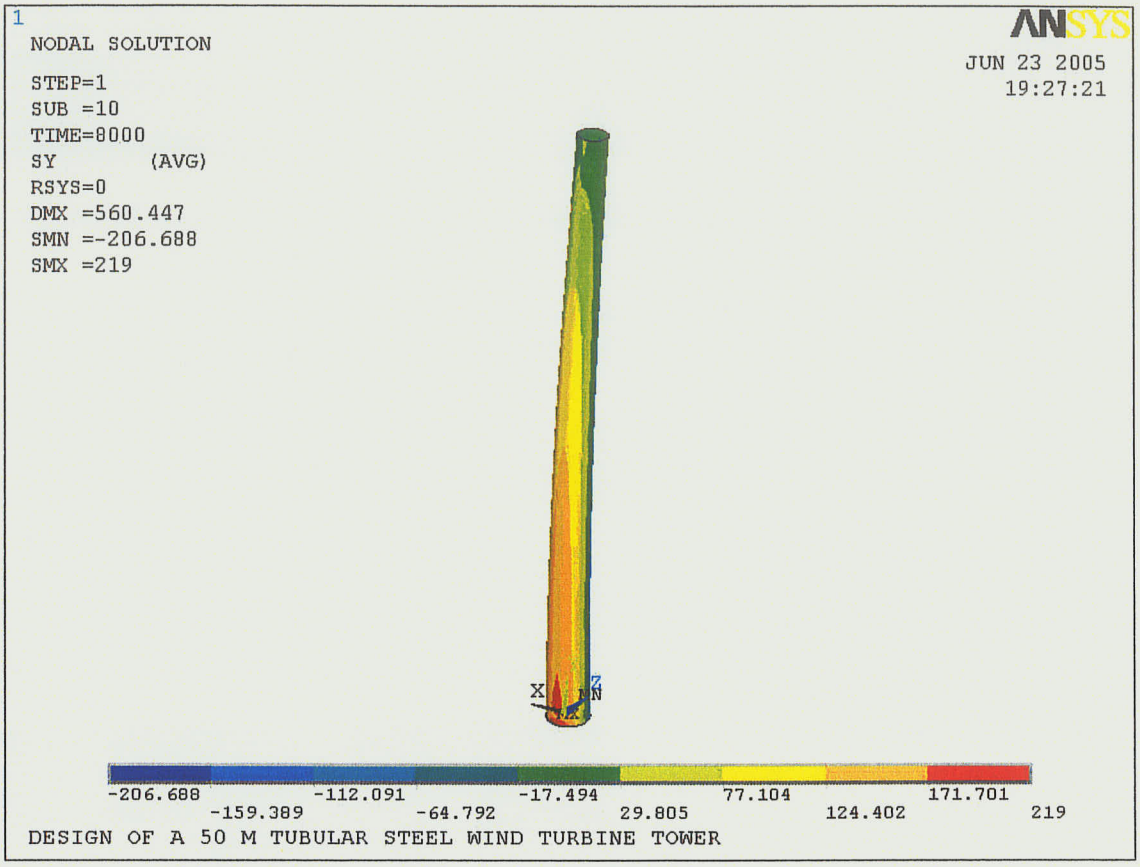

Figure 7-8 Distribution of stresses in tubular steel tower

For the 8-cell GFRP wind turbine tower, each cell was made up of 16 equal thickness layers of 1.25 mm. The fiber orientations were $(90, 0_6, 90)_2$. When individual cells were assembled to form a complete tower, 28 additional layers, with the following fiber orientation: $(0_{27}, 90)$, were added to make the tower stiffer and to provide confinement to the cells. The total mass of the GFRP tower was 78.4 tons. The tip deflection of the GFRP tower is 967.74 mm, which is less than

the serviceability limit for lateral deflection of 1 m. The maximum stress of 71.39 MPa occurred at the stiffener near the base of the tower as shown in **Figure 7-9**.

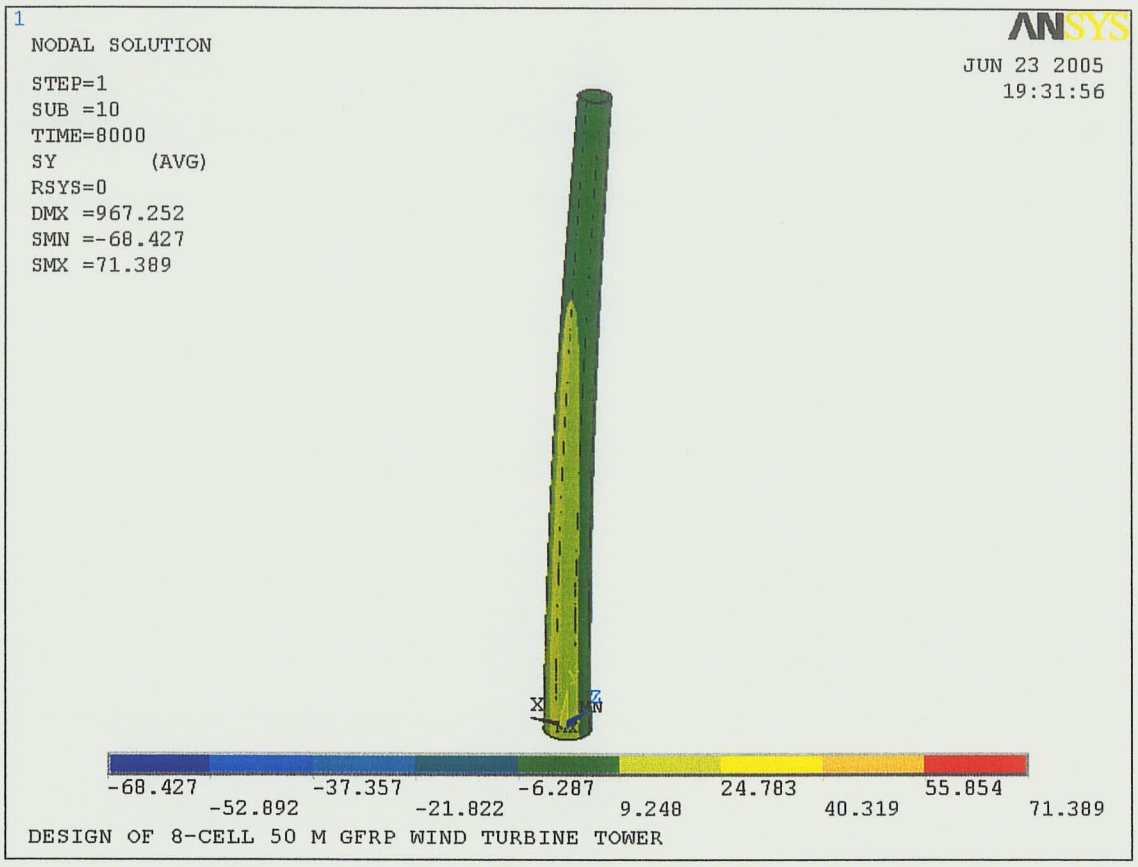

Figure 7-9 Distribution of stresses in 50 m GFRP tower

For the 8-cell CFRP wind turbine tower, each cell was made up of 20 equal thickness layers of 1.25 mm. The fiber orientations were $(90, 0_8, 90)_2$. When individual cells were assembled to form the complete tower, one additional circumferential layer was added to provide confinement. The total mass of the CFRP tower was 47.8 tons. The tip deflection of the CFRP tower is 627.74 mm, which is less than the serviceability limit for lateral deflection of 1 m. **Figure 7-10**

shows the stress distribution in the CFRP tower. The maximum stress of 152.29 MPa occurred at the stiffener near the base of the tower.

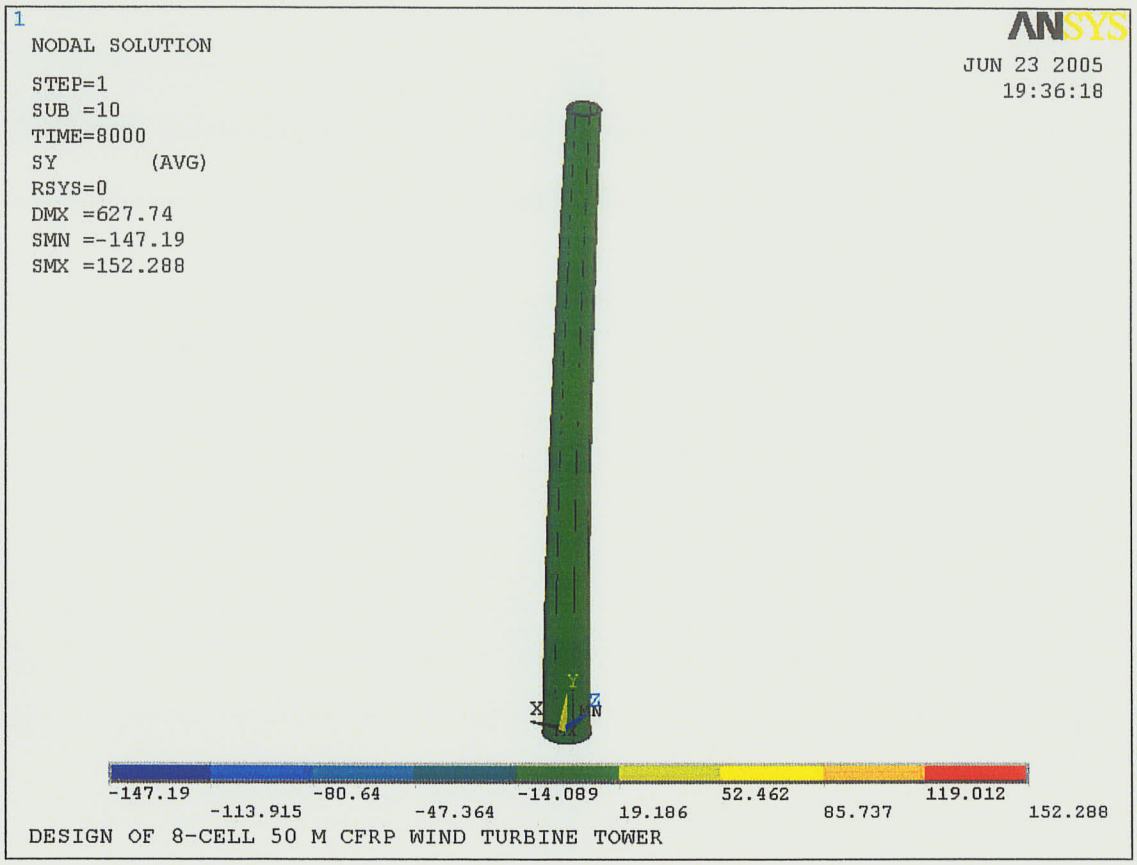

Figure 7-10 Distribution of stresses in 50 m CFRP tower

Figures 7-11, and **7-12** show values of the Tsai-Wu failure criterion along the GFRP and the CFRP tower and the failure criteria were 0.39 and 0.18, respectively. These values were less than unity, which indicated that both composite towers are safe to resist the factored loads. Although, both composite towers can resist a greater load, the serviceability limit for lateral deflection is the controlling factor in the design. The GFRP and the CFRP towers are approximately 8 and 44 percent lighter than the tubular steel tower respectively.

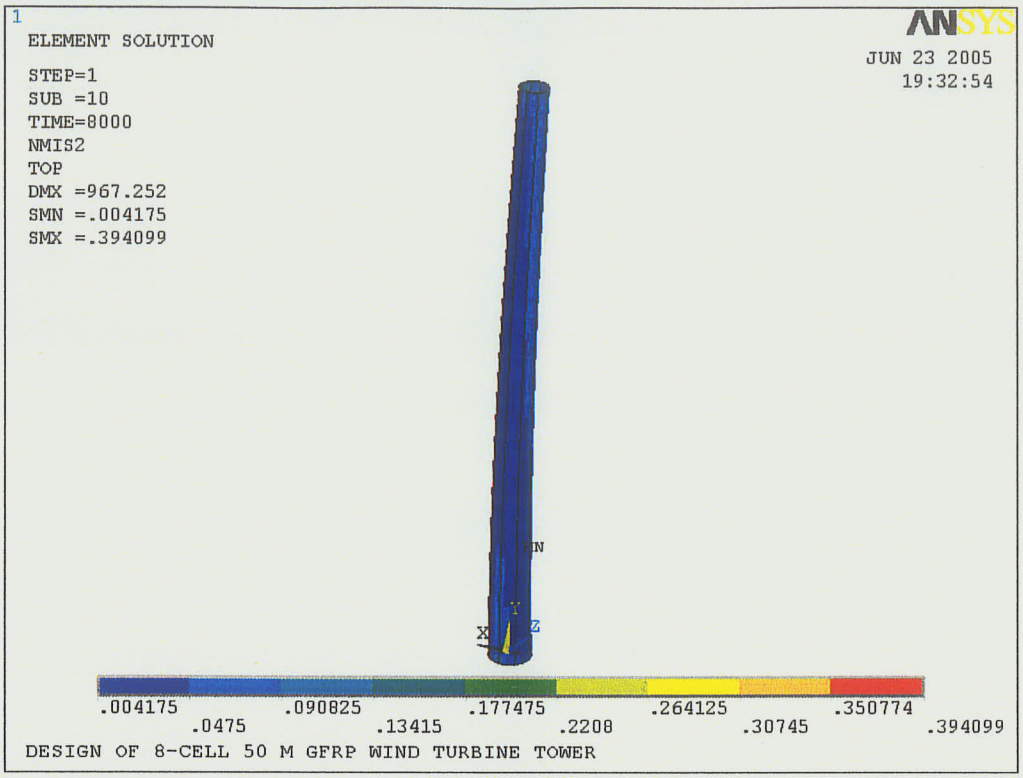

Figure 7-11 Values of the Tsai-Wu failure criterion along the 50 m GFRP tower

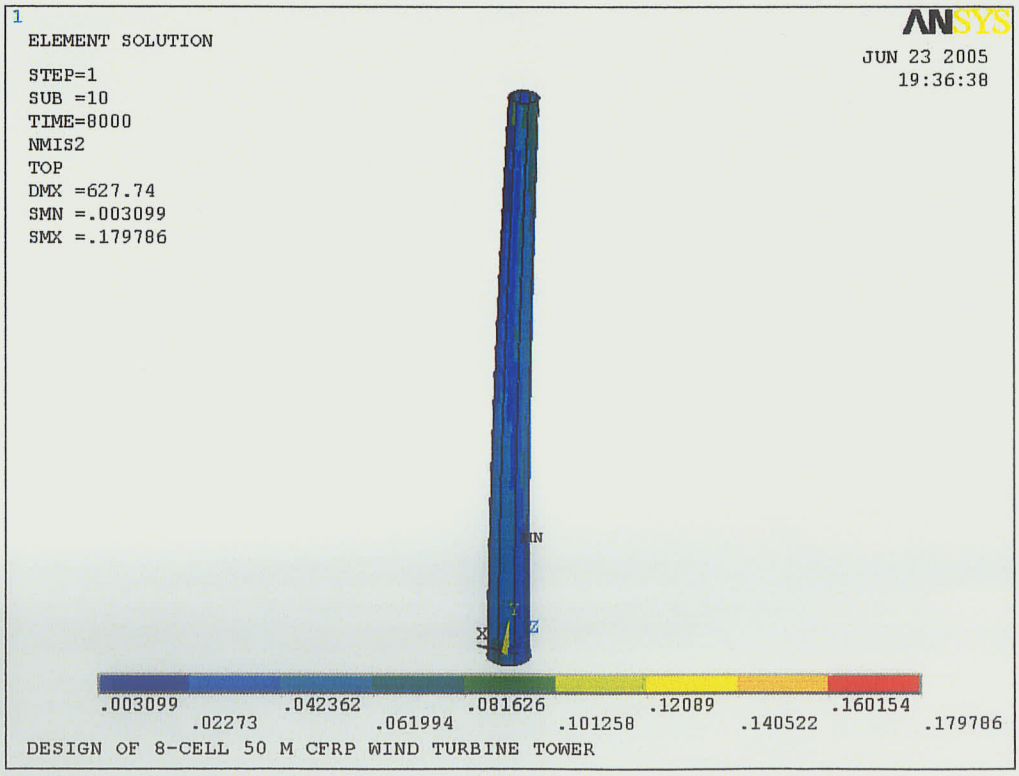

Figure 7-12 Values of the Tsai-Wu failure criterion along the 50 m CFRP tower

CHAPTER 8

SUMMARY, CONCLUSIONS AND RECOMMENDATIONS FOR FUTURE WORK

8.1 SUMMARY AND CONCLUSIONS

The multi-cell composite tower concept was proposed for use in wind turbine structures. The technology for manufacturing such towers was developed and presented in this thesis. This included the design and fabrication of a robotic filament winding machine that was used to fabricate the single and multi-cell composite segment and tower specimens in this research project. Experimental and theoretical studies were conducted to study the structural performance of the multi-cell composite wind turbine towers. The experimental program was carried out in three phases. In the first phase, two single cell specimens were tested to failure under lateral loading. The second phase involved the testing to failure of two single cell specimens in compression. The third phase of the experimental investigation involved the testing of two eight-cell jointed FRP towers. These specimens were tested as cantilevers under static loading. The towers were fabricated at the FRP Manufacturing Facility of the University of Manitoba using

the filament winding process. Glass fiber (1100 TEX) and West System 105/ 205 epoxy resin were used to wind all the tested specimens. The specimens were tested to failure and the experimental data collected included failure loads, tip deflections, and strains along the tower segment. In the theoretical component, the numerical method was used to analyze and simulate the behavior of the tested specimens. More specifically, the ANSYS finite element program was employed to develop a finite element model. Eight-node quadrilateral layered composite shell elements were used in this analysis. Large deflection and cross-section distortion were taken into account in the analysis and proper failure criteria were used. The theoretical models developed were then verified through comparison with the experimental results. The numerical results were in good correlation with the experimental results. Once the numerical models were verified, they were used as a design tool in the design of 750 kW 50 m wind turbine towers made of steel, GFRP, and CFRP.

Based on the results from both the experimental and the numerical studies, the following conclusions were drawn:

Phase I: Single cells under bending.

- The load-deflection relationship was linear up to the point of local buckling. A sudden drop in the load was observed after local buckling occurred.

- The average ultimate load carrying capacity and tip deflection of both specimens tested were 3.72 kN and 156.81 mm respectively. The variation in both ultimate load and stiffness was small.
- The failure mode was local buckling on the compression side near the fixed support. There was no other sign of failure, such as cracking or crushing of the resin or fiber during the tests at any part of the specimens.
- The finite element results were in a good agreement with the experimental results. The average ratio of the experimental-to-theoretical failure load was 0.92. The average tip deflection obtained from testing was 156.81 mm, which was slightly higher than 132.56 mm obtained from the finite element model. This is due to the imperfection of the boundary condition used. The failure mode predicted by the finite element model was also local buckling.

Phase II: Single cells under compression.

- The ultimate failure loads of the two cells tested were 82.89 kN and 64.38 kN, respectively.
- Specimens failed by local buckling. "Ripples" along the height on both specimens were observed prior to failure of the specimens.
- The finite element results had a strong correlation with the results obtained from the experimental program. The average ratio of the experimental-to-theoretical failure load was 0.891.

Phase III: Multi-cell towers under bending.

- The average ultimate load carrying capacity and tip deflection of the two towers tested (P3-1 and P3-2) were 19.11 kN and 76.90 mm, respectively. The test results showed a small variation in both ultimate load and stiffness.
- The load-deflection relationship was linear up to 84 percent of the ultimate load. At higher load levels a nonlinear behavior was observed due to the damage accumulation and progressive failure on a micro scale of the tested specimens.
- Two modes of failure were observed during the testing of towers. The first failure mode was a shear rapture of fibers on the compression side within the foundation. The second mode of failure was local buckling on the compression side near the fixed base.
- No other damage was observed at the connection between the upper and lower sections or between the individual cells, indicating that the bond strength was greater then the shear and bending strengths of the tower.
- The finite element model gave a good prediction on the structural behavior of the FRP towers tested in Phase III. The average ratio between the ultimate loads obtained from experimental program and the ultimate load predicted by the finite element method was 1.15. In addition, the results indicated that the FRP towers analyzed by the finite element method were

approximately 20 percent stiffer than the actual tested FRP towers due to the imperfection of the boundary condition used.

- Tsai –Wu failure criterion values obtained from the finite element model were less than unity at the ultimate load. This indicated that the failure mode was due to instability (local buckling) and not due to material failure. The Phase III specimens, indeed, failed by local buckling on the compression side near the base.
- The strains at the joint location obtained from experimental program were compared well with the strains obtained from the finite element model. However, the strains in the lower section near the base obtained from experimental program fluctuated considerably from the strains obtained from the finite element model. This was attributed to the effect of the "ripples" and ovalization in the section, which the finite element model does not take into consideration. The fact that the theoretical locations of the troupes and ridges in a buckling shape do not coincide with the actual location of the strain gages results in the discrepancies observed.
- An attempt to repair one of the towers and retest it was not as successful as expected. While the repaired tower was able to reach the ultimate capacity at the original tower, the deflections were too large.

Once the numerical models were verified, they were used as a design tool in the design of 750 kW 50 m wind turbine towers. Three materials were used in this

study: steel, GFRP, and CFRP. From this design study, the following conclusions were drawn:

- The serviceability limit for lateral deflection is the controlling factor in the design of FRP wind turbine towers.
- The GFRP and CFRP wind turbine towers were found to be approximately 8 and 44 percent, respectively, lighter than the tubular steel tower.
- The objective of example studied here was to examine the ability of the analytical model developed to analyze composite towers. No attempt was made to optimize the design. This is the objective of another study currently in progress at the University of Manitoba.

8.2 RECOMMENDATIONS FOR FUTURE RESEARCH

The research work for the development of multi-cell composite wind turbine towers at the University of Manitoba was the first of its kind. A number of major achievements were accomplished during this process and an application for patent of the developed concept has been filed. However, more research is still required in order to make this product economically attractive and to broaden the understanding of the behavior of multi-cell FRP towers. Further research is recommended in the following areas:

1. Investigation on a long term bonding performance in a variety of environmental conditions.

2. Evaluation of various connection designs, particularly the connection between the segments.
3. Investigation of scaled and full-scale segmented FRP towers under combined axial load and bending to evaluate both their structural performance and the performance of the bond between the segments.
4. Investigation of the segmented FRP towers under cyclic loading.
5. Investigation on the structural optimization of the segmented FRP towers.

A number of these areas are currently being investigated by colleagues at the University of Manitoba.

REFERENCES

1. Agarwal, B.D and Brownman, L.J., Analysis and Performance of Fiber Composites, 2nd Edition, John Wiley and Sons, Inc., 1990
2. Allen, L.R., Hutchinson, G.L., and Stevens, L.K., Buckling considerations in the design of elevated steel water tanks, Thin-walled structures, vol. 9, pp. 389-406, 1990
3. ANSYS, Rev 7.16.0, Reference Manual, ANSYS Inc., 2002
4. ASTM standards D3039, Standard Test Methods for Tensile Properties of Polymer Matrix Composite Materials, 2000
5. ASTM standards D3410, Standard Test Methods for Compressive Properties of Polymer Matrix Composite Materials with Unsupported Gage Section by Shear Loading, 2000
6. ASTM standards D5379, Standard Test Methods for Shear Properties of Composite Materials by the V-Notched Beam Method, 2000
7. Baker, E.H., Structural Analysis of Shells, McGraw-Hill book co., New York, 1972
8. Beedle, L.S., Stability of metal structures - A world view, Second edition, Structural stability council, Bethlehem, Pennsylvania, 1991
9. Borman, A. and Reuter, A., New Concepts and Optimal Design of Steel Towers for Large Horizontal Axis Wind turbines. Proceedings EUWEC'96, Gothenburg, 1996

10. Brughuis, F.J., Advanced Tower Solutions for Large Wind Turbines and Extreme Tower Heights, Mecal Applied Mechanics, Netherlands, website, http://www.mecal.nl, 2003

11. CAN/CSA-S16.1-94, Handbook of steel construction, Sixth edition, Canadian institute of steel construction, 1995

12. Chilver, A.H., Think-walled structures, Chatto and windus, London, 1967

13. Danish Wind Turbine Manufactures Association (DWTMA), Danish Wind Turbine Manufactures Association website, http://www.windpower.org/en/core.htm, 2005

14. Dean, W.R., Proc. Royal Society, London, Series A, Vol 107, pp.734, 1925

15. DIN 18800, Structural steelwork, German standards, Benth Veelag GmbH, Berlin, 1990

16. DMC-1425 User Manual, Galil Motion Control, Inc., 2002

17. Energy Efficient and Renewable Energy (EERE), Wind Energy, U.S. Department of Energy, website, http://www.eere.energy.gov

18. Englekirk, R., Steel Structures – Controlling Behavior Through Design, John Wiley & Sons, Inc., 1994

19. Gaylord, Jr. E.H., Gaylord, C.N., and Stallmeyer, J.E., Design of Steel Structures, 3rd Edition, McGraw-Hill, Inc., 1992

20. Germannischer Lloyd Rule and Regulations, Part 1: Wind Energy, Hamburg, German, 1993

21. Gipe, P, Wind Turbine Tower Trends, website, http://www.wind-works.org/articles/TowerTrends.html, 1995

22. Griffin, D.A., and Ashwill, T.D., Alternative Composite Materials for Magawatt-Scale Wind Turbine Blades: Design Considerations and recommended Testing, Proceedings of AIAA/ASME Wind Energy Symposium, 2003

23. IEC 61400-1 International Standard, Wind Turbine Generator Systems, Part 1: Safety Requirements, Geneva, Switzerland, 1999

24. Ibrahim, S., Performance Evaluation of Fiber Reinforced Plastics Poles for Transmission Lines, Ph.D. Thesis, University of Manitoba, Canada, 2000

25. Jones, J., Wind Onward and Upward, Renewable Energy World, Vol 7, No. 10, pp. 58-73, July-August 2004

26. Lin, Z.M., Analysis of Pole-Type Structures of Fiber Reinforced Plastics by Finite Element Method, Ph.D. Thesis, University of Manitoba, Canada, 1995

27. McClure, G., Boire, L., and Carrier, J.C., Applications of Communications Structures, Advanced Composite in Bridges and Structures, Canadian Society for Civil Engineering, Montreal, pp. 543-549, 1992

28. National Building Code of Canada, National Research Council of Canada, Canadian Structural Design Manual. Supplement No. 4, 1995

29. NEG Micon, Wind Turbine Properties of NM48/750, web page: www.neg-micon.com, 2002

30. Philopulos, S.D., An Investigation on Structural Performance of Jointed Filament Wound GFRP Poles for Light Utility Applications, Undergraduate Thesis, University of Manitoba, Canada, 2002

31. Polyzois, D., Ibrahim, S., and Raftoyiannis, I.G., Performance of Fiber-Reinforced Plastic Tapered Poles under Lateral Loading, Journal of Composite Materials, Vol 33, No. 10, pp. 941-960, 1999

32. Prescott, J., Applied Elasticity, Longmans, Green and Co., London, pp. 530-564, 1924

33. Salmon, C.G., and Johnson, J.E., Steel Structures – Design and Behavior, 3rd Edition, HarperCollingsPublishers Inc., 1990

34. Southwell, R.V., On the General Theory of Elastic Stability, Philos. Trans. Royal Soc., London, Series A, Vol 213, pp. 187-244, 1913

35. Troitsky, M.S., Tubular steel structures: theory and design, The Jame F. Lincoln Arc Welding Foundation, Cleveland, Ohio, 1986

36. Wilson, W.M., and Newmark, N.M., The Strength of Thin Cylindrical Shells as Column, Bulletin No. 255, University of Illinois, 1933

37. WindTower Composites, The Need for lightweight, Composite Towers, WindTower Composites website, http://windtowercomposites.com, 2003

APPENDIX A: DIMENSION DETAILS AND SPECIFICATIONS OF NEMA 34

The dimension details and specifications of NEMA 34 servo motor provided by Galil Motion Control, Inc. are shown below.

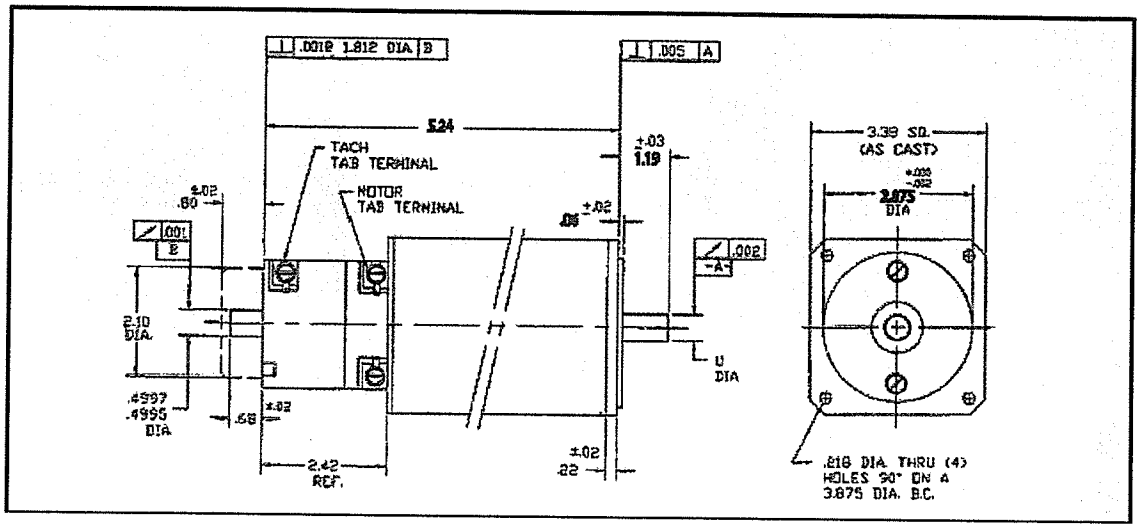

Figure A-1 NEMA 34 dimension details

Table A-1 NEMA 34 specifications

Parameter	Units	N34-170-1000
Kt–Torque Constant	Nm/A	0.197
Tc–Continuous Torque	Nm	1.2
Tp–Peak Torque	Nm	10.6
Jm–Moment of Inertia Recommended	Kg •m^2	$1.69x10^{-4}$
Supply Voltage	volts	100
ωm–Maximum	rpm	4600
R–Armature Resistance	W	1.01
L–Armature Inductance	mH	NA
Rth–Thermal Resistance	°C/W	2.3
Tm– Electro-mechanical Time Constant	ms	3.5
Length with Encoder	in	6.0
Diameter	in	3.38
Shaft Diameter	in	.375
Weight	kg	3.41
Encoder Resolution	cycles	1000

APPENDIX B: TERMINAL SPECIFICATIONS OF ICM-1460

Table B-1 Terminal specifications of ICM-1460

Terminal#	Label	I/O	Description
1	+12V	O	+12 Volts
2	-12V	O	-12 Volts
3	AMPEN	O	Amplifier enable (both X and Y axis)
4	ACMD	O	Analog motor command signal +/-10 Volts
5	PULSE	O	Pulse output for input to stepper motor amp
6	DIR	O	Direction output for input to stepper motor amp
7	GND		Signal Ground
8	RESET	I	Reset
9	ERROR	O	Error signal
10	OUT3	O	Output 3
11	OUT2	O	Output 2
12	OUT1	O	Output 1
13	CMP	O	Circular Compare output
14	5V	O	+ 5 Volts
15	GND		Signal Ground
16	IN7	I	I Input 7 (Y-axis index + input)
17	IN6	I	Input 6
18	IN5	I	Input 5
19	IN4	I	Input 4
20	IN3	I	Input 3
21	IN2	I	Input 2
22	IN1/LTCH	I	Input 1/Input for Latch Function)
23	FLS	I	Forward limit switch input
24	RLS	I	Reverse limit switch input
25	HOME	I	Home input
26	ABORT	I	Abort input
27	GND		Signal Ground
28	MA+	I	Main encoder A+
29	MA-	I	Main encoder A-
30	MB+	I	Main encoder B+
31	MB-	I	Main encoder B-
32	INDEX+	I	Main encoder index +
33	INDEX-	I	Main encoder index -
34	AA+	I	Auxiliary encoder A+
35	AA-	I	Auxiliary encoder A-
36	AB+	I	Auxiliary encoder B+
37	AB-	I	Auxiliary encoder B-
38	ACMD2	I	Analog command signal for Y axis
39	5V	O	+ 5 Volts
40	GND		Signal Ground

APPENDIX C: ANSYS INPUT FILES

C.1 INPUT FILE FOR PHASE I SPECIMEN

```
/PREP7
!*****************************************
!*SINGLE CELL UNDER LATERAL LOADING
!*Vf 55%
!*Fiber 1100TEX/EPOXY (WEST SYSTEM)
!*5 LAYERS FOR THE CELL(86,-86,0,86,-86)
!*****************************************
FZZ=5000 !N (5.0KN)
CV=25.4 !CONVERSION VALUE
T=0.177*CV/6 !1 LAYER OF UNI = 2 LAYERS OF FILA
/PBC,F,,1
/PBC,U,,1
/NERR,5,50000000
/PNUM,KP,1
/PNUM,LINE,1
/PNUM,AREA,1
/VIEW,1,3500,6000,5000
!
!GEOMETRY
!
K,1,0,0,0
K,2,0,96*CV,0
K,3,3.469*CV,0,0
K,4,3.469*CV,96*CV,0
K,5,-2.2782*CV,0,5.5*CV
K,6,-1.864*CV,96*CV,4.5*CV
K,7,5.7472*CV,0,5.5*CV
K,8,5.333*CV,96*CV,4.5*CV
A,1,2,4,3
A,3,4,8,7
A,7,8,6,5
A,5,6,2,1
BOPT,NUMB,OFF
AFILLT,2,1,0.5*CV
AFILLT,7,4,0.5*CV
AFILLT,5,3,0.5*CV
AFILLT,9,8,0.5*CV
AREVERSE,2,0
AREVERSE,5,0
AREVERSE,6,0
AREVERSE,7,0
```

```
!
ELEMENT TYPE
!
ET,1,SHELL99,,0,0,0,1,3
KEYOPT,1,8,1
KEYOPT,1,11,1
 !(NODE LOCATES AT THE BOTTOM)
!
!REAL CONSTANT
!
R,1,5,0 !SPECIMEN
RMORE,
RMORE,1,4,T,1,-4,T
RMORE,2,90,2*T,1,4,T
RMORE,1,-4,T
!
!MATERIAL PROPERTIES
!
!FILAMENT WINDING
!
MP,EX,1,23060 !N/MM^2 (MPA)
MP,EY,1,5420
MP,EZ,1,5420
MP,GXY,1,2090
MP,GYZ,1,2080
MP,GXZ,1,2090
MP,PRXY,1,0.31
MP,PRYZ,1,0.3
MP,PRXZ,1,0.31
MP,DENS,1,1.97E-6 !KG/MM^3
!
!UNIDIRECTIONAL SHEET
!
MP,EX,2,28490 !N/MM^2 (MPA)
MP,EY,2,9380
MP,EZ,2,9380
MP,GXY,2,2410
MP,GYZ,2,3600
MP,GXZ,2,2410
MP,PRXY,2,0.34
MP,PRYZ,2,0.3
MP,PRXZ,2,0.34
MP,DENS,2,1.97E-6 !KG/MM^3
!
!FAILURE CRITERIA
!
```

```
!CHECK MAX STRESS AND TSAI-WU FAILURE CRITERIA
TB,FAIL,1,1
TBTEMP,,CRIT
TBDATA,1,0,1,1
TBTEMP,0
TBDATA,10,632.62,-258.7,1000,-1000,1000,-1000
!(IGNORE STRESS IN Z DIRECTION)
TBDATA,16,1000,1000,1000,-1,-1,-1
!
TB,FAIL,2,1
TBTEMP,,CRIT
TBDATA,1,0,1,1
TBTEMP,0
TBDATA,10,579.13,-361.55,18.08,-65.95,1000,-1000
!(IGNORE STRESS IN Z DIRECTION)
TBDATA,16,47.03,47.03,47.03,-1,-1,-1
!
!MASHING CONTROL
!
ESHAPE,3,0
ESIZE,0,6
LSEL,S,LOC,Y,96*CV/2
LESIZE,ALL,,,50,5
LSEL,ALL
!
ASEL,S,AREA,,1,3,2
AATT,1,1,1
AMESH,ALL
ASEL,ALL
!
ASEL,S,AREA,,4,10,6
AATT,1,1,1
AMESH,ALL
ASEL,ALL
!
ESIZE,0,3
ASEL,S,AREA,,2
AATT,1,1,1
AMESH,ALL
ASEL,ALL
!
ASEL,S,AREA,,5,7,1
AATT,1,1,1
AMESH,ALL
ASEL,ALL
!
```

```
!BOUNDARY CONDITIONS
!
NSEL,S,LOC,Y,311,312
D,ALL,UZ,0,0,,,UX,UY,ROTX,ROTY,ROTZ
NSEL,ALL
!
SAVE
FINISH
!
!ANALYSIS
!
/SOLU
/TITLE, ANALYSIS OF SINGLE CELL UNDER LATERAL LOADING
ANTYPE,STATIC
NLGEOM,ON
AUTOTS,ON
SSTIF,ON
NSUBST,10,500,10,ON
NROPT,AUTO
NEQIT,20
CNVTOL,F,,0.001,,1
CNVTOL,M,,0.001,,1
CNVTOL,U,,0.04,,0
TIME,8000
!
!LOADS
!
NSEL,S,LOC,Y,2340,2341
F,ALL,FZ,-FZZ/72 ! 72 NODES
NSEL,ALL
OUTRES,,ALL
LSWRITE,1
LSSOLVE,1
SAVE
FINISH
```

C.2 INPUT FILE FOR PHASE II SPECIMEN

```
/PREP7
!*****************************************
!*SINGLE CELL UNDER COMPRESSION
!*Vf 55%
!*Fiber 1100TEX/EPOXY (WEST SYSTEM)
!*5 LAYERS FOR THE CELL(86,-86,0,86,-86)
!*****************************************
FYY=1 !N (1N)
CV=25.4 !CONVERSION VALUE
T=0.177*CV/6 !1 LAYER OF UNI = 2 LAYERS OF FILA
/PBC,F,,1
/PBC,U,,1
/NERR,5,50000000
/PNUM,KP,1
/PNUM,LINE,1
/PNUM,AREA,1
/VIEW,1,3500,6000,5000
!
!GEOMETRY
K,1,0,0,0
K,2,0,96*CV,0
K,3,3.469*CV,0,0
K,4,3.469*CV,96*CV,0
K,5,-2.2782*CV,0,5.5*CV
K,6,-1.864*CV,96*CV,4.5*CV
K,7,5.7472*CV,0,5.5*CV
K,8,5.333*CV,96*CV,4.5*CV
A,1,2,4,3
A,3,4,8,7
A,7,8,6,5
A,5,6,2,1
BOPT,NUMB,OFF
AFILLT,2,1,0.5*CV
AFILLT,7,4,0.5*CV
AFILLT,5,3,0.5*CV
AFILLT,9,8,0.5*CV
AREVERSE,2,0
AREVERSE,5,0
AREVERSE,6,0
AREVERSE,7,0
!
ELEMENT TYPE
ET,1,SHELL99,,0,0,0,1,3
```

```
KEYOPT,1,8,1
KEYOPT,1,11,1
!(NODE LOCATES AT THE BOTTOM)
!
!REAL CONSTANT
R,1,5,0 !SPECIMEN
RMORE,
RMORE,1,4,T,1,-4,T
RMORE,2,90,2*T,1,4,T
RMORE,1,-4,T
!
!MATERIAL PROPERTIES
!FILAMENT WINDING
MP,EX,1,23060 !N/MM^2 (MPA)
MP,EY,1,5420
MP,EZ,1,5420
MP,GXY,1,2090
MP,GYZ,1,2080
MP,GXZ,1,2090
MP,PRXY,1,0.31
MP,PRYZ,1,0.3
MP,PRXZ,1,0.31
MP,DENS,1,1.97E-6 !KG/MM^3
!
!UNIDIRECTIONAL SHEET
MP,EX,2,28490 !N/MM^2 (MPA)
MP,EY,2,9380
MP,EZ,2,9380
MP,GXY,2,2410
MP,GYZ,2,3600
MP,GXZ,2,2410
MP,PRXY,2,0.34
MP,PRYZ,2,0.3
MP,PRXZ,2,0.34
MP,DENS,2,1.97E-6 !KG/MM^3
!
!MASHING CONTROL
ESHAPE,3,0
ESIZE,0,6
LSEL,S,LOC,Y,96*CV/2
LESIZE,ALL,,,50,5
LSEL,ALL
!
ASEL,S,AREA,,1,3,2
AATT,1,1,1
AMESH,ALL
```

```
ASEL,ALL
!
ASEL,S,AREA,,4,10,6
AATT,1,1,1
AMESH,ALL
ASEL,ALL
!
ESIZE,0,3
ASEL,S,AREA,,2
AATT,1,1,1
AMESH,ALL
ASEL,ALL
!
ASEL,S,AREA,,5,7,1
AATT,1,1,1
AMESH,ALL
ASEL,ALL
!
!BOUNDARY CONDITIONS
NSEL,S,LOC,Y,1173,1174
D,ALL,UZ,0,0,,,UX,UY,ROTX,ROTY,ROTZ
NSEL,ALL
!
SAVE
FINISH
!
!ANALYSIS
/SOLU
/TITLE, ANALYSIS OF SINGLE CELL UNDER COMPRESSION
ANTYPE,STATIC
PSTRES,ON
!
!LOADS
NSEL,S,LOC,Y,2438.4
NSEL,A,LOC,Y,2340,2341
F,ALL,FY,-FYY/144 ! 72*2 NODES
NSEL,ALL
OUTRES,,ALL
LSWRITE,1
LSSOLVE,1
SAVE
FINISH
!
!EIGENVALUE BUCKLING
!
/SOLU
```

```
ANTYPE,BUCKLE
BUCOPT,LANB,2
MXPAND,2
LSWRITE,1
LSSOLVE,1
SAVE
FINISH
```

C.3 INPUT FILE FOR PHASE III SPECIMEN

```
/PREP7
!*****************************************
!*5-M JOINTED TOWER UNDER LATERAL LOADING
!*Vf 55%
!*Fiber 1100TEX/EPOXY (WEST SYSTEM)
!*5 LAYERS FOR THE CELL(86,-86,0,86,-86)
!*****************************************
FZZ=25000 !N (25.0KN)
CV=25.4 !CONVERSION VALUE
T=0.1875*CV/6 !1 LAYER OF UNI = 2 LAYERS OF FILA
/PBC,F,,1
/PBC,U,,1
/NERR,5,50000000
/PNUM,KP,1
/PNUM,LINE,1
/PNUM,AREA,1
/VIEW,1,3500,6000,5000
!
!GEOMETRY
K,1,0,0,0
K,2,4.19*CV,0,1.7356*CV
K,3,4.19*CV,2*96*CV,1.7356*CV
K,4,4.19*CV,0,-1.7356*CV
K,5,4.19*CV,2*96*CV,-1.7356*CV
K,6,10.69*CV,0,4.4279*CV
K,7,8.69*CV,2*96*CV,3.5995*CV
K,8,10.69*CV,0,-4.4279*CV
K,9,8.69*CV,2*96*CV,-3.5995*CV
K,10,0,96*CV,-5*CV
K,11,0,96*CV,5*CV
K,12,12*CV,96*CV,-5*CV
K,13,12*CV,96*CV,5*CV
K,14,0,13*CV,-5*CV
K,15,0,13*CV,5*CV
K,16,12*CV,13*CV,-5*CV
K,17,12*CV,13*CV,5*CV
K,18,0,105.6*CV,-5*CV
K,19,0,105.6*CV,5*CV
K,20,12*CV,105.6*CV,-5*CV
K,21,12*CV,105.6*CV,5*CV
K,22,0,180*CV,-5*CV
K,23,0,180*CV,5*CV
K,24,12*CV,180*CV,-5*CV
```

```
K,25,12*CV,180*CV,5*CV
A,2,3,5,4
A,8,9,7,6
A,6,7,3,2
A,10,11,13,12
A,14,15,17,16
A,18,19,21,20
A,22,23,25,24
ASBA,ALL,4,,DELETE,DELETE
ASBA,ALL,5,,DELETE,DELETE
ASBA,ALL,6,,DELETE,DELETE
ASBA,ALL,7,,DELETE,DELETE
A,19,18,20,21
!
!ELEMENT TYPE
ET,1,SHELL99,,0,0,0,1,3
KEYOPT,1,8,1
KEYOPT,1,11,1
!(NODE LOCATES AT THE TOP SURFACE)
!
ET,2,SHELL99,,0,0,0,1,3
KEYOPT,2,8,1
KEYOPT,2,11,0
!(NODE LOCATES AT THE MIDDLE SURFACE)
!
!REAL CONSTANT
R,1,5,0 !THE REST OF SPECIMEN
RMORE,
RMORE,1,4,T,1,-4,T
RMORE,2,90,2*T,1,4,T
RMORE,1,-4,T
R,2,10,0 !INTERFACE B/W EACH CELL
RMORE,
RMORE,1,4,T,1,-4,T
RMORE,2,90,2*T,1,4,T
RMORE,1,-4,T,1,4,T
RMORE,1,-4,T,2,90,2*T
RMORE,1,4,T,1,-4,T
!
R,3,20,0 !JOINT
RMORE,
RMORE,1,4,T,1,-4,T
RMORE,2,90,2*T,1,4,T
RMORE,1,-4,T,1,4,T
RMORE,1,-4,T,2,90,2*T
RMORE,1,4,T,1,-4,T
```

```
RMORE,1,4,T,1,-4,T
RMORE,2,90,2*T,1,4,T
RMORE,1,-4,T,1,4,T
RMORE,1,-4,T,2,90,2*T
RMORE,1,4,T,1,-4,T
!
!MATERIAL PROPERTIES
!FILAMENT WINDING
MP,EX,1,23060 !N/MM^2 (MPA)
MP,EY,1,5420
MP,EZ,1,5420
MP,GXY,1,2090
MP,GYZ,1,2080
MP,GXZ,1,2090
MP,PRXY,1,0.31
MP,PRYZ,1,0.3
MP,PRXZ,1,0.31
MP,DENS,1,1.97E-6 !KG/MM^3
!
!UNIDIRECTIONAL SHEET
MP,EX,2,28490 !N/MM^2 (MPA)
MP,EY,2,9380
MP,EZ,2,9380
MP,GXY,2,2410
MP,GYZ,2,3600
MP,GXZ,2,2410
MP,PRXY,2,0.34
MP,PRYZ,2,0.3
MP,PRXZ,2,0.34
MP,DENS,2,1.97E-6 !KG/MM^3
!
!FAILURE CRITERIA
!CHECK MAX STRESS AND TSAI-WU FAILURE CRITERIA
TB,FAIL,1,1
TBTEMP,,CRIT
TBDATA,1,0,1,1
TBTEMP,0
TBDATA,10,632.62,-258.7,1000,-1000,1000,-1000
!(IGNORE STRESS IN Z DIRECTION)
TBDATA,16,1000,1000,1000,-1,-1,-1
!
TB,FAIL,2,1
TBTEMP,,CRIT
TBDATA,1,0,1,1
TBTEMP,0
TBDATA,10,579.13,-361.55,18.08,-65.95,1000,-1000
```

```
!(IGNORE STRESS IN Z DIRECTION)
TBDATA,16,47.03,47.03,47.03,-1,-1,-1
!
!MASHING CONTROL
ESHAPE,3,0
LSEL,S,LOC,Y,13*CV/2
LESIZE,ALL,,,4,1
LSEL,ALL
!
LSEL,S,LINE,,14
LSEL,A,LINE,,38,40,1
LESIZE,ALL,,,20,1.5
LSEL,ALL
!
LSEL,S,LOC,Y,101*CV
LESIZE,ALL,,,3,1
LSEL,ALL
!
LSEL,S,LOC,Y,143*CV
LESIZE,ALL,,,15,1
LSEL,ALL
!
LSEL,S,LOC,Y,186*CV
LESIZE,ALL,,,3,1
LSEL,ALL
!
ESIZE,0,2
ASEL,S,AREA,,6,12,6
AATT,1,1,1
AMESH,ALL
ASEL,ALL
!
ASEL,S,AREA,,13
AATT,1,2,2
AMESH,ALL
ASEL,ALL
!
ASEL,S,AREA,,1,4,3
AATT,1,1,1
AMESH,ALL
ASEL,ALL
!
ESIZE,0,3
ASEL,S,AREA,,10,19,9
AATT,1,2,2
AMESH,ALL
```

```
ASEL,ALL
!
ASEL,S,AREA,,17
AATT,1,3,2
AMESH,ALL
ASEL,ALL
!
ASEL,S,AREA,,3,15,12
AATT,1,2,2
AMESH,ALL
ASEL,ALL
!
ASEL,S,AREA,,8,18,10
AATT,1,1,1
AMESH,ALL
ASEL,ALL
!
ASEL,S,AREA,,16
AATT,1,2,2
AMESH,ALL
ASEL,ALL
!
ASEL,S,AREA,,2,14,12
AATT,1,1,1
AMESH,ALL
ASEL,ALL
!
ASEL,S,AREA,,5    ! STIFFENER WHERE THE LOAD APPLIED
AATT,1,2,2
AMESH,5
ASEL,ALL
!
CSYS,5
AGEN,8,ALL,,,,45,,,0,
NUMMRG,NODE,0.01
EPLOT
CSYS,0
!
!BOUNDARY CONDITIONS
NSEL,S,LOC,Y,13*CV
D,ALL,UZ,0,0,,,UX,UY,ROTX,ROTY,ROTZ
NSEL,ALL
FINISH
SAVE
!
!ANALYSIS
```

```
/SOLU
/TITLE, ANALYSIS OF 5-M CELLULAR COMPOSITE TOWER
ANTYPE,STATIC
NLGEOM,ON
AUTOTS,ON
SSTIF,ON
NSUBST,10,500,10,ON
NROPT,AUTO
NEQIT,20
CNVTOL,F,,0.001,,1
CNVTOL,M,,0.001,,1
CNVTOL,U,,0.04,,0
TIME,8000
!
!LOADS
NSEL,S,LOC,Y,180*CV
F,ALL,FZ,FZZ/224 ! 224 NODES
NSEL,ALL
OUTRES,,ALL
LSWRITE,1
LSSOLVE,1
SAVE
FINISH
```

C.4 INPUT FILE FOR A 50-M 750 kW TUBULAR STEEL TOWER

```
/PREP7
!*********************************************
!*50 M TUBULAR STEEL TOWER
!*3.5 M IN DIA AT THE BASE AND 2.5 M IN DIA AT THE TOP
!*EXTREME CONTIDTION LOAD COMBINATION
!*********************************************
!
!FACTORED LOADS
FYY=-349580        ! N
FZZ=771620
MXX=1289310000  ! N.MM
MYY=1202160000
MZZ=572790000
RAD=1750 ! MM
PW=1.01/(2*RAD)   ! N/MM^2
/PBC,F,,1
/PBC,U,,1
/NERR,5,50000000
/PNUM,KP,1
/PNUM,LINE,1
/PNUM,AREA,1
/VIEW,1,3500,6000,5000
!
!GEOMETRY
K,1,0,0,0
K,2,0,50000,0
K,3,1750,0,0
K,4,1250,50000,0
L,3,4
AROTAT,1,,,,,,1,2,360,8
!
!ELEMENT TYPE
ET,1,93
!
!REAL CONSTANT
R,1,23,23,23,23      ! SHELL THICKNESS
!
!MATERIAL PROPERTIES
MP,EX,1,200000     ! N/MM^2 (MPA)
MP,PRXY,1,0.3
MP,DENS,1,7.85E-6         ! KG/MM^3
!
!MASHING CONTROL
```

```
ESHAPE,3,0
ESIZE,,3
LSEL,S,LOC,Y,25000
LESIZE,ALL,,,40,4
LSEL,ALL
ASEL,ALL
AATT,1,1,1
AMESH,ALL
ASEL,ALL
!
!BOUNDARY CONDITIONS
NSEL,S,LOC,Y,0
D,ALL,UZ,0,0,,,UX,UY,ROTX,ROTY,ROTZ
NSEL,ALL
!
SAVE
FINISH
!
!ANALYSIS
/SOLU
/TITLE, DESIGN OF A 50 M TUBULAR STEEL WIND TURBINE TOWER
ANTYPE,STATIC
NLGEOM,ON
AUTOTS,ON
SSTIF,ON
NSUBST,10,500,10,ON
NROPT,AUTO
NEQIT,20
CNVTOL,F,,0.001,,1
CNVTOL,M,,0.001,,1
CNVTOL,U,,0.04,,0
TIME,8000
!
!LOADS
FYAV=FYY/48        ! 48 NODES
FZAV=FZZ/48
NSEL,S,LOC,Y,50000
F,ALL,FY,FYAV
F,ALL,FZ,FZAV
NSEL,ALL
!
!MX IN TERM OF COUPLE MOMENT
FMX1=MXX/2/2500
FMX2=MXX/4/1768
!
!MY IN TERM OF COUPLE MOMENT
```

```
FMY1=MYY/4/2500
FMY1=MYY/8/1768
!
!MZ IN TERM OF COUPLE MOMENT
FMZ1=MZZ/2/2500
FMZ2=MZZ/4/1768
!
NSEL,S,NODE,,1918
F,ALL,FX,FMY1
F,ALL,FY,-FMX1+FYAV
NSEL,ALL
NSEL,S,NODE,,454
F,ALL,FX,-FMY1
F,ALL,FY,FMX1+FYAV
NSEL,ALL
NSEL,S,NODE,,1186
F,ALL,FY,-FMZ1+FYAV
F,ALL,FZ,FMY1+FZAV
NSEL,ALL
NSEL,S,NODE,,88
F,ALL,FY,FMZ1+FYAV
F,ALL,FZ,-FMY1+FZAV
NSEL,ALL
NSEL,S,NODE,,1552
F,ALL,FX,FMY2
F,ALL,FY,-FMX2-FMZ2+FYAV
F,ALL,FZ,FMY2+FZAV
NSEL,ALL
NSEL,S,NODE,,2284
F,ALL,FX,FMY2
F,ALL,FY,-FMX2+FMZ2+FYAV
F,ALL,FZ,-FMY2+FZAV
NSEL,ALL
NSEL,S,NODE,,8
F,ALL,FX,-FMY2
F,ALL,FY,FMX2+FMZ2+FYAV
F,ALL,FZ,-FMY2+FZAV
NSEL,ALL
NSEL,S,NODE,,820
F,ALL,FX,-FMY2
F,ALL,FY,FMX2-FMZ2+FYAV
F,ALL,FZ,FMY2+FZAV
NSEL,ALL
!
ASEL,S,LOC,Z,-RAD,0
SFA,ALL,,PRES,PW! WIND PRESSURE APPLIED ON AREA WHERE Z<=0
```

```
ASEL,ALL
OUTRES,,ALL
LSWRITE,1
LSSOLVE,1
SAVE
FINISH
```

C.5 INPUT FILE FOR A 50-M 750 kW CFRP TOWER

```
/PREP7
!*****************************************
!*DESIGN OF CFRP TOWER
!*DIA. AT THE BASE 3.5M,
!*DIA. AT THE TOP 2.5M,
!*ID 2.0M,AND H 50M
!*Vf 63%
!*****************************************
t=1.25
!
!FACTORED LOADS
FYY=-349580        ! N
FZZ=771620
MXX=1289310000  ! N.MM
MYY=1202160000
MZZ=572790000
RAD=1750 ! MM
PW=1.01/(2*RAD)   ! N/MM^2
/PBC,F,,1
/PBC,U,,1
/NERR,5,50000000
/PNUM,KP,1
/PNUM,LINE,1
/PNUM,AREA,1
/VIEW,1,3500,6000,5000
!
!GEOMETRY
K,1,0,0,0
K,2,0,50000,0
K,3,1000,0,0
K,4,1000,50000,0
K,5,1750,0,0
K,6,1250,50000,0
L,3,4
L,5,6
AROTAT,1,,,,,,1,2,360,8
AROTAT,2,,,,,,1,2,360,8
A,3,4,6,5
A,7,8,22,21
A,9,10,24,23
A,11,12,26,25
A,13,14,28,27
A,15,16,30,29
```

```
A,17,18,32,31
A,19,20,34,33
!
!ELEMENT TYPE
ET,1,SHELL99,,0,0,0,1,3
!
!REAL CONSTANT
R,1,20,0 !INNER SHELL
RMORE,
RMORE,2,0,t,1,90,t
RMORE,1,90,t,1,90,t
RMORE,1,90,t,1,90,t
RMORE,1,90,t,1,90,t
RMORE,1,90,t,2,0,t
RMORE,2,0,t,1,90,t
RMORE,1,90,t,1,90,t
RMORE,1,90,t,1,90,t
RMORE,1,90,t,1,90,t
RMORE,1,90,t,2,0,t
!
R,2,21,0 !OUTER SHELL
RMORE,
RMORE,2,0,t,1,90,t
RMORE,1,90,t,1,90,t
RMORE,1,90,t,1,90,t
RMORE,1,90,t,1,90,t
RMORE,1,90,t,2,0,t
RMORE,2,0,t,1,90,t
RMORE,1,90,t,1,90,t
RMORE,1,90,t,1,90,t
RMORE,1,90,t,1,90,t
RMORE,1,90,t,2,0,t
RMORE,2,0,t
!
R,3,40,0 !STIFFENER
RMORE,
RMORE,2,0,t,1,90,t
RMORE,1,90,t,1,90,t
RMORE,1,90,t,1,90,t
RMORE,1,90,t,1,90,t
RMORE,1,90,t,2,0,t
RMORE,2,0,t,1,90,t
RMORE,1,90,t,1,90,t
RMORE,1,90,t,1,90,t
RMORE,1,90,t,1,90,t
RMORE,1,90,t,2,0,t
```

```
RMORE,2,0,t,1,90,t
RMORE,1,90,t,1,90,t
RMORE,1,90,t,1,90,t
RMORE,1,90,t,1,90,t
RMORE,1,90,t,2,0,t
RMORE,2,0,t,1,90,t
RMORE,1,90,t,1,90,t
RMORE,1,90,t,1,90,t
RMORE,1,90,t,1,90,t
RMORE,1,90,t,2,0,t
!
!MATERIAL PROPERTIES
MP,EX,1,142000 !N/MM^2 (MPA)
MP,EY,1,10300
MP,EZ,1,10300
MP,GXY,1,7200
MP,GYZ,1,7200
MP,GXZ,1,7200
MP,PRXY,1,0.27
MP,PRYZ,1,0.3
MP,PRXZ,1,0.27
MP,DENS,1,1.58E-6 !KG/MM^3
!
MP,EX,2,142000 !N/MM^2 (MPA)
MP,EY,2,10300
MP,EZ,2,10300
MP,GXY,2,7200
MP,GYZ,2,7200
MP,GXZ,2,7200
MP,PRXY,2,0.27
MP,PRYZ,2,0.3
MP,PRXZ,2,0.27
MP,DENS,2,1.58E-6 !KG/MM^3
!
!FAILURE CRITERIA
!CHECK MAX STRESS AND TSAI-WU FAILURE CRITERIA
TB,FAIL,1,1
TBTEMP,,CRIT
TBDATA,1,0,1,1
TBTEMP,0
TBDATA,10,2280,-1440,57,-228,1000,-1000
!(IGNORE STRESS IN Z DIRECTION)
TBDATA,16,71,71,71,-1,-1,-1
!
TB,FAIL,2,1
TBTEMP,,CRIT
```

```
TBDATA,1,0,1,1
TBTEMP,0
TBDATA,10,2280,-1440,1000,-1000,1000,-1000
!(IGNORE STRESS IN Z DIRECTION)
TBDATA,16,1000,1000,1000,-1,-1,-1
!
!MASHING CONTROL
ESHAPE,2,0
LSEL,S,LOC,Y,25000
LESIZE,ALL,,,40,3
LSEL,ALL
!
ESIZE,0,3
ASEL,S,AREA,,1,8,1 !INNER
AATT,1,1,1
AMESH,ALL
ASEL,ALL
!
ASEL,S,AREA,,9,16,1 !OUTER
AATT,1,2,1
AMESH,ALL
ASEL,ALL
!
ESIZE,0,2
ASEL,S,AREA,,17,24,1 !STIFFENER
AATT,1,3,1
AMESH,ALL
ASEL,ALL
!
!BOUNDARY CONDITIONS
NSEL,S,LOC,Y,0
D,ALL,UZ,0,0,,,UX,UY,ROTX,ROTY,ROTZ
NSEL,ALL
!
SAVE
FINISH
!
!ANALYSIS
/SOLU
/TITLE, DESIGN OF 8-CELL 50 M CFRP WIND TURBINE TOWER
ANTYPE,STATIC
NLGEOM,ON
AUTOTS,ON
SSTIF,ON
NSUBST,10,500,10,ON
NROPT,AUTO
```

```
NEQIT,20
CNVTOL,F,,0.001,,1
CNVTOL,M,,0.001,,1
CNVTOL,U,,0.04,,0
TIME,8000
!
!LOADS
FYAV=FYY/120      ! 120 NODES
FZAV=FZZ/120
NSEL,S,LOC,Y,50000
F,ALL,FY,FYAV
F,ALL,FZ,FZAV
NSEL,ALL
!
!MX IN TERM OF COUPLE MOMENT
FMX1=MXX/2/2500
FMX2=MXX/4/1768
!
!MY IN TERM OF COUPLE MOMENT
FMY1=MYY/4/2500
FMY1=MYY/8/1768
!
!MZ IN TERM OF COUPLE MOMENT
FMZ1=MZZ/2/2500
FMZ2=MZZ/4/1768
!
NSEL,S,NODE,,4846
F,ALL,FX,FMY1
F,ALL,FY,-FMX1+FYAV
NSEL,ALL
NSEL,S,NODE,,3382
F,ALL,FX,-FMY1
F,ALL,FY,FMX1+FYAV
NSEL,ALL
NSEL,S,NODE,,4114
F,ALL,FY,-FMZ1+FYAV
F,ALL,FZ,FMY1+FZAV
NSEL,ALL
NSEL,S,NODE,,3016
F,ALL,FY,FMZ1+FYAV
F,ALL,FZ,-FMY1+FZAV
NSEL,ALL
NSEL,S,NODE,,4480
F,ALL,FX,FMY2
F,ALL,FY,-FMX2-FMZ2+FYAV
F,ALL,FZ,FMY2+FZAV
```

```
NSEL,ALL
NSEL,S,NODE,,5212
F,ALL,FX,FMY2
F,ALL,FY,-FMX2+FMZ2+FYAV
F,ALL,FZ,-FMY2+FZAV
NSEL,ALL
NSEL,S,NODE,,2936
F,ALL,FX,-FMY2
F,ALL,FY,FMX2+FMZ2+FYAV
F,ALL,FZ,-FMY2+FZAV
NSEL,ALL
NSEL,S,NODE,,3748
F,ALL,FX,-FMY2
F,ALL,FY,FMX2-FMZ2+FYAV
F,ALL,FZ,FMY2+FZAV
NSEL,ALL
!
ASEL,S,AREA,,9,12,1
SFA,ALL,,PRES,PW
ASEL,ALL
OUTRES,,ALL
LSWRITE,1
LSSOLVE,1
SAVE
FINISH
```

APPENDIX D: LOCAL BUCKLING

The elastic stability theory of the plate was used to determine the buckling strength of the Phase I specimens, since local buckling was the dominant failure mode in the tested specimens. The Phase I specimen properties, which include the bending moment diagram and the moment of inertia along the specimen are shown in **Figure D-1**.

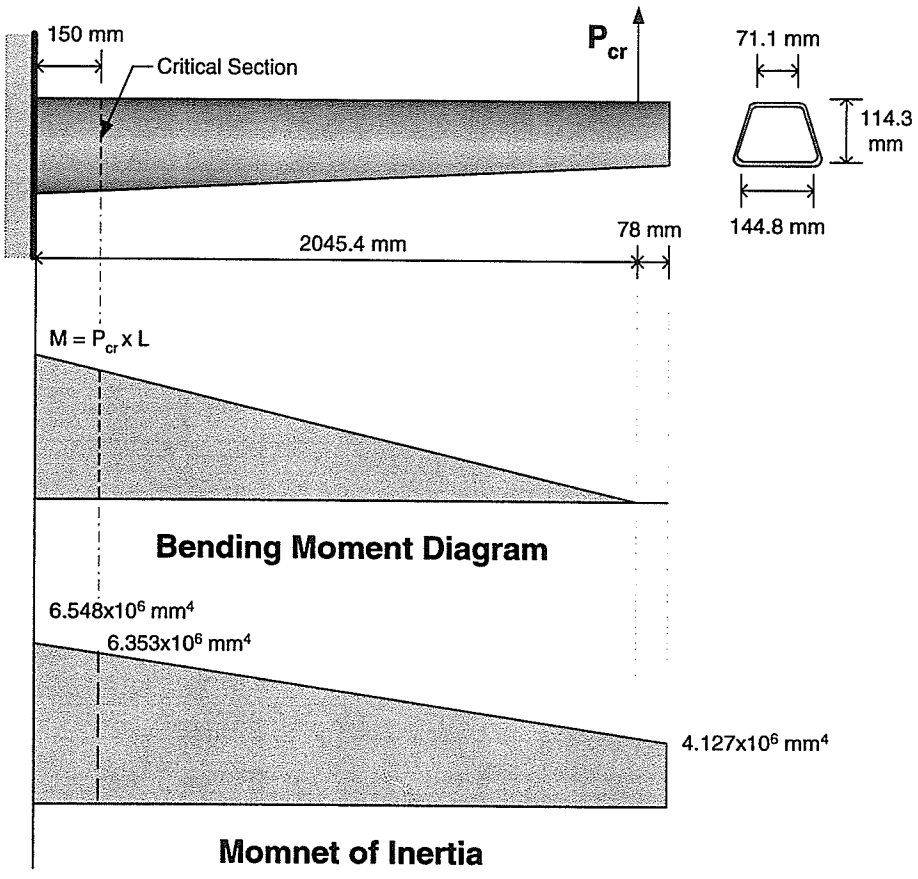

Figure D-1 Phase I specimen properties

The critical stress for rectangular plates with various types of edge support, and with loads in the plane of the plate of distributed along the edges, is given by

$$\sigma_{cr} = k\frac{\pi^2 E}{12(1-\nu^2)(b/t)^2} \qquad \textbf{Equation D.1}$$

with:

k = 4 (assuming both edges are simply supported);

E = 28.49 GPa (from material tests);

ν = 0.34 (from material tests);

b = 71.12 mm; and

t = 2 mm (thickness of longitudinal fiber only).

Therefore, the buckling stress of the plate at the critical cross section was determined to be 83.81 MPa using ***Equation D.1***.

Using the stress analysis, the maximum compressive stress on the critical cross section can be determined by

$$\sigma = \frac{My}{I} \qquad \textbf{Equation D.2}$$

where

M = bending moment, in this case, was equal to $P_{cr} \times L$;

y = distance from the neutral axis, which was equal to 78.38 mm; and

I = moment of inertia, which was calculated to be 6.353×10^6 mm^4.

Therefore, the ultimate load, P_{cr}, was determined to be equal to 3.58 kN, which is in good agreement with the average ultimate load of 3.72 kN obtained from experimental program.